

Effect of late-time transition of SNIa Absolute Magnitude on the best fit values of cosmological and cosmographic parameters

Leiden Institute of Physics



Universiteit Leiden

Chrisostomos-Panagiotis Stamou

Student ID: s2917432

LION Supervisor: Dr. S. Patil

External Supervisor: Dr. L. Perivolaropoulos

Leiden, The Netherlands

June 30, 2025

Contents

1 Cosmology Overview, Hubble Crisis and Late-Time Transition	5
1.1 The Cosmological Principle	5
1.2 Friedmann Equations	6
1.3 The Λ CDM Model	12
1.4 The Hubble Tension and Late-Time Transition	14
1.5 Outline of the Thesis	16
2 Distance Ladder and Type Ia Supernovae	17
2.1 Luminosity Distance	17
2.2 Astronomical Magnitudes and the Distance Modulus	20
2.3 Distance Ladder	22
2.3.1 Cepheid Variable Start	22
2.3.2 Type Ia Supernovae	24
2.4 Flat Λ CDM	29
2.5 Cosmographic Expansion	29
2.6 Flat w_0 CDM Model	34
2.7 Flat Chevallier-Polarski-Linder Model	35
3 Frequentist & Bayesian Inference for a flat ΛCDM Model	36
3.1 Frequentist and χ^2 Statistics	36
3.2 Bayesian Inference	37
3.2.1 Monte Carlo Markon Chain via <i>emcee</i>	38
3.2.2 Nested Sampling	39
3.3 Λ CDM Inference via χ^2 Minimization	40
3.3.1 No-transition in Absolute Magnitude	41
3.3.2 Transition in Absolute Magnitude	44
3.3.3 AIC & BIC Tests	46
3.3.4 Accounting for the Volumetric Redshift Scatter Bias	49
3.4 Λ CDM Inference via MCMC & Nested Sampling	51
3.4.1 No-transition in M — MCMC	51
3.4.2 Transition in M — MCMC	53
3.4.3 No-Transition in M — Nested Sampling/dynesty	60
3.4.4 Transition in M — Nested Sampling/dynesty	62
3.5 Frequentist vs Bayesian for the flat Λ CDM	65
4 Expanding the analysis	69
4.1 Cosmographic Expansion Model up to $\mathcal{O}(z^2)$ order	69
4.1.1 χ^2 minimization	69
4.1.2 MCMC Sampling	71
4.1.3 Nested Sampling	75
4.2 w_0 CDM Model	79
4.2.1 χ^2 minimization	79
4.2.2 MCMC Sampling	81
4.2.3 Nested Sampling	87

4.3	CPL Model	90
4.3.1	<i>MCMC</i> Sampling	90
4.3.2	Nested Sampling	95
5	Summary and Discussion	99
	References	102

Abstract

This thesis investigates the impact of a late-time transition in the standardized absolute magnitude M of Type Ia supernovae (SnIa), provided by the PANTHEON+ survey [1], on the inference of cosmological parameters. Motivated by the work of Perivolaropoulos & Skara (P&S) [2], who demonstrated that introducing a transition in M improves the fit to the Pantheon+ dataset in the context of a flat Λ CDM model, we aim to reproduce and extend their analysis across a broader set of cosmological models. We first validate the P&S results using a standard χ^2 minimization and then generalize the analysis using Bayesian parameter estimation techniques, specifically a *Monte Carlo Markov Chain (MCMC)* sampling via `emcee` and Nested Sampling, with the latter providing also the evidence of the model under consideration, making the comparison between models via the Bayes factor possible. The models tested include Λ CDM, a cosmographic expansion truncated at the deceleration parameter q_0 , *i.e.* *up to second order redshift*, the w_0 CDM model, and the CPL (Chevallier–Polarski–Linder) parameterization for dark energy. For each model- besides the CPL model, the complexity of which made a robust χ^2 inference not feasible- we perform model comparison using the Akaike Information Criterion (AIC), the Bayesian Information Criterion (BIC), and Bayesian evidence ratios. Our preliminary results indicate that the inclusion of a transition in M , occurring at a characteristic distance of approximately 20 Mpc, is consistently supported across all models with the Hubble constant H_0 , being the only parameter consistently affected. This finding suggests a possible late-time inhomogeneity in SnIa luminosity that may have significant implications for cosmological inference and the interpretation of the Hubble tension, while also hinting towards possible hidden physics in the low-redshift regime. The numerical codes are all available on <https://github.com/ChrisStamou/Thesis-2025>

1 Cosmology Overview, Hubble Crisis and Late-Time Transition

1.1 The Cosmological Principle

In a nutshell, cosmology is the branch of physics that studies the structure and evolution of the Universe on large scales, exceeding the 100 Mpc. On such scales, due to the presence of supermassive systems such as galaxies, clusters of galaxies, etc., gravity is the dominant field and the theory to describe the interactions among these supermassive systems is the General Theory of Relativity (GR), formulated in 1915 by Albert Einstein [3]. Einstein realized that gravity should no longer be regarded as a force in the conventional sense but rather as a manifestation of the curvature of the spacetime, this curvature being induced by the presence of matter [4], a realization that he beautifully and elegantly described mathematically in his GR field equations:

$$R_{\mu\nu} - \frac{1}{2}g_{\mu\nu}R = \frac{8\pi G}{c^4}T_{\mu\nu}, \quad (1.1)$$

where the geometry of the spacetime is described via the metric tensor $g_{\mu\nu}$, the Ricci tensor, $R_{\mu\nu}$ and the Ricci scalar R describe the curvature of the spacetime which is induced by the presence of matter, described via the energy-momentum tensor $T_{\mu\nu}$. The most famous summary of Einstein's field equations is:
Space tells matter how to move and matter tells space how to curve.

Once GR was formulated, a Pandora box opened as scientists finally had the tool to go further than what they already knew and explore how our Universe behaves on large scales. This was the point in history, where Cosmology shifted from a philosophical endeavor to a quantitative and predictive scientific discipline. Cosmology's goal is to describe the Universe on large scales. If we start by looking up at the sky, we will see our galaxy, *i.e.* the Milky Way, which is stars grouped in a local density concentration. Looking a bit further away, we will see our neighbor, Andromeda (M31), which together with the Triangulum galaxy (M33) and around 50 smaller dwarf galaxies constitute the so-called *Local Group*. Going on even larger scales, we will see that our Local Group sits on the outskirts of a cluster of galaxies centered in the constellation of Virgo. We can therefore understand that on small scales matter is distributed in a highly irregular way but, as we look on larger and larger scales, the matter distribution looks more and more uniform. Evidence from the temperature measurement of the Cosmic Microwave Background Radiation (CMB) [5], showing constancy on different directions in the sky, implies that our Universe appears to be isotropic, meaning that there is no preferred direction, or to put it in a more scientific way, no matter which direction an observer points, the large-scale properties such as the temperature of CMB or the density of galaxies, appear statistically the same. Following the Copernical principle, implying that we are not at a special location, *i.e.* the Universe has no preferred center, then isotropy also implies homogeneity, meaning that the Universe looks the same in all locations.

Besides the Copernican principle, the homogeneity of the Universe is observationally well supported from galaxy surveys [6], [7], Lyman α forest and quasar absorption lines [8], [9], the Integrated Sachs-Wolf effect [10] and Weak Lensing surveys [11].

Cosmological Principle: *On scales larger than 100 Mpc, the Universe is homogeneous and isotropic.*

The isotropy and homogeneity of the Universe imply symmetries that strongly constrains the possible forms of the spacetime geometry. These symmetries uniquely lead to the Friedman-Robertson-Walker (FRW) metric [12, 13, 14, 15, 4, 16], *i.e.* the metric of our Universe:

$$ds^2 = -c^2 dt^2 + a^2(t) \left[\frac{dr^2}{1 - kr^2} + r^2 d\theta^2 + r^2 \sin^2 \theta d\phi^2 \right] \quad (1.2)$$

This metric is written in spherical coordinates, where $a(t)$ is the scale factor and k the curvature of the Universe, which is set to be equal to -1 , 1 or zero. We're also using the $(-, +, +, +)$ signature convention. The FRW metric, or equivalently, line element, is the basis on which the mathematical foundation of Cosmology is built on, starting from solving the Einstein equations for (1.1).

1.2 Friedmann Equations

To understand the dynamical evolution of our Universe, one needs to solve the Einstein equations for the FRW metric. The left-hand-side of the Einstein equations describe the geometry and the right-hand-side the matter content. Therefore, we need to specify and express both. Starting from the left-hand-side, the geometry is an FRW one, which can be also written in tensor form as:

$$ds^2 = g_{\mu\nu} dx^\mu dx^\nu \quad (1.3)$$

from which it becomes clear that:

$$g_{\mu\nu} = \begin{pmatrix} -1 & 0 & 0 & 0 \\ 0 & \frac{a^2(t)}{1 - kr^2} & 0 & 0 \\ 0 & 0 & a^2(t) r^2 & 0 \\ 0 & 0 & 0 & a^2(t) r^2 \sin^2 \theta \end{pmatrix} \quad (1.4)$$

What is now left is a sometimes tedious, but always beautiful algebraic calculation of the Ricci tensor and the Ricci scalar, for which one needs first to

calculate the Christoffel symbols for (1.4). The non-zero Christoffel symbols are:

$$\Gamma_{01}^1 = \Gamma_{10}^1 = \frac{\dot{a}(t)}{a(t)}, \Gamma_{02}^2 = \Gamma_{20}^2 = \frac{\dot{a}(t)}{a(t)}, \Gamma_{03}^3 = \Gamma_{30}^3 = \frac{\dot{a}(t)}{a(t)},$$

$$\Gamma_{11}^1 = \frac{kr}{1-kr^2}, \Gamma_{22}^1 = -r(1-kr^2), \Gamma_{33}^1 = -r(1-kr^2)\sin^2\theta,$$

$$\Gamma_{12}^2 = \Gamma_{21}^2 = \frac{1}{r}, \Gamma_{13}^3 = \Gamma_{31}^3 = \frac{1}{r}, \Gamma_{33}^2 = -\sin\theta\cos\theta,$$

$$\Gamma_{23}^3 = \Gamma_{32}^3 = \cot\theta$$

The Ricci tensor is defined as:

$$R_{\mu\nu} = \partial_\lambda\Gamma_{\mu\nu}^\lambda - \partial_\nu\Gamma_{\mu\lambda}^\lambda + \Gamma_{\lambda\rho}^\lambda\Gamma_{\mu\nu}^\rho - \Gamma_{\nu\rho}^\lambda\Gamma_{\mu\lambda}^\rho \quad (1.5)$$

Plugging in the Christoffel symbols results in the following non-zero components:

$$R_{00} = -3\frac{\ddot{a}(t)}{a(t)} \quad (1.6)$$

$$R_{11} = \frac{a(t)\ddot{a}(t) + 2\dot{a}(t)^2 + 2k}{1-kr^2} \quad (1.7)$$

$$R_{22} = r^2(a(t)\ddot{a}(t) + 2\dot{a}(t)^2 + 2k) \quad (1.8)$$

$$R_{33} = r^2\sin^2\theta(a(t)\ddot{a}(t) + 2\dot{a}(t)^2 + 2k) \quad (1.9)$$

What is now left to complete the calculation of the left-hand-side of Einstein's equations is the Ricci scalar, which is just the contraction of the Ricci tensor:

$$R = g^{\mu\nu}R_{\mu\nu} = R = 6\left(\frac{\ddot{a}(t)}{a(t)} + \left(\frac{\dot{a}(t)}{a(t)}\right)^2 + \frac{k}{a^2(t)}\right) \quad (1.10)$$

The left-hand-side of the Einstein equations, is also known as the Einstein tensor, $G_{\mu\nu}$. Plugging in the Einstein tensor the metric tensor, the non-zero Ricci tensor components and the Ricci scalar yields the following non-zero components:

$$G_{00} = 3 \left(\frac{\dot{a}(t)}{a(t)} \right)^2 + 3 \frac{k}{a^2(t)} \quad (1.11)$$

$$G_{11} = - \left(2 \frac{\ddot{a}(t)}{a(t)} + \left(\frac{\dot{a}(t)}{a(t)} \right)^2 + \frac{k}{a^2(t)} \right) \cdot \frac{a^2(t)}{1 - kr^2} \quad (1.12)$$

$$G_{22} = - \left(2 \frac{\ddot{a}(t)}{a(t)} + \left(\frac{\dot{a}(t)}{a(t)} \right)^2 + \frac{k}{a^2(t)} \right) \cdot a^2(t)r^2 \quad (1.13)$$

$$G_{33} = - \left(2 \frac{\ddot{a}(t)}{a(t)} + \left(\frac{\dot{a}(t)}{a(t)} \right)^2 + \frac{k}{a^2(t)} \right) \cdot a^2(t)r^2 \sin^2 \theta \quad (1.14)$$

Let us now move on to the right-hand-side of (1.1), *i.e.* the energy-momentum tensor, $T_{\mu\nu}$. This tensor describes the matter content of the system under consideration, which in our case is the Universe! So, how can someone define an energy-momentum tensor that will describe our Universe in large scales? It was Hermann Weyl who answered this question with his famous postulate, stating that following the isotropy and homogeneity of the Universe on large scales, it contains a homogeneous *substratum* of matter, inside which galaxies are moving like the particles of a perfect fluid. Therefore, the matter content can be represented by a perfect fluid of density ρ and pressure p , moving with a 4-velocity $u^\mu = (-1, 0, 0, 0)$ in units where $c = 1$, as a rank-2 tensor:

$$T_{\mu\nu} = (\rho + p) u_\mu u_\nu + p g_{\mu\nu} \quad (1.15)$$

A physical property structured within this tensor is of course the conservation of energy and momentum, which in this case is mathematically expressed as:

$$\nabla_\mu T^{\mu\nu} = 0 \quad (1.16)$$

which implies that if taking the covariant derivative of the Einstein equations (1.1), should yield:

$$\nabla_\mu G^{\mu\nu} = 0 \quad (1.17)$$

which in words means that the conservation of space is consistent with the conservation of energy and momentum. Equation (1.17) is of fundamental importance in GR. Finding a tensor that describes the curvature of spacetime while it is also conserved was the original process with which Einstein derived $G_{\mu\nu}$ and

then his equations [4]. Nowadays, the common way of deriving Einstein equations is more easily done via the variation calculus using the Einstein-Hilbert action [17].

We are now fully ready to solve Einstein equations for the FRW metric. Setting $\mu = \nu = 0$, we can easily derive Friedman's first equation:

$$\boxed{\left(\frac{\dot{a}(t)}{a(t)}\right)^2 = \frac{8\pi G}{3}\rho(t) - \frac{k}{a^2(t)}} \quad (1.18)$$

Using the spatial components of the Einstein equations, it is straightforward to derive Friedmann's second equation:

$$\boxed{\frac{\ddot{a}(t)}{a(t)} = -\frac{4\pi G}{3}(\rho(t) + 3p(t))} \quad (1.19)$$

Friedmann's equations (1.18),(1.19) are the solution of the Einstein field equations (1.1) for an FRW metric (1.2) and they are differential equations, the solution of which describes a dynamical evolution of the scale factor. To solve these equations, one needs to specify a density and a pressure for the perfect fluid, *i.e.* define the matter content. Density and pressure are connected and we can describe them both via the equation of state parameter:

$$w = \frac{p}{\rho} \quad (1.20)$$

where $c = 1$. Using the energy-momentum conservation equation (1.16) and (1.20), one can easily derive the *continuity equation*:

$$\boxed{\dot{\rho} = -3\frac{\dot{a}}{a}\rho(1+w)} \quad (1.21)$$

from which we can straightforward prove that,

$$\rho \propto a^{-3(1+w)} \quad (1.22)$$

To find an expression for the density ρ , we first need to find a value for w , which describes the matter content of the Universe, that can be:

- **baryonic + dark matter \equiv matter**, non-relativistic particle with $w = 0$, *i.e.* pressureless matter
- **radiation (photons & neutrinos)**, relativistic particles with $w = \frac{1}{3}$

A derivation of the w value for both cases is a standard exercise in Cosmology, using basic principles from statistical physics and is nicely formulated in [18]. Plugging in the matter and radiation cases into (1.22) yields:

$$\rho(a) = \begin{cases} \rho_{m,0} a^{-3} & \text{for matter } (w=0) \\ \rho_{r,0} a^{-4} & \text{for radiation } (w=\frac{1}{3}) \end{cases} \quad (1.23)$$

where $\rho_{m,0}$ and $\rho_{r,0}$ are the present day matter and radiation densities.

We are now equipped with all the tools to solve Friedmann's equations. The simplest case possible would be to consider an only-matter dominated Universe and an only-radiation dominated Universe. Substituting (1.23) into (1.18) yields:

$$a(t) = \begin{cases} \left(\frac{3}{2} \sqrt{\frac{8\pi G}{3}} \rho_{m,0} t \right)^{2/3} & \text{for matter domination } (w=0) \\ \left(2 \sqrt{\frac{8\pi G}{3}} \rho_{r,0} t \right)^{1/2} & \text{for radiation domination } (w=\frac{1}{3}) \end{cases} \quad (1.24)$$

One message is loud and clear from these solutions, and that is that solving the Einstein equations for an FRW metric reveals an expanding Universe, a concept entirely opposite to what Einstein and the scientific community used to believe in that time. It was a common belief that the Universe is static, meaning that it was here since forever and will be here forever. Therefore, according to that belief, Einstein equations were wrong and needed to be modified. Einstein then realized in 1917 that for his equations to describe a static Universe, he needs to insert a constant term into his equations that would force the expansion to stop. He denoted this constant by Λ and named it, *the Cosmological Constant* [19]. He therefore modified his equation as:

$$R_{\mu\nu} - \frac{1}{2}g_{\mu\nu}R + \Lambda g_{\mu\nu} = \frac{8\pi G}{c^4}T_{\mu\nu} \quad (1.25)$$

This is mathematically and physically allowed, since the addition of a constant term does not violate the conservation condition of the Einstein tensor. The addition of the cosmological constant term, leads to the following modified Friedmann equation:

$$\left(\frac{\dot{a}(t)}{a(t)} \right)^2 = \frac{8\pi G}{3}\rho(t) - \frac{k}{a^2(t)} + \frac{\Lambda}{3} \quad (1.26)$$

$$\frac{\ddot{a}(t)}{a(t)} = -\frac{4\pi G}{3}(\rho(t) + 3p(t)) + \frac{\Lambda}{3} \quad (1.27)$$

The implication for a static Universe is that the scale factor is constant, *i.e.* $\dot{a} = \ddot{a} = 0$. Plugging this into the Friedmann equations yield:

$$\rho_\Lambda = \frac{\Lambda}{4\pi G} \quad \& \quad \frac{k}{a^2} = \Lambda \quad (1.28)$$

which was the first relativistic cosmological model. Furthermore, since the cosmological constant is a substance with constant density, *i.e.* $\dot{\rho} = 0$, we see from the continuity equation that the state parameter should be:

$$w = -1 \Rightarrow p = -\rho \quad (1.29)$$

Therefore, the cosmological constant Λ is an unknown substance with negative pressure, acting against gravity to restore the static Universe!

However, it turned out a decade later, that Einstein's original equations were correctly predicting an expanding Universe! It was Edwin Hubble in 1929 [20], who showed that the recession velocity of a galaxy is proportional to its distance from us, demonstrating this way that galaxies are receding away from us, proving thus the expansion of the Universe! This relation between the recession velocity and the distance of the galaxy is known as the *Hubble law*:

$$v = H_0 d \quad (1.30)$$

where v is the velocity, d is the distance and the coefficient H_0 was named after Hubble, as the Hubble constant. This was the discovery that made Einstein regret the introduction of his cosmological constant and quote it as “the biggest blunder of his life” [21].

To put everything in order, after Hubble's discovery, it was established that the Universe is expanding and based on the matter content available, *i.e.* matter and radiation, this expansion is decelerating (1.24). However, many years after Hubble's discovery and Einstein's retraction of the cosmological constant, two independent Supernova projects, [22, 23], measuring distances to Supernovae of Type Ia, discovered that the Universe is expanding in an accelerated rate, a result opposite to the well established belief of the decelerating expansion! The source of this accelerating expansion was dubbed as *Dark Energy* and it was found that it dominates in the Universe, occupying almost 70% of the total density. This discovery raised a plethora of questions, regarding the nature of this Dark Energy (DE). The most simple answer explaining DE was surprisingly enough, Einstein's cosmological constant! Bringing Λ back at the game and dropping the static condition of $\dot{a} = \ddot{a} = 0$, makes the Universe expanding in an accelerated rate, with this negative pressure substance pushing violently

galaxies away from each other! This is the most simple answer, but not necessarily the correct one. We still don't know what the nature of Dark Energy is and answering this question is at the heart of the active Cosmology research. Lots of models have been proposed in addition to the cosmological constant, or Λ CDM, where CDM stands for "Cold Dark Matter", such as modified matter models, where one modifies the right-hand-side of Einstein's equations to describe DE, or modified gravity models, where one considers the accelerated expansion as a pure geometrical consequence of higher order curvature terms in the Einstein-Hilbert action (see [18] for a nice discussion of both models). For now let us focus on the simple Λ CDM model.

1.3 The Λ CDM Model

Let us now define mathematically the Λ CDM model and its associated parameters. We start by defining the Hubble parameter as:

$$H(t) = \frac{\dot{a}}{a} \quad (1.31)$$

We have already defined the matter and radiation densities in (1.23). Is is more convenient to work with dimensionless quantities, so we will define the density parameter Ω as:

$$\Omega_i = \frac{\rho_i}{\rho_{crit}}, \quad \text{where} \quad \rho_{crit} = \frac{3H^2}{8\pi G} \quad (1.32)$$

Plugging this into the Friedman equation (1.18) with the inclusion of Λ of course yields:

$$H^2(t) = H_0^2 \left[\Omega_{m,0} a^{-3} + \Omega_{r,0} a^{-4} + \Omega_{\Lambda,0} - \frac{k}{a^2 H_0^2} \right] \quad (1.33)$$

where the 0 subscript denotes present day values. to express everything in terms of Ω , we can also define the curvature density parameter as:

$$\Omega_k = \frac{-k^2}{a^2 H^2} \quad (1.34)$$

Thus the Friedmann equation can be written as:

$$H^2(t) = H_0^2 [\Omega_{m,0} a^{-3} + \Omega_{r,0} a^{-4} + \Omega_{\Lambda,0} + \Omega_{k,0} a^{-2}] \quad (1.35)$$

Equation (1.35) describes a Universe containing baryonic and cold dark matter through $\Omega_{m,0}$, radiation, $\Omega_{r,0}$, cosmological constant, Ω_{Λ} and a curvature

term. Recent observations place precise constraints on the composition of the Universe. The *Planck 2018* cosmic microwave background analysis [5] reports a present-day matter density of $\Omega_m = 0.315 \pm 0.007$, and a spatial curvature consistent with flatness, $\Omega_k \approx 0$. The dark energy density is inferred to be $\Omega_\Lambda \approx 0.685$, under the assumption of a flat Λ CDM model. The radiation density today is negligible, with $\Omega_r \sim 10^{-4}$, and becomes significant only at very early times. Complementary results from the *Pantheon+* supernova compilation [1], which probes the late-time expansion history, yield $\Omega_m = 0.334 \pm 0.018$ assuming a flat Universe. This independently supports a dominant dark energy contribution of approximately $\Omega_\Lambda \approx 0.666$, consistent with the Planck results within uncertainties. In addition to CMB measurements, several independent probes support the spatial flatness of the Universe. Baryon acoustic oscillation (BAO) data from the BOSS and eBOSS surveys [24], weak gravitational lensing from the DES [25] and KiDS-1000 [26], and large-scale structure measurements all constrain the curvature parameter to be consistent with $\Omega_{k,0} \simeq 0$ within percent-level uncertainties.

We can therefore conclude based on the aforementioned constraints, that a flat Λ CDM model is favored and update Friedman equation as:

$$H^2(t) = H_0^2 [\Omega_{m,0}a^{-3} + \Omega_\Lambda] \quad (1.36)$$

where we dropped the 0 subscript in Ω_Λ , since the cosmological constant density is constant throughout the cosmic history. The total matter content density parameter, *i.e.* the summation of the density parameters, should obviously be equal to 1, which in the flat Λ CDM model translates to:

$$\Omega_\Lambda = 1 - \Omega_{m,0} \quad (1.37)$$

To infer the values of the associated parameters of the Λ CDM model, one needs to express equation (1.36) in terms of observables. The most basic observable in Cosmology that encodes the meaning of time and distance in one, is the *redshift*, which is defines as:

$$z = \frac{\lambda_{\text{observed}} - \lambda_{\text{emitted}}}{\lambda_{\text{emitted}}} \quad (1.38)$$

where λ is the radiation's wavelength. Since galaxies are moving away from us, the light that they emit is being stretched during its journey to us and as a result the observed wavelength shift towards the red regime of the electromagnetic spectrum. Measuring the redshift of an astronomical object far away from us, is the cornerstone of observational cosmology which allows us to infer parameters and test models. The redshift is connected to the scale factor of the Universe,

via:

$$1 + z = \frac{a_0}{a} = \frac{1}{a} \quad (1.39)$$

where we normalized the present-day value of the scale factor to be equal to 1. Using this definition, Friedmann's equation for the Λ CDM model (1.36) can be written as,

$$H^2(z) = H_0^2 \left[\Omega_{m,0} (1+z)^3 + \Omega_\Lambda \right] \quad (1.40)$$

Therefore, the parameters one needs to infer to describe the flat Λ CDM universe are two, namely the Hubble constant, H_0 and $\Omega_{m,0}$.

We mentioned that independent probes provide good constraints on the flat Λ CDM model, but we cannot deterministically state that we live in a Λ CDM Universe. Why? What are the challenges? We discuss this in the next section.

1.4 The Hubble Tension and Late-Time Transition

Despite its remarkable success in explaining a wide range of cosmological observations, the Λ CDM model faces several growing challenges, the most prominent of which is the so-called *Hubble tension*, which is the main subject of the present thesis. This refers to the statistically significant discrepancy between the value of the Hubble constant H_0 inferred from early-Universe observations, primarily the cosmic microwave background (CMB) as measured by the Planck satellite [5], and that measured in the local Universe using distance ladder methods, such as those employed by the PANTHEON+ collaboration [1]. Planck data, under the assumption of Λ CDM, yields $H_0 = 67.4 \pm 0.5$ km/s/Mpc, while local measurements report a higher value, $H_0 = 73.5 \pm 1.1$ km/s/Mpc, resulting in a discrepancy exceeding 5σ . This tension has spurred intense theoretical and observational investigation, raising the possibility that new physics beyond Λ CDM may be required to reconcile these conflicting measurements, although another school of thought insists on accounting this tension in systematics.

While the Hubble tension stands as the most prominent challenge to the Λ CDM model, several other tensions have also emerged in recent years. These include the *S_8 tension*, a discrepancy between the amplitude of matter clustering inferred from CMB observations and that measured through weak lensing surveys [27], the so-called *cosmic dipole tension*, where the observed dipole in the distribution of quasars or radio galaxies appears inconsistent with the CMB dipole [28]. Additional issues include possible large-scale anomalies in the CMB [29], such as alignments of low multipoles and hemispherical asymmetries, and inconsistencies in growth-rate measurements and BAO-derived distances at low

redshifts [30]. While individually less significant than the Hubble tension, the convergence of these anomalies raises questions about the completeness of the standard cosmological model and puts significant challenges for the model. A nice and compact review and discussion of the aforementioned challenges is presented in [31].

In the present thesis, we focus on the Hubble tension and our work is motivated by the work of Perivolaropoulos and Skara [2], who test the homogeneity of the PANTEHON+ dataset [1] by proposing a late-time transition in the absolute magnitude of the Supernovae of Type Ia (SnIa). They are considering a flat Λ CDM cosmology and using a standard χ^2 minimization they test which model provides a better fit to the data, *i.e.* the standard flat Λ CDM or the transition model. They find that the transition model provides a better fit to the data after calculating the Akaike Information Criterion (AIC) with the transition occurring at a critical distance of approximately 20 Mpc. They further support the evidence of this critical distance, even after removing low redshift $z \leq 0.01$ data from the likelihood to account for the systematic effect of volumetric redshift scatter bias.

Our work builds on this analysis [2], where we start by reproducing their results for the flat Λ CDM via a χ^2 minimization and then expand the analysis to test the effect of the transitions in more models, including the cosmographic expansion up to $\mathcal{O}(z^2)$, the flat w_0 CDM model and the flat Chevallier-Polarski-Linder (CPL) model. We perform the inference of each model using a χ^2 minimization, a Monte Carlo Markov Chain (MCMC) sampling via *emcee* and Nested Sampling, a toolkit that allows us to extract best-fit values, contour plots and comparison among models.

1.5 Outline of the Thesis

In Chapter 2, we construct the mathematical and physical framework of our analysis. We begin by defining distances in cosmology and specifically the luminosity distance in 2.1 and we proceed with a short astrophysics intermezzo in section 2.2 where we discuss light’s inverse square law and astronomical magnitudes to make the connection to the luminosity distance and observables. Since our work focuses on the PANTHEON+ dataset, we build the distance ladder in section 2.3, showing how each rung calibrates the next one until we reach the Supernovae rung and we finish the chapter by defining the equations for the models of interest in sections 2.4–2.7.

In Chapter 3, we start by discussing the Frequentist and Bayesian methods of parameter inference in Sections 3.1–3.2. In section 3.3 we reproduce the results of Perivolaropoulos and Skara [2] of testing the effect of the late time transition using the same χ^2 minimization method. In sections 3.4–3.5, we repeat the same inference, this time in a Bayesian framework using an MCMC sampling and Nested Sampling respectively, and we compare the results from all three methods in section 3.5.

Having set up the framework for the Λ CDM model, we expand our analysis in Chapter 4 to include the cosmographic expansion model up to $\mathcal{O}(z^2)$ order, the w_0 CDM model and the CPL model. We infer the best-fit parameters, produce the contour plots and perform model comparison for each case and cross-reference between models.

The results and future extensions of this work are discussed in the final Chapter 5.

2 Distance Ladder and Type Ia Supernovae

2.1 Luminosity Distance

The focus of the present Thesis lies on the Hubble tension and inferring the Hubble parameter from Type Ia Supernovae(SnIa). This inference occurs via measuring distances to SnIa, so our first task would be to define distances in a cosmological context. The objects we're interested in are lying deep in the Universe, far away from us, where the cosmic expansion dominates. To measure distances to such objects, implies that we need to measure distances in an expanding space.

Measuring distances in astronomy is one of the most beautiful and at the same time challenging task, which begins by observing light rays emitted from astronomical objects. This very light is nothing else but electromagnetic radiation and its interpretation gives us a vast amount of information about our Universe. Since we're interested in an expanding space, let us start by writting the FRW metric once again:

$$ds^2 = -dt^2 + a^2(t) \left(\frac{dr^2}{1 - kr^2} + r^2 d\theta^2 + r^2 \sin^2 \theta d\phi^2 \right) \quad (2.1)$$

We distinguish three cases for the above metric, *i.e.* $k = -1, 0, 1$. It is useful to write this metric in a more general form, which includes all the allowed values for k in one expression:

- For $k = 1$, we set $r = \sin \chi$

In this case, FRW becomes: $ds^2 = -dt^2 + a^2(t) [d\chi^2 + \sin^2 \chi (d\theta^2 + \sin^2 \theta d\phi^2)]$

- For $k = 0$, we set $r = \chi$

In this case, FRW becomes: $ds^2 = -c^2 dt^2 + a^2(t) [d\chi^2 + \chi^2 (d\theta^2 + \sin^2 \theta d\phi^2)]$

- For $k = -1$, we set $r = \sinh \chi$

In this case, FRW becomes: $ds^2 = -c^2 dt^2 + a^2(t) [d\chi^2 + \sinh^2 \chi (d\theta^2 + \sin^2 \theta d\phi^2)]$

We can simply combine these three different cases in one, via

$$S_k(\chi) = \frac{1}{\sqrt{-k}} \sinh (\sqrt{-k} \chi) \quad (2.2)$$

so the FRW metric can be generally written as:

$$ds^2 = -dt^2 + a^2(t) [d\chi^2 + S_k^2(\chi) (d\theta^2 + \sin^2 \theta d\phi^2)] \quad (2.3)$$

Let us now define the luminosity distance, which is the distance measured in the PANTHEON+ survey. Let us assume an observer who has set a telescope and detects radiation from a distant astrophysical object. The energy received by the observer per time unit in a standard surface and in a frequency region is defined as the *flux of radiation*:

$$\mathcal{F} = \frac{l_0}{S} \quad (2.4)$$

where $S = 4\pi a_0^2 S_k^2(\chi)$ is the area of a sphere at $z = 0$ and l_0 is the energy per time unit we observe in a frequency region, at $\chi = 0$ and $z = 0$. In other words, l_0 is the *observed luminosity*. Therefore, we define as *absolute luminosity*, l_s , the total energy emitted from the source per time unit in a frequency region. Thus, we define *luminosity distance* as:

$$d_L^2 = \frac{l_s}{4\pi\mathcal{F}} \quad (2.5)$$

Using the definitions of flux in (2.4) and S , we obtain:

$$d_L^2 = a_0^2 S_k^2(\chi) \frac{l_s}{l_0} \quad (2.6)$$

To make clear how Cosmology is encoded in the luminosity distance, we need to find an expression for the ratio l_s/l_0 . Using De Broglie's principle from Quantum Mechanics, the energy of a photon is given by:

$$\Delta E = h\nu \quad (2.7)$$

where h is Planck's constant and ν is the frequency which is connected with the wavelength via: $c = \lambda\nu$. If we write the energy of light emitted at the time interval Δt_1 to be ΔE_1 and the energy we receive at Δt_0 to be ΔE_0 , then from luminosity's definition:

$$l_s = \frac{\Delta E_1}{\Delta t_1} \quad l_0 = \frac{\Delta E_0}{\Delta t_0} \quad (2.8)$$

Thus the ratio of luminosities is,

$$\frac{l_s}{l_0} = \frac{\Delta t_0}{\Delta t_1} \frac{\Delta E_1}{\Delta E_0} \quad (2.9)$$

Using the wave equation for the speed of light and equation (2.7), the ratio of energies is given by:

$$\frac{\Delta E_1}{\Delta E_0} = \frac{hv_1}{hv_o} = \frac{hc/\lambda_1}{hc/\lambda_0} = \frac{\lambda_0}{\lambda_1} \quad (2.10)$$

Using the definition of redshift (1.39), we find that:

$$\frac{\Delta E_1}{\Delta E_0} = \frac{\lambda_0}{\lambda_1} = 1 + z \quad (2.11)$$

For the ratio of time intervals we have:

$$c = \lambda v = \frac{\lambda}{\Delta t} \quad (2.12)$$

Since speed of light is constant:

$$\begin{aligned} c &= \frac{\lambda_0}{\Delta t_0} = \frac{\lambda_1}{\Delta t_1} \\ \Rightarrow \frac{\Delta t_0}{\Delta t_1} &= \frac{\lambda_0}{\lambda_1} = 1 + z \end{aligned} \quad (2.13)$$

Combining everything, we find that the ratio of the absolute luminosity over the observed one is equal to:

$$\frac{l_S}{l_0} = (1 + z)^2 \quad (2.14)$$

and the luminosity distance is thus given by:

$$d_L = a_0 S_k^2(\chi) (1 + z) \quad (2.15)$$

Redshift is now included in the expression as expected, but cosmology still remains hidden within $S_k^2(\chi)$. Combining the definition of the curvature density parameter (1.34) and (2.2), we can easily obtain:

$$S_k^2(\chi) = \frac{c}{a_0 H_0 \sqrt{\Omega_{k,0}}} \sinh \left(\sqrt{\Omega_{k,0}} \int_0^z \frac{d\tilde{z}}{E(\tilde{z})} \right) \quad (2.16)$$

where the speed of light was recovered to properly display the dimensions and we defined:

$$E(z) = \frac{H(z)}{H_0} \quad (2.17)$$

Therefore, luminosity distance can be expressed in the general form as:

$$d_L = \frac{c(1+z)}{H_0\sqrt{\Omega_{k,0}}} \sinh\left(\sqrt{\Omega_{k,0}} \int_0^z \frac{d\tilde{z}}{E(\tilde{z})}\right) \quad (2.18)$$

The models that we will later consider are all flat, therefore we can further simplify equation (2.18), by setting $\Omega_{k,0} = 0$, which yields:

$$d_L = c(1+z) \int_0^z \frac{d\tilde{z}}{H(\tilde{z})}$$

(2.19)

and the model under consideration is expressed via $H(z)$. This equation is a beautiful expression showing how measuring the distance to a set of astronomical objects can eventually yield useful information on our Universe. But, how can we measure the distance to such objects lying so far away? Via the distance ladder! But before that, let's discuss how to measure distances in astronomy.

2.2 Astronomical Magnitudes and the Distance Modulus

While the night sky offers a two-dimensional map of celestial positions, our goal is to unveil the third dimension of the Universe, *i.e.* measure the distance to a star, transforming this way flat star charts into a dynamic, three-dimensional cosmic landscape. Astronomy is all about detecting, receiving and eventually interpreting the electromagnetic radiation emitted by astronomical objects. Measuring the intrinsic brightness of stars is linked with determining their distances.

Kepler's laws in their original form describe the relative sizes of the planets' orbits in terms of astronomical units, since their actual dimensions were unknown to Kepler. The true scale of our Solar System was first unveiled in 1761, when the distance to Venus was measured as it crossed the Sun's disk in a rare transit during inferior conjunction. The method used was *trigonometric parallax*.

Trigonometric parallax is the most direct and geometric method for determining stellar distances. It relies on observing the apparent angular displacement of a nearby star against the distant background stars as Earth moves from one side of its orbit to the other. This angular shift, known as the *parallax angle* θ , is typically measured in arcseconds. The distance d to the star, expressed in parsecs, is given by [32, 33]:

$$d = \frac{1}{\theta} \text{pc} \quad (2.20)$$

where θ is the parallax angle in arcseconds. The larger the parallax angle, the closer the star is to Earth. Because of the small size of these angles, this method

cannot reach far enough in the Universe, where cosmology becomes important. Observations from the Gaia mission have achieved measuring stellar distances out to several kiloparsecs, with some bright stars being mapped even beyond 10 kpc [34].

Going further into the Universe, require the definition of the *magnitude scale*. Greek astronomer Hipparchus (2nd Century BCE) was one of the first sky watchers to catalog the stars that he saw. He compiled a list with the positions of 850 stars and he categorized them by inventing a numerical scale to describe their brightness. He called this scale, the magnitude scale, and he assigned $m = 1$ for the brightest star and $m = 6$ for the dimmest star. Since Hipparchus's time, astronomers had of course to refine this scale, after discovering much brighter and much dimmer stars. In the 19th century, it was thought that the human eye responded to the difference in logarithms of the brightness of two luminous objects. By the modern definition, a difference of 5 magnitudes (mag), corresponds exactly to a factor of 100 in brightness. That being said, a star with *apparent* (or observed) magnitude $m_1 = 1$ will be 100 times brighter than a star of $m_2 = 6$. If we denote brightness by \mathcal{F} , we can write:

$$\frac{\mathcal{F}_2}{\mathcal{F}_1} = 100^{(m_1 - m_2)/5} \quad (2.21)$$

This equation holds in general for any stars of magnitudes m_1 and m_2 .

The brightness of a star is actually measured in terms of the *radiant flux*, \mathcal{M} , received from the star. The radiant flux is defined to be the total amount of light energy of all wavelengths that crosses a unit area oriented perpendicular to the direction of the light's travel per unit time ; that is the number of joules of starlight energy per second received by one square meter of a detector aimed at the star. It is therefore depending on the intrinsic luminosity and the distance of the star from the observer. That is, the same star would appear less bright in the sky if it was located farther from the Earth. Assuming that a star of intrinsic luminosity L is surrounded by a huge spherical shell of radius d , this leads to the formulation of the *light's inverse square law*:

$$\mathbf{F} = \frac{L}{4\pi d^2} \quad (2.22)$$

which we have already silently used above when we defined the luminosity distance in the cosmological context 2.5. Working out equation (2.21) yields:

$$m_1 - m_2 = -2.5 \log \frac{\mathcal{F}_\infty}{\mathcal{F}_\epsilon} \quad (2.23)$$

In most of observations and especially in the SnIa which we're interested in, we don't care about differences in apparent magnitudes between stars, but about the magnitude of each star individually. Therefore, we can assign an *absolute*

magnitude, M to each star and define it as the apparent magnitude that the star would have if it were located at a distance of exactly 10 pc from us. The absolute magnitude can be thus also interpreted as the intrinsic luminosity of the star. Setting $m_1 = m$ and $m_2 = M$ in (2.21), and using light's inverse square law (2.22), we can easily derive the famous distance modulus equation written in Mpc units:

$$\mu \equiv m - M = 5 \log \frac{d}{1\text{Mpc}} + 25 \quad (2.24)$$

This is one of the most important equations in astronomy and observational cosmology and of course in this thesis. This equation provides the link between theory and observations by plugging in the luminosity distance equation for a given model (2.19). Let us now see how we can exploit the physical properties of some stellar objects so we can use this equation to infer Cosmology information!

2.3 Distance Ladder

2.3.1 Cepheid Variable Start

We've seen that the parallax method is a simple method that can impressively reach out to a few kiloparsecs, but unfortunately this does not meet our requirements, since we're interested in the Mpc scale. We need to measure distances to objects located farther away, so the Universe's expansion becomes important. Thankfully, the sky is full of astronomical objects with specific properties that allow us to measure larger distances. An important class of these objects are the Cepheid variable stars. Cepheids are luminous pulsating stars, the brightness of which is correlated to their period. That is, the brighter the star, the longer the pulsation period. It is therefore clear that Cepheids obey a period-luminosity relation which was first discovered by Henrietta Swan Leavitt (1868-1921) in Harvard [35]. Her tedious task was to compare two photographs of the same field of stars taken at different times and detect any star that varied in brightness. Eventually, she discovered 2400 classical Cepheids with periods between 1 and 50 days, most of them located in the Small Magellanic Cloud (SMC). She noticed that the more luminous stars took longer to go through their pulsation cycles and she plotted the apparent magnitudes of these SMC stars against their pulsation periods, demonstrating the correlation between the brightness and the period of Cepheid stars. This correlation is known as the Leavitt law and it's expressed as:

$$M = \alpha \log_{10} P + b \quad (2.25)$$

where M is the intrinsic brightness of the Cepheid, *i.e.* its apparent magnitude, P is the period, α is the slope of the relation indicating how luminosity changes with period and b is the interception, representing the magnitude for a given

reference period. Given that the period-luminosity relation is of universal character, in principle, we only need to know the distance to one Cepheid star, so we can infer the values of α and b , and since these are constants, they will always be the same. This is where parallax comes in the game, to calibrate the period-luminosity relation. Thankfully, there are many Cepheid stars close enough to us, making the measurement of their distances possible and precise via the trigonometric parallax method. Once Cepheid stars have been detected, their apparent magnitudes are being measured using photometry. This measurement is not an easy one and it requires a lot of work, the discussion of which goes far beyond the scope of the present thesis. For a nice overview of how detectors, telescopes and photometry are being applied, see [32], and for more technical applications see [36, 37, 38, 39]. Once the Cepheids' apparent magnitudes have been measured and their distances are already known via the trigonometric parallax, all one has to do is to plug them in the distance modulus relation (2.24) and infer M . Then, since the period is also known, one can solve for α and b and calibrate the period-luminosity relation. This is how the ladder is being built, using parallax as the first rung to get to the second rung, *i.e.* the Cepheids.

It is worth mentioning here that there is no single, universal period–luminosity relation applicable to all Cepheids. The form of the relation depends on several astrophysical and observational factors. First, the slope and zero-point vary with the photometric band used; infrared observations tend to yield tighter relations with reduced sensitivity to interstellar extinction [40]. Second, metallicity plays a non-negligible role, particularly in optical bands, where metal-rich Cepheids may appear intrinsically brighter or fainter than their metal-poor counterparts at the same period [41]. Lastly, the inclusion of a color term or use of reddening-free Wesenheit magnitudes leads to refined Period–Luminosity–Color relations that mitigate scatter due to temperature and extinction effects [42]. These dependencies must be carefully accounted in precise distance measurements, especially when calibrating extragalactic distance ladders.

Thanks to high-resolution imaging from the Hubble Space Telescope, Cepheid variable stars have been observed and used to calibrate distances out to approximately 40 Mpc [43, 44], with even greater reach achieved using near-infrared observations from JWST [45]. Beyond this range, their intrinsic brightness becomes insufficient for detection in most galaxies, and they are gradually superseded by Type Ia supernovae in the cosmic distance ladder, which is the next step of the ladder!

Before moving on to the next rung of the ladder, let us provide some reference, to understand how far we are and how even further we aim to reach. Let us assume that we measured the distance to a Cepheid to be equal to 20 Mpc. In meters, this is translated to $d_{Ceph} = 61.72 \times 10^{22}$ m. Let us compare this to the distance to the Sun:

$$\frac{d_{Ceph}}{d_\odot} = \frac{61.72 \times 10^{22} \text{m}}{147.22 \times 10^9 \text{m}} \simeq 0.42 \times 10^{13} \simeq 10^{12}$$

meaning that the distance to a Cepheid star is a trillion times larger than the distance to the Sun, and we're still not happy with that!

2.3.2 Type Ia Supernovae

We're trying to reach to distances more than 40 Mpc, implying that the objects we want to observe should be extremely bright! Fortunately, nature took care of that, providing us with Supernovae! A Supernova (SN) is a powerful and luminous explosion that occurs when certain types of stars reach the end of their lifetimes and they can outshine entire galaxies for a short period of time, releasing enormous amounts of energy. SNe are extremely important objects in astronomy and cosmology. Supernovae are among the most energetic and informative phenomena in astrophysics, with a wide range of types and rich underlying physics. Their breadth is such that it could easily fill an entire thesis or book and goes beyond our scope. In this work, we restrict our attention on *Type Ia supernovae* (SnIa), due to their well-established role as standard candles in cosmology.

Type I SNe, happen in binary systems, where one of the stars is a white dwarf. If the white dwarf accumulates too much material from its companion star, it can reach a critical mass of $m = 1.4M_\odot$, known as the Chandrasekhar limit [46], which triggers a runaway nuclear reaction, leading to an enormous, beautiful, glorious but also catastrophic explosion. A key feature of this type of SNe is that their spectral lines are hydrogen-free. Type I SNe can be further categorized into type Ia, Ib and Ic, depending on their spectral lines. Our interest here is restricted to SnIa, so we will only focus on them and neglect the other types. For a comprehensive discussion of all types of SNe, see [32].

SnIa occur in binary systems when the white dwarf gains material from its companion star, reaching this way the Chandrasekhar limit and resulting to an explosion. A key characteristic of them that makes them easily detectable, is that their spectral lines present a strong silicon absorption line, while neither Hydrogen nor Helium are found. What makes these objects special, is that their decline rate is correlated to their brightness. Specifically, a SnIa increases its brightness gradually while heading to an explosion and it reaches its peak brightness at some point. Afterwards, the brightness is gradually fading out, defining the decline rate. An intrinsic property of all SnIa is that the brighter they are, the longer their decline rate is. This is the physical property on which we can build one and use SnIa to extract cosmology information, but first, let us present in a nutshell how SnIa are being detected and then how this physical intrinsic property can be exploited.

1. Detection of SnIa

Detecting SnIa involves astronomical observation techniques combined with follow-up analyses to confirm their nature. It starts with wide-field surveys, using wide-field telescopes to capture repeated images of the same region of the sky over time, which are then compared to identify “new” sources of light that were not present in earlier images. The technology being used involves automated software analyzing images, looking for changes in brightness or new point sources [47].

2. Light Curve Observations

Once a candidate SN is detected, astronomers track its brightness over time to build a light curve $m = m(t)$, searching for the signature property of SnIa, *i.e.* a light curve reaching gradually at its peak and then slowly decline.

3. Spectroscopic Confirmation

The telescope is usually equipped with a spectograph that spreads the light into its component wavelengths. Spectra showing strong silicon absorption lines and no hydrogen or helium correspond to SnIa [48, 49, 50].

4. Photometric Redshift Measurement

For very distant SNe, obtaining a spectrum might not always be feasible. Instead a multi-band photometry that observes the object in different color filters, can estimate its redshift and classify the SN as Ia based on its color and light-curve shape [51, 52, 53].

5. Host Galaxy Analysis

Identifying host galaxies is of crucial importance, since it provides us with additional clues that can help later with calibrating their distance.

6. Capturing the Light

Light is being captured using charge-coupled device (CCD) cameras and then being passed through filters to measure the SN brightness in specific wavelengths, *e.g.* B-band, V-band, etc [54].

7. Photometry

Aperture or Point-Spread-Function photometry is being used to analyze the detected light [55].

8. Using Filters to Isolate Wavelengths

Use of filters to isolate specific parts of the electromagnetic spectrum,

measuring this way apparent magnitudes in specific bands [56].

9. Calibrating the Brightness

To ensure an accurate measurement of the brightness, the raw brightness data need to be calibrated and correct for detector sensitivity and remove instrumental noise [57].

10. Converting Brightness to Apparent Magnitude

Once brightness is calibrated, it can be converted to apparent magnitude via equation (2.23), by choosing a reference flux for which $m_2 = 0$ and brightness is already known [57].

11. Correcting for extinction

Galactic and host-galaxy extinction affect the observed brightness of the SNe. This requires applying a wavelength dependent correction for extinction, using a color excess $E(B - V)$, typically derived from observations in multiple filters:

$$A_\lambda = R_\lambda E(B - V)$$

where A_λ is extinction at wavelength λ and R_λ is the extinction coefficient, often $\simeq 3.1$ for the Milky Way in the V-band [58].

12. Accounting for background light

If the SN is located in a crowded background, the background light needs to be subtracted to avoid contaminating the measurement. This is usually done by taking images of the region after the SNe have faded and subtract its background from the original images [59].

13. Building a Light Curve

Once all corrections have been applied, a clean light curve can be finally constructed [60, 61] Check figure 1 for a typical SnIa light curve.

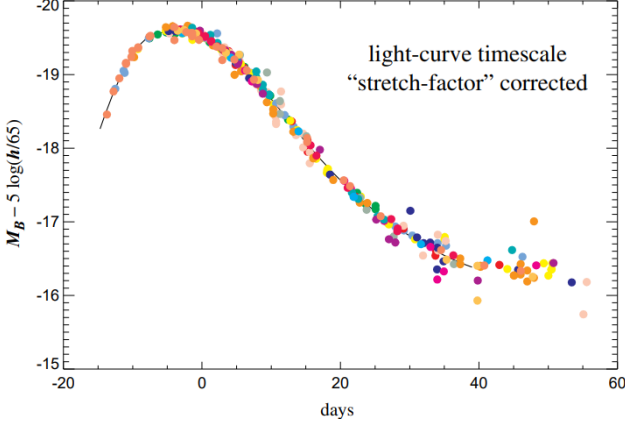


Figure 1: Example of a supernova light curve. The stretch correction applied here is discussed in section 2.3.2. Adapted from [60]

This is the process of a Supernova survey in a nutshell. Going through each one of the items with detail is more than enough to write an extra thesis on top of the present one. Since our interest is centered on parameter inference, our goal here was to only briefly demonstrate how the process works and not dive into more detail, which can of course be found in the given references.

Now that the SNe have been detected, let us discuss their calibration. Our goal is to eventually measure the distance to the SNe, meaning that we need to know their absolute magnitude. Exploiting their intrinsic property of their brightness being correlated with their decline rate, following the Cepheid example in section 2.3.1, we can define the following relation:

$$M = \alpha \Delta m_{15} + \beta \quad (2.26)$$

where α and β are the coefficients that we need to determine and Δm_{15} is the decline rate of the magnitude after 15 days. This relation is known as the *Phillips relation* [62]. Measuring the distance to at least one SnIa, can in principle constrain the coefficients and calibrate the Phillips relation. Fortunately, there are nearby SnIa residing in same galaxies as Cepheid stars. Therefore, since they are in the same galaxy with a Cepheid star, the distance to which is known, we can plug this distance in (2.24) and calculate the absolute magnitude for the SnIa, calibrating this way the Phillips relation. This is how Cepheid stars provide the rung to reach to the further away located SNe and the distance ladder is now complete -at least for our scope.

In addition to calibration, a few observational effects must be accounted for before comparing supernova magnitudes across a wide redshift range. One such effect is *time dilation*, a natural consequence of cosmic expansion, which

stretches the observed light curve of distant supernovae [63]. Another is the *K-correction*, which accounts for the fact that supernovae observed at different redshifts are measured through filters that correspond to different rest-frame wavelengths. These corrections are essential for comparing light curves consistently across redshifts [64].

Once all corrections have been applied, it's time to use the physical property of the SnIa well-calibrated intrinsic brightness, due to the fact that they follow a predictable physical process leading to the explosion, which is the thermonuclear explosion of a white dwarf at or near the Chandrasekhar limit. This means that we can consider all of the light curves that we have available from a given observation and apply corrections to create a single light curve, which will be the reference point for starting a cosmological analysis. This process is what's making SnIa standardizable candles.

While the Phillips relation provides a useful conceptual foundation, modern analyses adopt more refined empirical models to standardize SnIa with greater precision. Surveys like *Pantheon+* do not use Equation (2.26) directly; instead, they rely on light-curve fitters such as **SALT2** (Spectral Adaptive Lightcurve Template 2), which model the SnIa flux as a function of time and wavelength using a training set of observed light curves [65, 1]. The model includes two main parameters: a *stretch parameter* x_1 , which accounts for the width of the light curve (analogous to the decline rate), and a *color parameter* c , which captures reddening due to dust and intrinsic color variation. These corrections are applied through a standardized relation for the distance modulus:

$$\mu = m_B - M + \alpha x_1 - \beta c \quad (2.27)$$

where m_B is the observed peak magnitude, and α , β , and M are nuisance parameters fitted during cosmological analysis. Alternative methods such as **MLCS2k2** use a more model-driven approach, constructing template light curves and explicitly modeling extinction using A_V and R_V [66]. These tools allow for robust standardization across large and heterogeneous SN datasets spanning a wide range of redshifts and survey conditions.

In the following sections 3 & 4 we will use the PANTHEON+ dataset to test different cosmological models. Now that a compact description of a Supernova survey is given, let us describe the process presented in PANTHEON+, summarizing this way all of the aforementioned concepts and technique in one, compact paragraph.

The Pantheon+ compilation represents one of the most comprehensive and rigorously standardized Type Ia supernova datasets to date. The team reprocessed and homogenized photometric data from 18 different surveys, totaling 1701 spectroscopically confirmed SnIa across a redshift range of $0.001 < z < 2.26$. Each supernova was standardized using the **SALT2** light-curve fitter, which

extracts three key parameters: the peak B -band apparent magnitude (m_B), a stretch parameter (x_1), and a color parameter (c). These were combined into a corrected distance modulus (2.27) with the nuisance parameters α , β , and M determined globally in a cosmological fit. The absolute calibration of the supernova sample—*i.e.*, fixing the value of M —was anchored using Cepheid distances from the SH0ES program [67], which measured high-precision distances to nearby SN-host galaxies via the Leavitt law. The final Pantheon+ data release includes light-curve parameters, covariance matrices, and a full treatment of systematics, enabling consistent and transparent cosmological analyses. For the remaining of this session, we will define the models that we will put to test and check the effect of a late-time transition in the SnIa absolute magnitude.

2.4 Flat Λ CDM

A flat Λ CDM model is already described in section 1.3 where we derived that the associated Friedmann equation is given by (1.40). To infer the parameters associated with the Λ CDM model, we first need to define the luminosity distance for this model. Plugging (1.40) into (2.19) yields:

$$d_L = c(1+z) \int_0^z \frac{d\tilde{z}}{H_0 \sqrt{\Omega_{m,0} (1+\tilde{z})^3 + 1 - \Omega_{m,0}}} \quad (2.28)$$

Making the connection to the observables via (2.24) yields:

$$m - M = 5 \log_{10} \left[\frac{c(1+z)}{1 \cdot \text{Mpc}} \int_0^z \frac{d\tilde{z}}{H_0 \sqrt{\Omega_{m,0} (1+\tilde{z})^3 + 1 - \Omega_{m,0}}} \right] + 25 \quad (2.29)$$

with the parameters need to be inferred being M , H_0 and $\Omega_{m,0}$. It becomes clear from this equation that M and H_0 are degenerate. However, this degeneracy may be broken under PANTHEON+, because Cepheid hosted SnIa are included, meaning that M can be calculated using only these SnIa.

2.5 Cosmographic Expansion

When we demonstrated the cosmological principle in refs1.1, we show that on small scales, matter is distributed in a highly irregular way but, as we look on larger and larger scales, the matter distribution looks more and more uniform. Hubble also demonstrated in his famous paper [20], that galaxies lying further away, *i.e.* on larger redshifts were appeared to be moving away further than the ones lying closest to us. We hence realize that things can become interesting in smaller scales. This motivates us to perform a Taylor expansion so we can find an expression that would bin different redshift regimes and examine the behavior on these regimes via some parameters. We start by Taylor expanding

the scale factor $a(t)$ around the present time t_0 :

$$a(t) = \sum_{n=0}^{\infty} \frac{1}{n!} \left. \frac{d^{(n)}a(t)}{dt^n} \right|_{t=t_0} (t-t_0)^n$$

$$= a_{t_0} + \dot{a}(t_0)(t-t_0) + \frac{1}{2}\ddot{a}(t_0)(t-t_0)^2 + \frac{1}{6}\left. \frac{d^3a(t)}{dt^3} \right|_{t=t_0} (t-t_0)^3 + \frac{1}{24}\left. \frac{d^4a(t)}{dt^4} \right|_{t=t_0} (t-t_0)^4 + \dots$$

We can express the derivatives via parameters defined as [68]:

$$H(t) = \frac{1}{a} \frac{da}{dt} \quad (2.30)$$

$$q(t) = -\frac{1}{a} \frac{d^2a}{dt^2} \left[\frac{1}{a} \frac{da}{dt} \right]^{-2} \quad (2.31)$$

$$j(t) = \frac{1}{a} \frac{d^3a}{dt^3} \left[\frac{1}{a} \frac{da}{dt} \right]^{-3} \quad (2.32)$$

$$s(t) = \frac{1}{a} \frac{d^4a}{dt^4} \left[\frac{1}{a} \frac{da}{dt} \right]^{-4} \quad (2.33)$$

where q_0 is called the deceleration parameter, j_0 the jerk parameter and s_0 the snap parameter. Plugging these definitions into the expansion of the scale factor yields:

$$a(t) = a(t_0) \left[1 + H_0(t-t_0) - \frac{1}{2}q_0 H_0^2(t-t_0)^2 + \frac{1}{6}j_0 H_0^3(t-t_0)^3 + \frac{1}{24}s_0 H_0^4(t-t_0)^4 + \mathcal{O}((t-t_0)^5) \right] \quad (2.34)$$

Our goal is to derive the expression for the luminosity distance for a cosmographic expansion. The first step is to express everything in terms of redshift, which is the observable. From (1.39) it becomes clear that we need to perform a Taylor expansion of the inverse scale factor, which is:

$$\frac{1}{a(t)} = \frac{1}{a(t_0)} + \frac{d}{dt} \left[\frac{1}{a(t)} \right] \Big|_{t=t_0} (t-t_0) + \frac{1}{2} \frac{d^2}{dt^2} \left[\frac{1}{a(t)} \right] \Big|_{t=t_0} (t-t_0)^2$$

$$+ \frac{1}{6} \frac{d^3}{dt^3} \left[\frac{1}{a(t)} \right] \Big|_{t=t_0} (t-t_0)^3 + \frac{1}{24} \frac{d^4}{dt^4} \left[\frac{1}{a(t)} \right] \Big|_{t=t_0} (t-t_0)^4$$

After a lot of tedious algebra to calculate the derivatives, we truncate the expansion to not include higher than fourth order and we derive:

$$\begin{aligned}\frac{1}{a(t)} &= \frac{1}{a(t_0)} - \frac{1}{a(t)} H_0 (t - t_0) + \frac{1}{2} \left[\frac{2 + q_0}{a(t_0)} H_0^2 \right] (t - t_0)^2 \\ &\quad + \frac{1}{6} \left[\frac{-6H_0^3 - 6q_0 H_0^3 - j_0 H_0^3}{a(t_0)} \right] (t - t_0)^3 \\ &\quad + \frac{1}{24} \left[\frac{24H_0^4 + 36q_0 H_0^4 + 6q_0 H_0^4 + 8j_0 H_0^4 - s_0 H_0^4}{a(t_0)} \right] (t - t_0)^4\end{aligned}$$

The time is not something that we can usually calculate, so it will be convenient to replace it with something that we can observe, even in an intermediate way. Since we're interested in light rays travelling from SNIa, the physical distance travelled by a photon that is emitted at time t and observed at time t_0 is given by:

$$D = c \int_t^{t_0} dt \Rightarrow D = c(t_0 - t) \quad (2.35)$$

Substituting this into the Taylor expansion of the inverse scale factor and using the redshift definition (1.39) yields:

$$\begin{aligned}1 + z &= 1 + \frac{H_0 D}{c} + \frac{2 + q_0}{2} \frac{H_0^2 D^2}{c^2} + \frac{6(1 + q_0) + j_0}{6} \left(\frac{H_0 D}{c} \right)^3 \\ &\quad + \frac{24 - s_0 + 8j_0 + 36q_0 + 6q_0^2}{24} \left(\frac{H_0 D}{c} \right)^4\end{aligned} \quad (2.36)$$

However, what we want to measure is the distance and not the redshift of course. We now have a function $z(D)$ and we want to make it $D(z)$. This is a standard practice where one uses series inversion. After quite some tedious but straightforward algebra, we can easily derive:

$$\begin{aligned}D(z) &= \frac{cz}{H_0} \left[1 - \left(1 + \frac{q_0}{2} \right) z + \left(1 + q_0 + \frac{q_0^2}{2} - \frac{j_0}{6} \right) z^2 \right. \\ &\quad \left. - \left(1 + 3q_0(1 + q_0) + \frac{5}{8}q_0^3 - \frac{1}{2}j_0 - \frac{5}{12}q_0 j_0 - \frac{s_0}{24} \right) z^3 \right]\end{aligned} \quad (2.37)$$

This is the most general form of Hubble's law and we verify that for nearby SNe, *i.e.* for $z \ll 1$ it reduces to the original famous form.

Unfortunately, physical distance is not the variable in terms of which Hubble's law is observationally presented. This role is usually played by the luminosity distance, which we have already defined in section 2.1 and equation (2.15). Let us now see how we can express it in a cosmographic expansion context.

A photon emitted at coordinate origin $r = 0$ and time t_* reaches a comoving observer-an observer moving solely due to the expansion of the Universe, *i.e.* the Hubble flow- at $r = r_0$ and time t_0 . The redshift is related to the scale factor at emission, and the proper distance at reception is given by $D = a_0 r_0$. Combining these geometric relations leads directly to:

$$d_L = \frac{a_0}{a(t_0 - D/c)} a_0 r_0 \quad (2.38)$$

without requiring assumptions about the energy content of the Universe. We see from this equation that in order to calculate the luminosity distance we first need to derive an expression for $r_0(D)$. We have considered a photon in an FRW Universe, which follows a null geodesic, implying from (1.2) that,

$$\int_{t_*}^{t_0} \frac{cdt}{a(t)} = \int_0^{r_0} \frac{dr}{\sqrt{1 - kr^2}} = f(r_0) \quad (2.39)$$

For different values of curvature, the above integral gives:

$$f(r_0) = \begin{cases} \sin^{-1}(r_0), & \text{if } k = +1 \\ r_0, & \text{if } k = 0 \\ \sinh^{-1}(r_0), & \text{if } k = -1 \end{cases} \quad (2.40)$$

It is obvious from (2.39) that:

$$r_0(D) = f^{-1} \left(\int_{t_0 - D/c}^{t_0} \frac{cdt}{a(t)} \right) \quad (2.41)$$

Substituting (2.40) yields:

$$r_0(D) = \begin{cases} \sin \left(\int_{t_0 - D/c}^{t_0} \frac{cdt}{a(t)} \right), & \text{if } k = +1 \\ \int_{t_0 - D/c}^{t_0} \frac{cdt}{a(t)}, & \text{if } k = 0 \\ \sinh \left(\int_{t_0 - D/c}^{t_0} \frac{cdt}{a(t)} \right), & \text{if } k = -1 \end{cases} \quad (2.42)$$

which can be equivalently written in a compact form as:

$$r_0(D) = \frac{1}{\sqrt{k}} \sinh \left(\sqrt{-k} \int_{t_0 - D/c}^{t_0} \frac{cdt}{a(t)} \right) \quad (2.43)$$

which is equivalent to equation (2.18). This equation can be easily Taylor expanded, giving:

$$r_0(D) = \int_{t_0-D/c}^{t_0} \frac{cdt}{a(t)} - \frac{k}{6} \left[\int_{t_0-D/c}^{t_0} \frac{cdt}{a(t)} \right]^3 + \dots \quad (2.44)$$

From equation (2.36), which is basically the result of the Taylor expansion of the inverse scale factor, we can write the integral of equation (2.44) as:

$$\begin{aligned} \int_{t_0-D/c}^{t_0} \frac{cdt}{a(t)} &= \int_{t_0-D/c}^{t_0} \frac{cdt}{a(t_0)} \left[1 + H_0(t-t_0) + \left(\frac{2+q_0}{2} H_0^2 \right) (t-t_0)^2 \right. \\ &\quad \left. + \frac{1}{6} (6+6q_0+j_0) (t-t_0)^3 + \mathcal{O}(t-t_0)^4 \right] \end{aligned}$$

Solving the integral easily yields:

$$\begin{aligned} \int_{t_0-D/c}^{t_0} \frac{cdt}{a(t)} &= \frac{D}{a_0} \left[1 + \frac{1}{2} \frac{H_0 D}{c} + \frac{2+q_0}{6} \left(\frac{H_0 D}{c} \right)^2 + \right. \\ &\quad \left. \frac{6+6q_0+j_0}{24} \left(\frac{H_0 D}{c} \right)^3 + \mathcal{O} \left(\frac{H_0 D}{c} \right)^4 \right] \end{aligned} \quad (2.45)$$

Plugging this result into the expression for $r_0(D)$ in (2.44) yields

$$\begin{aligned} r_0(D) &= \frac{D}{a_0} \left[1 + \frac{1}{2} \frac{H_0 D}{c} + \frac{1}{6} \left(2+q_0 - \frac{kc^2}{a_0^2 H_0^2} \right) \left(\frac{H_0 D}{c} \right)^2 + \right. \\ &\quad \left. \frac{1}{24} \left(6+6q_0+j_0 - 6 \frac{kc^2}{a_0^2 H_0^2} \right) \left(\frac{H_0 D}{c} \right)^3 + \mathcal{O} \left(\frac{H_0 D}{c} \right)^4 \right] \end{aligned} \quad (2.46)$$

We have now all the expressions that we need, to finally write the full equation for the luminosity distance in the context of a cosmographic expansion. Combining (2.38), (2.36) and (2.46) yields:

$$\begin{aligned} d_L(z) &= \frac{cz}{H_0} \left[1 + \frac{1}{2} (1-q_0)z - \frac{1}{6} \left(1-q_0 - 3q_0^2 + j_0 + \frac{kc^2}{H_0^2 a_0^2} \right) z^2 \right. \\ &\quad + \frac{1}{24} \left(2-2q_0-15q_0^2-15q_0^3+10q_0j_0+5j_0+s_0+2(1+3q_0)\frac{kc^2}{H_0^2 a_0^2} \right) z^3 \\ &\quad \left. + \mathcal{O}(z^4) \right] \end{aligned} \quad (2.47)$$

Later in Section 4.1, we will fit a cosmographic expansion to the PAN-THEON+ data, but we will consider only the q_0 parameter, so we will discard redshift of order higher than 2. The distance modulus in this case will be given

by:

$$m - M = 5 \log_{10} \left[\frac{cz}{H_0 \cdot \text{Mpc}} \left(1 + \frac{1}{2}(1 - q_0)z \right) \right] + 25 \quad (2.48)$$

2.6 Flat w_0 CDM Model

Let us now consider the simplest model for a dynamical dark energy component—known as the flat w_0 CDM model. This framework extends the standard Λ CDM model by allowing the dark energy equation of state to deviate from the cosmological constant value $w = -1$. Instead, the dark energy pressure-to-density ratio is parametrized by a constant w_0 , such that:

$$p_{\text{DE}} = w_0 \rho_{\text{DE}} \quad (2.49)$$

Assuming a spatially flat Universe ($k = 0$), the first Friedmann equation takes the form:

$$H^2(z) = H_0^2 \left[\Omega_m (1+z)^3 + (1-\Omega_m)(1+z)^{3(1+w_0)} \right] \quad (2.50)$$

where the final term corresponds to the dark energy density evolving as:

$$\rho_{\text{DE}}(z) = \rho_{\text{DE},0} (1+z)^{3(1+w_0)} \quad (2.51)$$

In contrast to a cosmological constant, where ρ_Λ remains constant with redshift, the w_0 CDM model introduces redshift dependence into the dark energy sector. For $w_0 < -1$, the model enters the so-called *phantom regime*, while $w_0 > -1$ implies a less dominant dark energy component in the past.

The aim of including this model is to test whether the data support a constant but non -1 value of w_0 , and test the effect of a late-time transition in the magnitude on the model. Observational constraints on w_0 are typically derived from distance indicators like Type Ia supernovae, baryon acoustic oscillations (BAO), and the cosmic microwave background (CMB).

For more on the development and application of this model, see [69, 70, 71], where the behavior and observability of w_0 CDM were first thoroughly examined in cosmological data analyses.

We will infer this model using the PANTHEON+ dataset in section 4.2. The distance modulus for this model is found by combining (2.50)

$$m - M = 5 \log_{10} \left[c(1+z) \int_0^z \frac{d\tilde{z}}{H_0 \sqrt{\Omega_m (1+\tilde{z})^3 + (1-\Omega_m)(1+\tilde{z})^{3(1+w_0)}}} \right] \quad (2.52)$$

2.7 Flat Chevallier-Polarski-Linder Model

The *CPL model*, introduced by Chevallier and Polarski [69] and later extended by Linder [70], generalizes the dark energy equation of state by allowing it to evolve with redshift. Unlike the constant- w_0 CDM model, the CPL parametrization captures possible time variation of the dark energy component in a simple and observationally tractable form:

$$w(z) = w_0 + w_a \frac{z}{1+z}, \quad (2.53)$$

where w_0 is the present-day value of the equation of state and w_a quantifies its rate of change. This form ensures that $w(z) \rightarrow w_0 + w_a$ at early times ($z \rightarrow \infty$) and $w(z) \rightarrow w_0$ at the present epoch ($z = 0$).

In a spatially flat Universe, the Hubble parameter evolves as:

$$H^2(z) = H_0^2 \left[\Omega_m (1+z)^3 + (1-\Omega_m)(1+z)^{3(1+w_0+w_a)} \exp\left(\frac{-3w_a z}{1+z}\right) \right]. \quad (2.54)$$

The CPL model is particularly useful for identifying potential departures from a cosmological constant by examining how the dark energy evolves over time. For $w_a = 0$, the model reduces to the w_0 CDM case. If both $w_0 = -1$ and $w_a = 0$, one recovers the Λ CDM model.

This parametrization is widely used in cosmological analyses due to its simplicity and flexibility, and is frequently constrained by data from supernovae, BAO, and CMB measurements. We will infer the parameters for CPL model and test the effect of a late-time transition in section 4.3. The distance modulus for this model is given by:

$$m-M = 5 \log_{10} \left[\frac{c(1+z)}{1 \cdot \text{Mpc}} \int_0^z \frac{d\tilde{z}}{H_0 \sqrt{\Omega_m (1+\tilde{z})^3 + (1-\Omega_m)(1+\tilde{z})^{3(1+w_0+w_a)} \exp\left(\frac{-3w_a \tilde{z}}{1+\tilde{z}}\right)}} \right] + 25 \quad (2.55)$$

3 Frequentist & Bayesian Inference for a flat Λ CDM Model

Over the last 25 years, Cosmology has shifted from a data-starved science to a data-driven scientist [72]. A vast amount of data is now available and many more data are about to come, so the development and application of statistical methods and techniques in Cosmology has increased significantly over the past years.

In Cosmology, the goal is usually to fit various cosmological models to the data available, infer their associated parameters, check the fit that they provide and draw conclusions based on the results. There are two main way to do that:

- **Frequentist Statistics:** Interprets probability as the long-run frequency of events. Parameters are fixed but unknown, and data is considered random. Inference is typically done via hypothesis testing and confidence intervals.
- **Bayesian Statistics:** Interprets probability as a measure of belief or certainty. Parameters are treated as random variables with prior distributions, and inference is based on updating these priors using Bayes' theorem to obtain posterior distributions.

In what follows, we will apply both methods to infer the parameters of the models under consideration, produce the contour plots and compare the models among each other. In this section, we will only work on the flat Λ CDM model and the rest of the models will be discussed in section 4.

3.1 Frequentist and χ^2 Statistics

We are fitting a flat Λ CDM model into the PANTHEON+ data, via a χ^2 minimization. Let us start by describing how the method works. The χ^2 method evaluates how well a model fits a set of observational data by quantifying the discrepancy between observed values and model predictions. For each data point, a residual is computed as the difference between the observed quantity and its corresponding predicted value from the model. These residuals are collected into a vector \vec{Q} .

To account for measurement uncertainties and correlations between data points, the residuals are weighted by the inverse of the covariance matrix C , which includes both statistical and systematic uncertainties. The χ^2 function is then defined as:

$$\chi^2 = \vec{Q}^T C^{-1} \vec{Q}. \quad (3.1)$$

Minimizing this function with respect to the model parameters yields the best-fit values that most closely match the data. To estimate the uncertainties in the best-fit parameters, one typically evaluates the curvature of the χ^2 surface around its minimum. This is done using the Fisher information matrix, defined as:

$$F_{ij} = \frac{1}{2} \frac{\partial^2 \chi^2}{\partial p_i \partial p_j}, \quad (3.2)$$

where p_i and p_j are the model parameters. The inverse of the Fisher matrix provides an estimate of the covariance matrix of the parameters, and the square roots of its diagonal elements give the 1σ uncertainties. This approach allows for a rigorous, quantitative comparison between theoretical models and observational data.

3.2 Bayesian Inference

In the Bayesian framework, inference is performed by updating prior beliefs about model parameters in light of observed data. This is formalized through Bayes' theorem:

$$P(\vec{\theta} | \vec{D}) = \frac{P(\vec{D} | \vec{\theta}) P(\vec{\theta})}{P(\vec{D})}, \quad (3.3)$$

where $\vec{\theta}$ denotes the vector of model parameters and \vec{D} represents the data. The term $P(\vec{\theta} | \vec{D})$ is the *posterior* probability distribution, reflecting our updated knowledge about the parameters after observing the data. $P(\vec{D} | \vec{\theta})$ is the *likelihood*, quantifying how well the model with parameters $\vec{\theta}$ explains the data. $P(\vec{\theta})$ is the *prior*, encoding knowledge or assumptions about the parameters before seeing the data. The denominator $P(\vec{D})$, known as the *evidence*, serves as a normalization constant and is often ignored in parameter estimation.

Bayesian inference typically involves sampling from the posterior distribution using techniques such as Markov Chain Monte Carlo (MCMC). From the posterior, one can compute summary statistics (mean, median, credible intervals) to estimate parameter values and their uncertainties. This approach naturally incorporates prior information and provides a probabilistic interpretation of both parameter values and model uncertainty. Let us explain in what follows the two Bayesian methods that we will use later.

3.2.1 Monte Carlo Markon Chain via `emcee`

To perform Bayesian inference in practice, we need to sample from the posterior distribution $P(\vec{\theta} | \vec{D})$. This is achieved using Markov Chain Monte Carlo (MCMC) methods, which generate a sequence of samples that follow the target posterior distribution. In our analysis, we use the `emcee` Python package, which implements the affine-invariant ensemble sampler developed by Goodman and Weare <https://emcee.readthedocs.io/en/stable/>.

The key idea behind MCMC is to construct a random walk through parameter space such that the density of points visited by the walk reflects the shape of the posterior. In `emcee`, this is done by initializing an ensemble of points called *walkers*. Each walker independently explores the parameter space, taking steps according to a proposal rule that ensures detailed balance and ergodicity.

Each step for a walker proposes a new position in parameter space (i.e., a new set of cosmological parameter values), which is accepted or rejected based on the Metropolis-Hastings criterion using the posterior probability [73]. Since the posterior is proportional to the product of the prior and the likelihood, the sampling process naturally incorporates prior bounds, and walkers test parameter values accordingly. Over time, the distribution of the walkers' positions approximates the true posterior.

In our case, the likelihood is assumed to follow a Gaussian distribution due to the nature of the observational uncertainties. Therefore, we use a chi-square likelihood of the form:

$$\mathcal{L}(\vec{\theta}) \propto \exp\left(-\frac{1}{2}\chi^2(\vec{\theta})\right), \quad (3.4)$$

which is equivalent to assuming independent Gaussian errors on the residuals used in the χ^2 analysis.

To ensure the chains have converged and are sampling the posterior reliably, we monitor the *auto-correlation time*, which measures how many steps are required before successive samples become effectively independent. We discard an initial *burn-in* phase, during which the walkers may still be settling into the high-probability regions of parameter space. A common choice is to run the sampler for several times the estimated auto-correlation time and discard the first few such intervals as burn-in.

While MCMC provides a robust method for parameter estimation, it does not compute the Bayesian evidence $P(\vec{D})$, which is needed for model comparison. Therefore, if model selection is required, alternative methods such as *Nested Sampling* must be used, as these are designed to estimate the evidence while also providing posterior samples, making them at the same time computationally more expensive.

3.2.2 Nested Sampling

While MCMC methods are highly effective for parameter estimation, they do not provide the Bayesian evidence $P(\vec{D})$, which is essential for model comparison. To overcome this limitation, we use *Nested Sampling* [74], a technique designed to efficiently compute both the posterior distribution and the evidence simultaneously.

The Bayesian evidence, or marginal likelihood, is defined as:

$$Z = P(\vec{D}) = \int P(\vec{D} | \vec{\theta}) P(\vec{\theta}) d\vec{\theta}, \quad (3.5)$$

where Z quantifies the average likelihood of a model over its entire prior volume. Models with higher evidence are better supported by the data, balancing goodness of fit with parameter volume.

Nested Sampling transforms this multidimensional integral into a one-dimensional integral over the prior mass. This is done by defining a series of nested likelihood contours and computing the volume between them. At each step, the algorithm maintains a set of *live points*, which are sampled uniformly within the region of parameter space where the likelihood exceeds a given threshold [75].

The process proceeds iteratively:

- Initialize N live points drawn from the prior distribution.
- At each iteration, identify the live point with the lowest likelihood and replace it with a new point drawn from the prior, but constrained to have a higher likelihood.
- This process effectively explores nested shells of increasing likelihood, shrinking the prior volume and building up the evidence integral as:

$$Z \approx \sum_i \mathcal{L}_i w_i, \quad (3.6)$$

where \mathcal{L}_i is the likelihood of the i -th discarded point and w_i is its associated prior volume weight.

As the algorithm progresses, the set of discarded points, each weighted appropriately, samples the posterior distribution. The result is a set of posterior samples along with an estimate of the evidence Z and its uncertainty.

Consistency and convergence of the algorithm are assessed through several diagnostics, including:

- **Estimated Sample Size (ESS):** This measures how many independent posterior samples have been effectively obtained. A sufficiently large ESS ensures accurate posterior statistics.

- **Log-evidence stability:** Convergence is also monitored by observing whether the change in the estimated log-evidence becomes negligible over successive iterations.

Nested Sampling, and in particular `dynesty` [76], is especially useful in cosmology where comparing competing models—such as Λ CDM without transition in M versus Λ CDM with transition in M —requires reliable estimates of both parameter constraints and model evidence. Given that our models included up to 7 parameters, the use of `dynesty` was well-suited to the task. However, this method providing posterior sampling and the evidence comes with a price of being computationally expensive. The higher the number of live points being used the better the results, but also the more expensive the calculation. Given the tools that we had available, we could not use more than 500 points for a model of maximum 5 parameters. This limited number of live points cannot provide as strict constraints on the parameters as the MCMC with 5000 steps does. However, it is more than enough to calculate the evidence of the model with a small uncertainty, as we shall prove for all of the models that we tested. *Therefore, we declare here that Nested Sampling is used only for model comparison via the evidence, which is justified given the low uncertainty found on the evidence calculation for each model.* However, we do report for each case the median values and the corresponding contour plots and compare them with the ones derived from MCMC, to ensure that the values are in agreement—but not equally powerfully statistically constrained—making usre that the model comparison is consistent.

3.3 Λ CDM Inference via χ^2 Minimization

Let us now apply the χ^2 minimization method using the PANTHEON+ dataset (available on GitHub: <https://github.com/PantheonPlusSH0ES/DataRelease>). We make use of specific columns that contain the relevant observational and calibration information. These are:

- **Hubble diagram redshift (z_{HD}):** This is the redshift used in the cosmological fit, corrected for peculiar velocities and given in the CMB rest frame. It is used as the input variable for computing theoretical distance moduli.
- **Corrected apparent magnitude (m_B):** This magnitude has been standardized using light-curve corrections (stretch and color) and bias corrections. It represents the observed brightness of each supernova after standardization.
- **Cepheid-calibrated distance modulus (μ_{Ceph}):** For supernovae hosted in galaxies with Cepheid variable stars, this column gives the distance modulus derived independently from the Cepheid calibration. It enables

a direct constraint on the absolute magnitude M of Type Ia supernovae and helps break the degeneracy between H_0 and M .

- **Cepheid host flag:** A binary flag indicating whether a given supernova is in a Cepheid-hosting galaxy. It is used to selectively apply the calibration data to the likelihood function.

These columns are used to construct the residuals \vec{Q} in the χ^2 computation, allowing for a coherent comparison between the observed and model-predicted distance moduli. The covariance matrix provided with the PANTHEON+ dataset accounts for both statistical and systematic uncertainties, and is applied consistently across all supernovae in the sample.

3.3.1 No-transition in Absolute Magnitude

We now construct the χ^2 statistic in the context of a flat Λ CDM model, following the methodology described by Perivolaropoulos and Skara (P&S) [2]. The model predicts the distance modulus $\mu_{\text{model}}(z)$ for each supernova, based on the parameters (Ω_m, H_0, M) , which for the flat Λ CDM model is given by equation (2.29)

The χ^2 function is built from the residuals between the observed apparent magnitudes and the model predictions. However, to break the degeneracy between H_0 and the absolute magnitude M , the likelihood must incorporate both Cepheid-calibrated and Hubble-flow supernovae. Following P&S, we define a modified residual vector \vec{Q} with elements:

$$Q_i = \begin{cases} m_{B,i} - M - \mu_{\text{Ceph},i} & \text{if SN } i \text{ is in a Cepheid host,} \\ m_{B,i} - M - \mu_{\text{model}}(z_i) & \text{otherwise.} \end{cases} \quad (3.7)$$

The full χ^2 is then written as:

$$\chi^2 = \vec{Q}^T C^{-1} \vec{Q},$$

where C is the covariance matrix provided with the dataset, incorporating both statistical and systematic uncertainties. This construction ensures a unified treatment of both calibrated and uncalibrated supernovae, and allows for a direct fit of the cosmological parameters (Ω_m, H_0, M) . This framework forms the basis for both frequentist inference and the likelihood function used in the Bayesian approach.

The minimization of this χ^2 yields the best-fit values of the parameters. The associated uncertainties are calculated via the diagonal of the parameter covariance matrix, *i.e.* the inverse of the Fisher matrix defined in equation (3.2).

We implemented this method using Python. We implemented a numerical optimization pipeline following [2]. The fit includes three free parameters: the absolute magnitude M of Type Ia supernovae, the Hubble parameter H_0 (in $\text{km s}^{-1} \text{Mpc}^{-1}$), and the matter density Ω_m .

Bounds and Initialization: We constrained the parameters within broad, physically motivated bounds:

- $M \in [-20, -19]$
- $H_0 \in [68, 80] \text{ km s}^{-1} \text{Mpc}^{-1}$
- $\Omega_m \in [0.0, 1.0]$

The initial guess used was $M = -19.3$, $H_0 = 70.0$, and $\Omega_m = 0.3$.

Minimization Algorithm: We employed the L-BFGS-B optimization algorithm, a quasi-Newton method that supports box constraints and is particularly well-suited for smooth, bounded optimization problems like ours. It leverages gradient information to rapidly converge and is robust against mild degeneracies often found in cosmological likelihoods. The termination criteria were chosen to ensure convergence to machine precision, with a function tolerance of 10^{-9} and gradient tolerance of 10^{-5} .

Fisher Matrix Estimation: To estimate uncertainties, we computed the Fisher matrix numerically. A small cubic grid was constructed around the best-fit parameters, and the χ^2 function was evaluated at discrete points on this grid. A quadratic surface was then fit to the χ^2 values, and the second derivatives were used to construct the Fisher matrix:

$$F_{ij} = \frac{1}{2} \frac{\partial^2 \chi^2}{\partial p_i \partial p_j}.$$

Inverting this matrix provides the parameter covariance matrix, from which the 1σ uncertainties are obtained as the square roots of the diagonal elements.

Results: The best-fit values and their uncertainties are:

$$M = -19.25 \pm 0.03 \tag{3.8}$$

$$H_0 = 73.4 \pm 1.0 \text{ km s}^{-1} \text{Mpc}^{-1} \tag{3.9}$$

$$\Omega_m = 0.333 \pm 0.018. \tag{3.10}$$

The minimum χ^2 value achieved was:

$$\chi^2_{\min} = 1522.98, \tag{3.11}$$

with a total of $n = 1701$ supernovae and $k = 3$ fitted parameters. This yields a number of degrees of freedom:

$$\text{dof} = n - k = 1698,$$

and a reduced chi-square value:

$$\chi_{\nu}^2 = \frac{\chi_{\text{min}}^2}{\text{dof}} = 0.896. \quad (3.12)$$

This reduced chi-square is less than 1 and may indicate a possible overestimation of the uncertainties in the covariance matrix as pointed out in [77]. Our results are in excellent agreement with the ones from P&S [2] and consequently also with the original PANTEHON+ results [1].

3.3.2 Transition in Absolute Magnitude

The next step in our analysis is to test the homogeneity of the PANTHEON+ dataset by allowing for a possible transition in the standardized absolute magnitude M of Type Ia supernovae at a critical distance d_{crit} . The goal is to investigate whether a statistically significant improvement in the fit can be achieved by allowing M to vary with distance, which could indicate either a real physical inhomogeneity or a residual systematic effect.

Following [2], we extend the likelihood model accordingly by introducing two distinct absolute magnitudes: $M_<$ for supernovae closer than d_{crit} and $M_>$ for those farther away. The residual vector \vec{Q} used in the χ^2 function is modified to reflect this piecewise definition:

$$Q_i = \begin{cases} m_{B,i} - M_< - \mu_{\text{Ceph},i} & \text{if } \mu_{i,S} < \mu_{\text{crit}}, i \in \text{Cepheid hosts}, \\ m_{B,i} - M_> - \mu_{\text{Ceph},i} & \text{if } \mu_{i,S} > \mu_{\text{crit}}, i \in \text{Cepheid hosts}, \\ m_{B,i} - M_< - \mu_{\text{model}}(z_i) & \text{if } \mu_{i,S} < \mu_{\text{crit}}, i \notin \text{Cepheid hosts}, \\ m_{B,i} - M_> - \mu_{\text{model}}(z_i) & \text{if } \mu_{i,S} > \mu_{\text{crit}}, i \notin \text{Cepheid hosts}, \end{cases} \quad (3.13)$$

where $\mu_{i,S} = m_{B,i} + 19.253$ and μ_{crit} corresponds to the distance modulus at the critical distance d_{crit} .

This generalization increases the number of free parameters from three to five: $M_<$, $M_>$, H_0 , Ω_m , and d_{crit} . The rest of the methodology—constructing the χ^2 statistic from the residuals and minimizing it—is carried over directly from the no-transition case.

Validation of the Methodology: Before proceeding with the transition model, we verified that our implementation of the χ^2 minimization is robust and accurate. The excellent agreement between our best-fit values and those reported in Perivolaropoulos and Skara (P&S) for the standard Λ CDM case confirms the reliability of the numerical setup, parameter bounds, and optimization procedure.

Bounds and Initialization: The initial parameter values and their allowed ranges were chosen based on physical plausibility and prior studies:

- $M_< \in [-19.45, -19.32]$
- $M_> \in [-19.30, -19.15]$
- $H_0 \in [72.0, 78.0] \text{ km s}^{-1} \text{ Mpc}^{-1}$
- $\Omega_m \in [0.20, 0.50]$
- $d_{\text{crit}} \in [18.5, 21.5] \text{ Mpc}$

The initial guess used was $M_< = -19.4$, $M_> = -19.2$, $H_0 = 74.0$, $\Omega_m = 0.3$, and $d_{\text{crit}} = 19.95$ Mpc.

Optimization Strategy: We employed the same L-BFGS-B algorithm as before, with strict tolerance settings:

- Function tolerance: 10^{-9}
- Gradient norm tolerance: 10^{-5}
- Maximum iterations: 10,000

The best-fit parameter values were extracted from the minimization output, and the Fisher matrix was again computed via a local quadratic fit to the χ^2 surface around the minimum, using a fine grid in the 5D parameter space.

Results: The best-fit values and corresponding 1σ uncertainties are:

$$M_< = -19.398 \pm 0.05 \quad (3.14)$$

$$M_> = -19.206 \pm 0.03 \quad (3.15)$$

$$H_0 = 74.8 \pm 1.0 \text{ km s}^{-1} \text{ Mpc}^{-1} \quad (3.16)$$

$$\Omega_m = 0.332 \pm 0.02 \quad (3.17)$$

$$d_{\text{crit}} = 19.95 \pm 0.1 \text{ Mpc} \quad (3.18)$$

The minimum value of the χ^2 function was:

$$\chi_{\min}^2 = 1503.38 \quad (3.19)$$

with $n = 1701$ data points and $k = 5$ free parameters, yielding:

$$\text{dof} = n - k = 1696, \quad \chi_{\nu}^2 = \frac{\chi_{\min}^2}{\text{dof}} = 0.886.$$

Our results are again in excellent agreement with [2]. It is also worth mentioning here, that another way to check the consistency of the inferred best-fit values is to check whether they lie on the edges of the bounds. One of them could be lying on the edge of its given bound and the resulted minimum would not change significantly, meaning that the reduced χ^2 would still be lower or close to 1, implying thus a good fit. If such thing happens, then one can increase the given bounds and see how this best-fit value changes. In our case, no best-fit value was lying close to the edge of its given bound.

3.3.3 AIC & BIC Tests

When comparing models with different numbers of parameters, it is essential to balance goodness of fit against model complexity to avoid overfitting. Two widely used statistical tools for this purpose are the *Akaike Information Criterion* (AIC) and the *Bayesian Information Criterion* (BIC). Both criteria penalize the likelihood based on the number of free parameters, but differ in how strongly they penalize complexity.

Akaike Information Criterion (AIC): The AIC is defined as:

$$\text{AIC} = \chi_{\min}^2 + 2k, \quad (3.20)$$

where k is the number of free parameters. The AIC favors models that achieve a lower χ^2 while penalizing the addition of extra parameters linearly [78].

Bayesian Information Criterion (BIC): The BIC is given by:

$$\text{BIC} = \chi_{\min}^2 + k \ln(n), \quad (3.21)$$

where n is the number of data points. Unlike AIC, the BIC penalizes complexity more strongly, especially for large datasets, as the penalty term scales with $\ln(n)$ [79].

Interpretation Guidelines: The relative support for one model over another can be assessed by computing the differences ΔAIC and ΔBIC between models. The interpretation is generally as follows:

$\Delta\text{AIC} = \text{AIC}_{\text{transition}} - \text{AIC}_{\text{no-transition}}$	Interpretation
< -10	Strong preference for transition model
$[-10, -5]$	Moderate preference for transition model
$[-5, -2]$	Weak preference for transition model
$[-2, 2]$	Models are statistically indistinguishable
$(2, 5]$	Weak preference for no-transition model
$(5, 10]$	Moderate preference for no-transition model
> 10	Strong preference for no-transition model

Table 1: Interpretation guide for AIC differences.

$\Delta\text{BIC} = \text{BIC}_{\text{transition}} - \text{BIC}_{\text{no-transition}}$	Interpretation
< -10	Strong preference for transition model
$[-10, -6)$	Moderate preference for transition model
$[-6, -2)$	Weak preference for transition model
$[-2, 2]$	Models are statistically indistinguishable
$(2, 6]$	Weak preference for no-transition model
$(6, 10]$	Moderate preference for no-transition model
> 10	Strong preference for no-transition model

Table 2: Interpretation guide for BIC differences.

Application to Our Models: We computed the AIC and BIC for both models as follows:

- No-transition model: $\chi^2_{\min} = 1522.98, k = 3$
- Transition model: $\chi^2_{\min} = 1503.38, k = 5$
- Number of data points: $n = 1701$

$$\begin{aligned} \text{AIC (No-Transition)} &= 1522.98 + 2 \times 3 = 1528.98 \\ \text{AIC (Transition)} &= 1503.38 + 2 \times 5 = 1513.38 \\ \Delta\text{AIC} &= 1513.38 - 1528.98 = -15.60 \end{aligned} \tag{3.22}$$

$$\begin{aligned} \text{BIC (No-Transition)} &= 1522.98 + 3 \ln(1701) \approx 1522.98 + 21.66 = 1544.64 \\ \text{BIC (Transition)} &= 1503.38 + 5 \ln(1701) \approx 1503.38 + 36.10 = 1539.48 \\ \Delta\text{BIC} &= 1539.48 - 1544.64 = -5.16 \end{aligned} \tag{3.23}$$

Interpretation: Based on Tables 1 & 2 we see that:

- $\Delta\text{AIC} = -15.6$ indicates **strong preference for the transition model**.
- $\Delta\text{BIC} = -5.16$ indicates **moderate preference for the transition model**.

There is substantial evidence in favor of the transition model. The AIC difference ($\Delta\text{AIC} = -15.6$) indicates **strong support**, while the BIC difference ($\Delta\text{BIC} = -5.16$) indicates **moderate support**. Since the BIC penalizes model complexity more heavily—particularly in large datasets like PANTHEON+—it is more conservative by design. The fact that both criteria favor the same model, even if with different strengths, suggests that the improvement in fit is statistically meaningful and not merely a result of overfitting. Thus, the transition model is preferred on empirical and statistical grounds.

Frequentist Confidence Contours: To assess the uncertainty in the cosmological parameter estimates, we construct frequentist confidence contours based on a grid evaluation of the χ^2 function around the best-fit point. First, we define the offset

$$\Delta\chi^2(\vec{p}) = \chi^2(\vec{p}) - \chi_{\min}^2, \quad (3.24)$$

where χ_{\min}^2 is the global minimum obtained from the L-BFGS-B minimization, and \vec{p} is a 2D slice of the parameter space (e.g., (Ω_m, M) or (H_0, M)). During this procedure, all nuisance parameters not shown in the slice are held fixed at their best-fit values.

The confidence levels corresponding to 1σ , 2σ , and 3σ regions are then defined by threshold values of $\Delta\chi^2$, derived from the inverse incomplete gamma function [80]:

$$\Delta\chi_{\sigma}^2 = 2\Gamma^{-1}\left(\frac{\nu}{2}, p\right), \quad (3.25)$$

where ν is the number of parameters shown in the slice (typically $\nu = 2$), and p is the desired confidence level (68.3%, 95.5%, or 99.7% for 1σ , 2σ , and 3σ , respectively). This yields the appropriate contour levels for comparing both the no-transition ($k = 3$ parameters) and transition ($k = 5$ parameters) models.

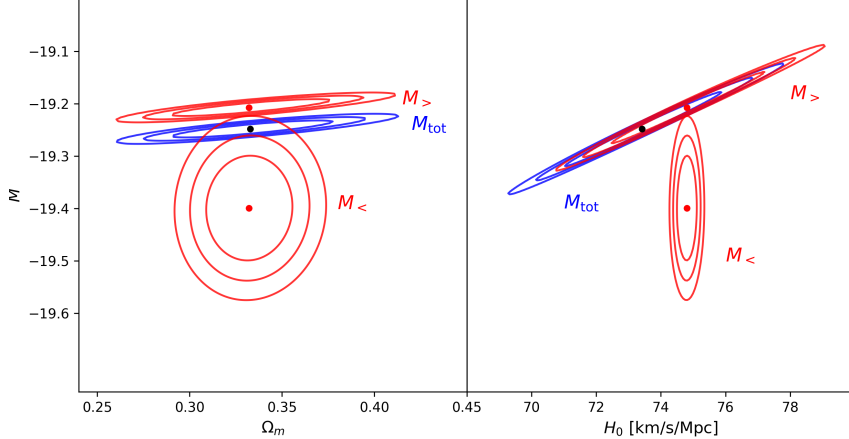


Figure 2: Frequentist contour plots for the Λ CDM model with and without a transition in M . The left panel shows M vs. Ω_m , and the right panel shows M vs. H_0 . Contours correspond to 1σ , 2σ , and 3σ confidence levels.

The contours shown in Figure 2 visualize how χ^2 increases away from the minimum, forming elliptical confidence regions. These curves mark the boundaries inside which the fit remains statistically consistent with the data, given a chosen confidence level.

In the frequentist interpretation, the 1σ region has a well-defined meaning: assuming the model is correct, then under repeated independent realizations of the data, the true parameter values would fall inside this region approximately 68.3% of the time. Similar interpretations hold for the 2σ and 3σ levels, encompassing 95.5% and 99.7% of realizations, respectively.

3.3.4 Accounting for the Volumetric Redshift Scatter Bias

An important systematic that can mimic an inhomogeneity in the Pantheon+ sample is the *volumetric redshift scatter bias* [1, 81]. This bias arises from peculiar velocity variations that affect nearby supernovae at redshifts $z < 0.01$. Specifically, for a fixed observed redshift, a galaxy is more likely to be scattered into the redshift bin from a larger distance (due to the larger comoving volume) than from a smaller one. This asymmetry leads to a net shift in the inferred distances of low- z objects, biasing their distance moduli μ to artificially high values. As a result, these nearby supernovae appear more luminous (lower inferred M) than they truly are, introducing a spurious signal that can be misinterpreted as a physical transition in supernova absolute magnitude.

To account for the volumetric redshift scatter bias, we eliminate SNe at $z < 0.01$ alongside with potentially useful information. The new updated likelihood now is given by:

$$Q_i = \begin{cases} m_{B,i} - M_< - \mu_{\text{Ceph},i} & \text{if } \mu_{i,S} < \mu_{\text{crit}}, i \in \text{Cepheid hosts}, \\ m_{B,i} - M_> - \mu_{\text{Ceph},i} & \text{if } \mu_{i,S} > \mu_{\text{crit}}, i \in \text{Cepheid hosts}, \\ 0 & \text{if } z_i < 0.01, \\ m_{B,i} - M_< - \mu_{\text{model}}(z_i) & \text{if } z_i \geq 0.01, \mu_{i,S} < \mu_{\text{crit}}, i \notin \text{Cepheid hosts}, \\ m_{B,i} - M_> - \mu_{\text{model}}(z_i) & \text{if } z_i \geq 0.01, \mu_{i,S} > \mu_{\text{crit}}, i \notin \text{Cepheid hosts}, \end{cases} \quad (3.26)$$

By setting $Q_i = 0$ if $z < 0.01$, we ensure that the full covariance matrix is being used in the minimization, making sure that all systematics and correlations are taken into account leading to a consistent result. Minimizing the χ^2 using the same setup like we did for the full dataset yields:

$$M_< = -19.347 \pm 0.05, \quad (3.27)$$

$$M_> = -19.226 \pm 0.03, \quad (3.28)$$

$$H_0 = 74.5 \pm 1.0 \text{ km s}^{-1} \text{ Mpc}^{-1}, \quad (3.29)$$

$$\Omega_m = 0.33 \pm 0.02, \quad (3.30)$$

$$d_{\text{crit}} = 19.95 \pm 0.1 \text{ Mpc}. \quad (3.31)$$

The minimum chi-square value obtained with this modified likelihood is:

$$\chi^2_{\min} = 1445.59 \quad (3.32)$$

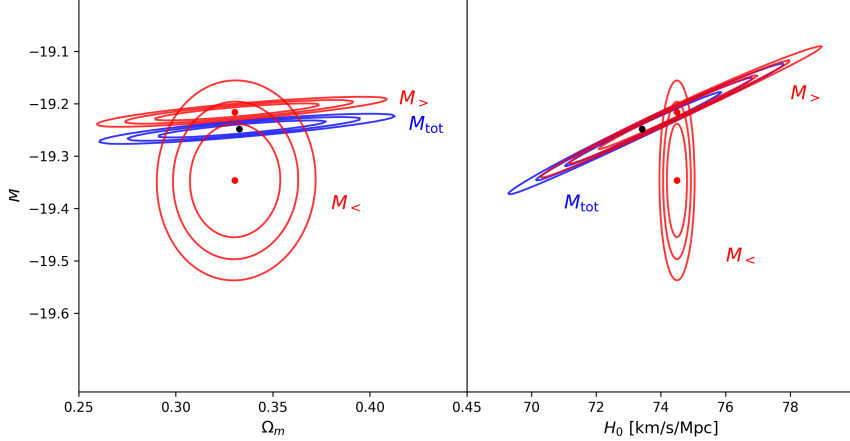


Figure 3: Frequentist likelihood contours after removing all supernovae with $z < 0.01$, to mitigate the volumetric redshift scatter bias. Compared to the full dataset, the tension between $M_<$ and $M_>$ is reduced from 3σ to slightly under 2σ , while the best-fit transition distance remains near $d_{\text{crit}} \approx 20$ Mpc.

The updated analysis using the modified likelihood of Eq. (3.9), which nullifies residuals for $z_i < 0.01$ to mitigate the volumetric redshift scatter bias, results in a best-fit transition distance near $d_{\text{crit}} \approx 20$ Mpc and a remaining discrepancy between the magnitudes $M_<$ and $M_>$ at approximately the 3σ level. While this tension is reduced compared to the full dataset, it remains statistically significant.

The AIC decreases by $\Delta\text{AIC} = -3.5$ when introducing two additional parameters relative to the no-transition model with $z < 0.01$ points removed. This AIC difference, though not large enough to constitute strong evidence, falls within the range $2 < |\Delta\text{AIC}| < 6$ (see Table 1) and is interpreted as *mild evidence* in favor of the transition model, even after excluding the potentially biased low-redshift supernovae.

These results support that the observed discrepancy between $M_<$ and $M_>$ is driven both by the volumetric redshift scatter bias and by mild but persistent indications of a genuine transition in the intrinsic luminosity of Type Ia supernovae near $d \approx 20$ Mpc. The robustness of the transition signature, despite the conservative redshift cut, suggests that the phenomenon cannot be fully explained by low-redshift systematics alone.

3.4 Λ CDM Inference via MCMC & Nested Sampling

3.4.1 No-transition in M — MCMC

We begin our Bayesian parameter inference with the standard flat Λ CDM model without a transition in the supernova absolute magnitude. The goal is to constrain the cosmological parameters:

$$\vec{\theta} = (M, H_0, \Omega_m),$$

using the posterior distribution derived from Bayes' theorem:

$$P(\vec{\theta} | \vec{D}) \propto \mathcal{L}(\vec{D} | \vec{\theta}) \pi(\vec{\theta}), \quad (3.33)$$

where $\mathcal{L} \propto \exp(-\chi^2/2)$ is the likelihood and $\pi(\vec{\theta})$ denotes the prior.

The likelihood is computed using the same χ^2 function defined earlier (3.7), which compares the theoretical distance moduli with the observed ones using the full covariance matrix of the Pantheon+ dataset. We assume uniform (flat) priors within the following bounds:

$$M \in [-20, -18], \quad (3.34)$$

$$H_0 \in [65, 78] \text{ km s}^{-1} \text{ Mpc}^{-1}, \quad (3.35)$$

$$\Omega_m \in [0.1, 0.8]. \quad (3.36)$$

We use the affine-invariant ensemble sampler implemented in the `emcee` Python package. The sampler is initialized with **32 walkers**, each running for **5,000 steps**, with the first 1,000 steps discarded as burn-in. Convergence is verified via inspection of the autocorrelation time and visual stability of the chains. We get the following results for the parameters:

Parameter	MAP Value	Median	Mean	$\pm 1\sigma$	Unit
M	-19.2488	-19.2485	-19.2486	± 0.0290	
H_0	73.4036	73.3994	73.4053	± 0.9909	km/s/Mpc
Ω_m	0.3323	0.3330	0.3334	± 0.0181	

Table 3: Posterior summary statistics for the parameters M , H_0 , and Ω_m .

Let us explain what each value represents:

- **MAP (Maximum A Posteriori):** The point in parameter space that has the highest posterior probability. It is the most probable single estimate according to the posterior distribution.
- **Median:** The value that divides the posterior distribution in half. It is less sensitive to asymmetries or long tails in the distribution.

- **Mean:** The average value across all posterior samples. It takes into account the entire shape of the posterior, including the tails.

We see that the MAP values reported in Table 3 are in agreement with the best-fit values from the χ^2 minimization (3.8)–(3.10).

In this case, the MAP, mean, and median are all extremely close for each parameter. This indicates that the posterior distributions are nearly symmetric and unimodal, with very little skew or multimodality. It also confirms that the sampling procedure was stable and effective. This can also be verified by checking the auto-correlation time and the number of the resulted effective samples. We estimated the autocorrelation times for the MCMC chains and obtained values of approximately 31.7, 38.4, and 42.1 for the parameters M , H_0 , and Ω_m , respectively. These autocorrelation times correspond to effective sample sizes of roughly 5050, 4170, and 3800 for the same parameters. These results indicate that the chains are well-mixed (see Figure 4 and that the inference is based on a large number of effectively independent samples.

To visualize the joint and marginal posterior distributions of the parameters, we present the corner plot shown in Figure 5. Each diagonal panel displays the one-dimensional marginalized posterior for a single parameter, while the off-diagonal panels show the two-dimensional projections of the joint posterior distributions, with 1σ , 2σ and 3σ credible regions overlaid.

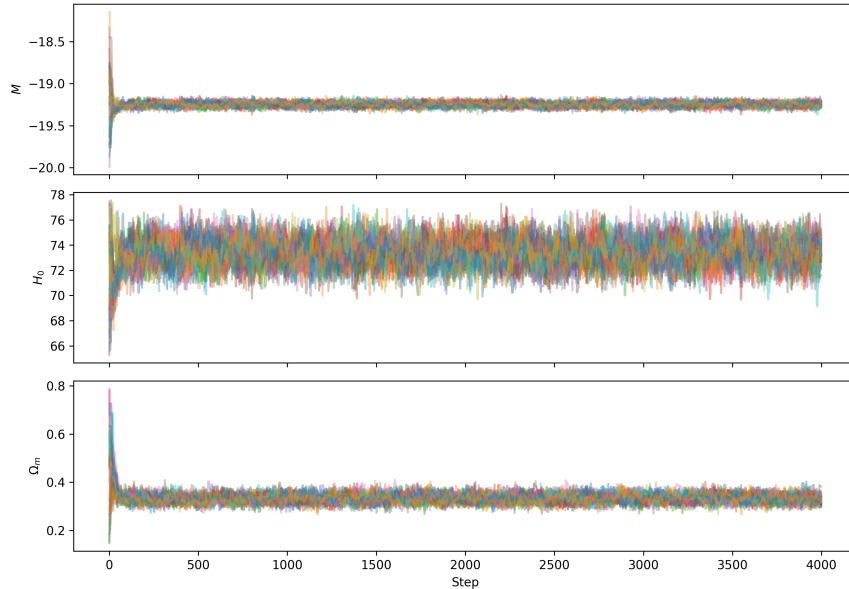


Figure 4: MCMC trace plots for the no-transition model. Walkers exhibit good mixing and convergence after the burn-in phase.

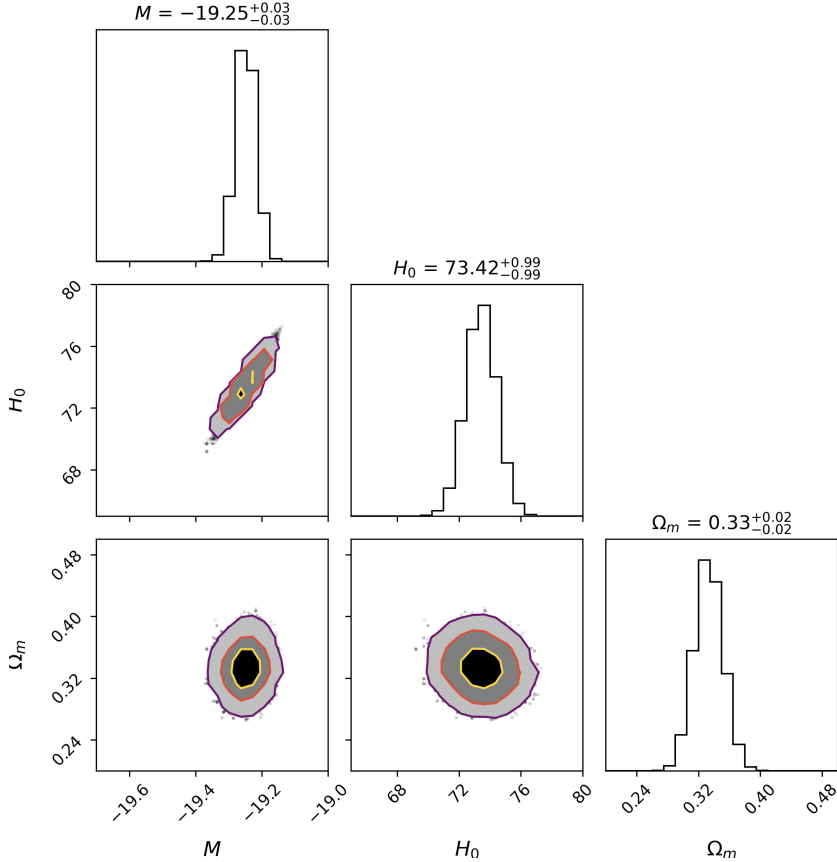


Figure 5: Corner plot showing the posterior distributions and contours for the no-transition flat Λ CDM model. The contours indicate 1σ , 2σ and 3σ credible regions. The median values are given on top of each of the 1-D posteriors.

In the Bayesian framework, the 1σ credible region corresponds to the highest-density interval (or area) that contains 68% of the total posterior probability. This means that, assuming the model is correct, there is a 68% probability that the true parameter values lie within this region. The contours are not interpreted in terms of repeated sampling—as in the frequentist case—but rather reflect our degree of belief about where the parameters are likely to be, given the observed data and prior assumptions.

3.4.2 Transition in M — MCMC

Now that we have already setup the table, having defined the χ^2 functions for both transition and no-transition and having setup the emcee sampler, the transition from the no-transition to the transition case is straightforward.

We have to update our priors, since now we have two extra parameters, and subsequently the χ^2 likelihood and the posterior. We assume uniform priors within the following bounds:

$$M_< \in [-20, -18], \quad (3.37)$$

$$M_> \in [-20, -18], \quad (3.38)$$

$$H_0 \in [60, 80] \text{ km s}^{-1} \text{ Mpc}^{-1}, \quad (3.39)$$

$$\Omega_m \in [0.1, 0.5], \quad (3.40)$$

$$d_{\text{crit}} \in [15, 25] \quad (3.41)$$

The likelihood function is modified accordingly, now using the residual vector defined in (3.13). We adopt the same sampling strategy as in the no-transition case: an ensemble of 32 walkers is evolved for 5000 steps, with the first 1000 steps discarded as burn-in. This process yields the following results:

Parameter	MAP Value	Median	Mean	$\pm 1\sigma$	Unit
M_{low}	-19.40164	-19.40307	-19.40379	± 0.05563	
M_{high}	-19.20362	-19.21293	-19.21262	± 0.03077	
H_0	74.94160	74.59914	74.62226	± 1.07789	km/s/Mpc
Ω_m	0.33267	0.33251	0.33259	± 0.01795	
d_{crit}	19.94380	19.48852	19.65654	± 0.81095	Mpc

Table 4: Posterior summary statistics for the parameters in the transition model.

where we see that the MAP values are in agreement with the best-fit values from the χ^2 minimization presented in (3.14)–(3.18), indicating a clear step between the absolute magnitudes M_{low} and M_{high} , with their difference being well-resolved given the reported uncertainties.

The posterior distributions for the five parameters in the transition model exhibit different statistical behaviors, as reflected in the values of their MAP estimates, medians, and means. For parameters such as $M_<$, $M_>$, and Ω_m , the MAP, median, and mean values are nearly identical. This close agreement indicates that the posterior distributions for these parameters are approximately symmetric and unimodal, with negligible skewness. As a result, any of these central estimates provides a consistent summary of the posterior.

In contrast, for H_0 and d_{crit} , we observe more noticeable differences between the MAP, median, and mean values. Specifically, the MAP value of $H_0 = 74.94 \text{ km s}^{-1} \text{ Mpc}^{-1}$ lies above both the median (74.60) and the mean (74.62), and the difference is even more pronounced in the case of d_{crit} , where the MAP estimate (19.94 Mpc) is significantly higher than the median (19.49 Mpc) and mean (19.66 Mpc). Let us interpret these discrepancies. The first thing to do,

is to make sure that our sampler converged properly, by checking if the chain has properly converged. Looking at the chain plot 6, we can verify successful convergence.

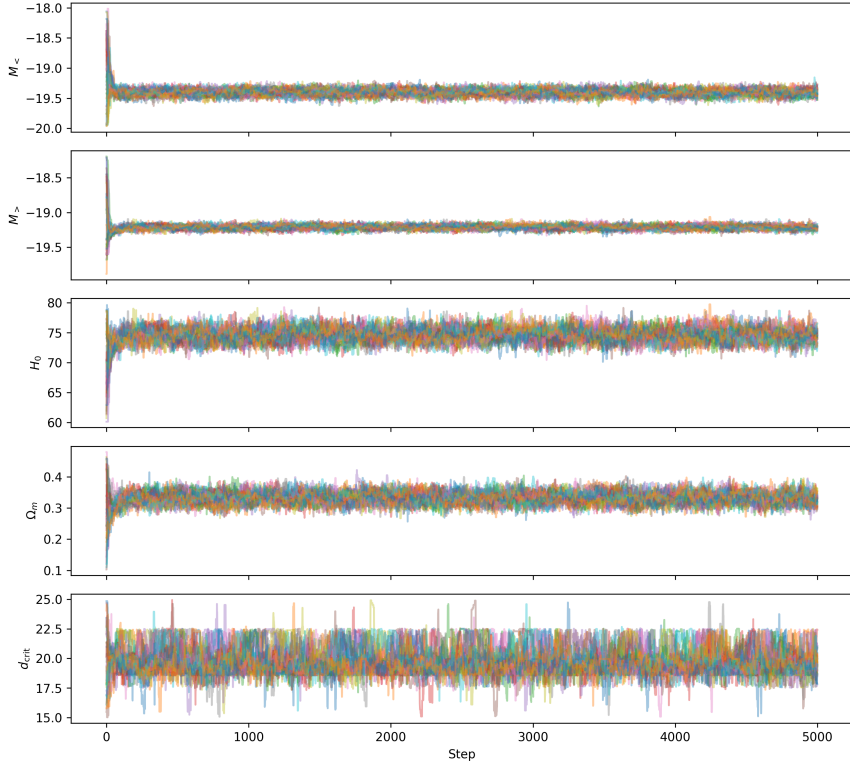


Figure 6: MCMC trace plots for the transition model. Walkers exhibit good mixing and convergence after the burn-in phase.

Since the sampler has successfully converged, let us see what is the source of these discrepancies. The differences in the H_0 values are suggesting a posterior distribution that is slightly skewed toward lower values. This asymmetry may be due to the interplay between H_0 and other parameters in the model, particularly the degeneracy with $M_<$ and $M_>$. In the case of d_{crit} , the sharp differences indicate a right-skewed posterior distribution, potentially arising from a flattening of the likelihood surface or limited data sensitivity in that region of parameter space. Such skewness is common in parameters that define thresholds or transition scales, especially when the data do not sharply constrain their exact location. More insight can be provided via the corner plot 7. We see that the H_0 - $M_<$ and H_0 - $M_>$ joint distributions exhibit tilted and elongated contours. These indicate strong or mild degeneracies between H_0 and the supernova absolute magnitudes, which skew the posterior density along their shared

parameter directions. As a result, the peak of the H_0 marginal lies at higher values than its center of mass, producing a MAP that exceeds both the mean and median. We can double check this, by calculating the correlation matrix of the posterior samples and by plotting the 1-D profile likelihood of H_0 .

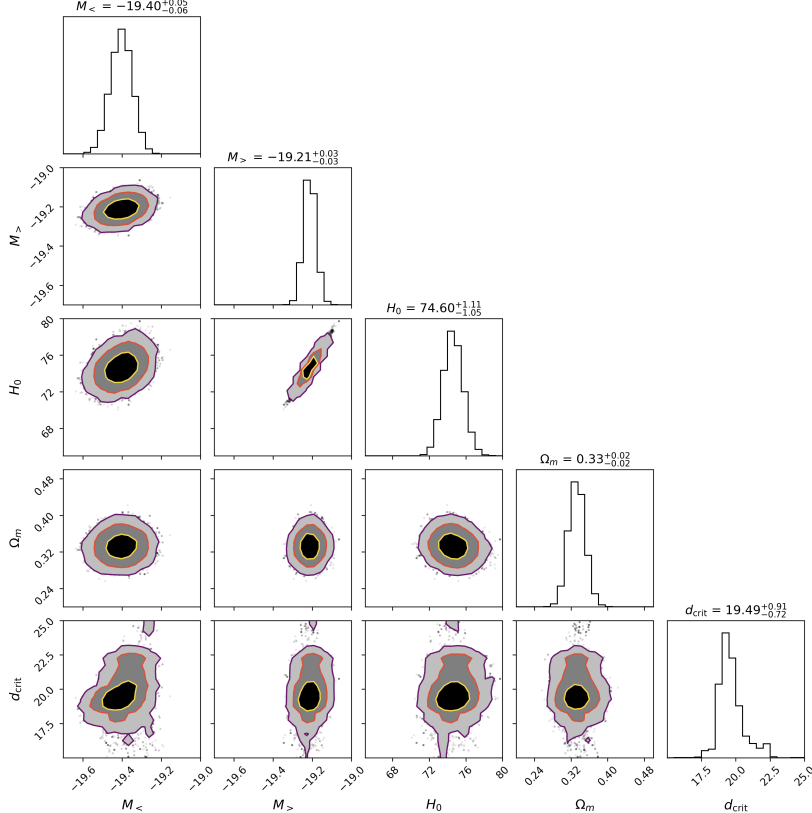


Figure 7: Corner plot showing the posterior distributions and contours for the transition flat Λ CDM model. The contours indicate 1σ , 2σ and 3σ credible regions. The median values are given on top of each of the 1-D posteriors.

From the correlation matrix 8, we see that H_0 shows an extremely strong positive correlation with $M_>$ ($\rho = 0.976$), indicating a near-linear degeneracy. This explains why the posterior distribution of H_0 is skewed: while its maximum a posteriori (MAP) value lies at the ridge's peak, the median and mean are drawn back along the degeneracy direction. A moderate correlation with $M_<$ ($\rho = 0.319$) further contributes to this structure.

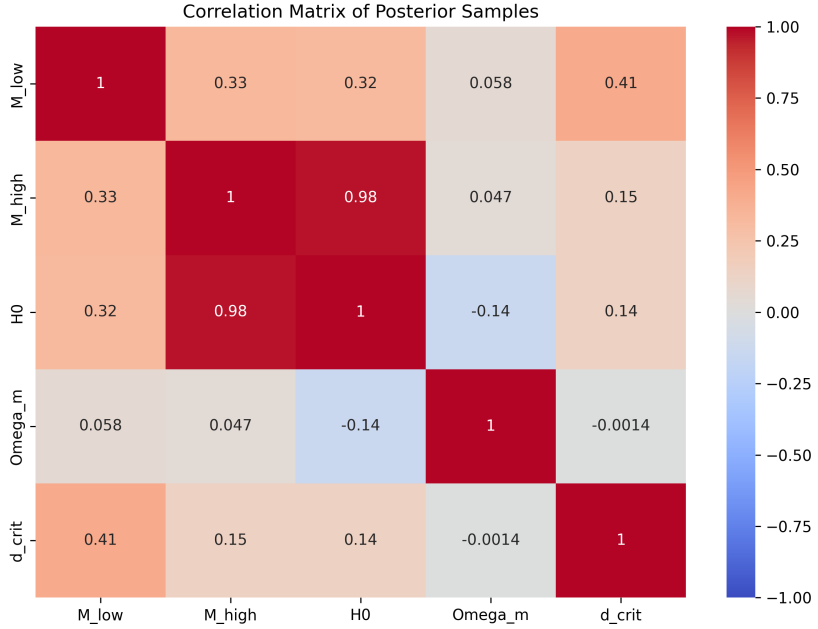


Figure 8: Correlation matrix of flattened MCMC samples for the transition case. Values close to $+1$ demonstrate strong correlation and values close to -1 demonstrate strong anti-correlation.

We can further check the profile likelihood of H_0 . To do that, we will fix all the nuisance parameters and vary H_0 in a given grid and see how the χ^2 changes¹. We see from the figure 9 that the 1D profile likelihood of H_0 reveals a smooth, nearly parabolic shape around the minimum. This indicates that the likelihood surface is well-behaved and strongly peaked, without flat directions or multimodal structure in the H_0 dimension. However, a subtle asymmetry is present: the curve descends slightly more steeply for lower H_0 values than for higher ones. The MAP value of H_0 lies to the right of both the median and the mean, consistent with the mild skewness observed in the marginal posterior. Because the likelihood profile itself is nearly symmetric, this skewness conclusively arises from parameter correlations — particularly the strong degeneracy between H_0 and $M_>$. Thus, the posterior asymmetry for H_0 is not due to the shape of the likelihood along H_0 alone, but rather due to its interaction with other parameters in the joint posterior.

¹This is not exactly how profile likelihood works. In principle, one should vary H_0 and for every value in the grid, minimize the χ^2 , instead of just fixing the nuisance parameters. However, fixing the nuisance parameters serves our goal well, given that we're only interested in the shape and a full profile likelihood calculation can be very computationally expensive.

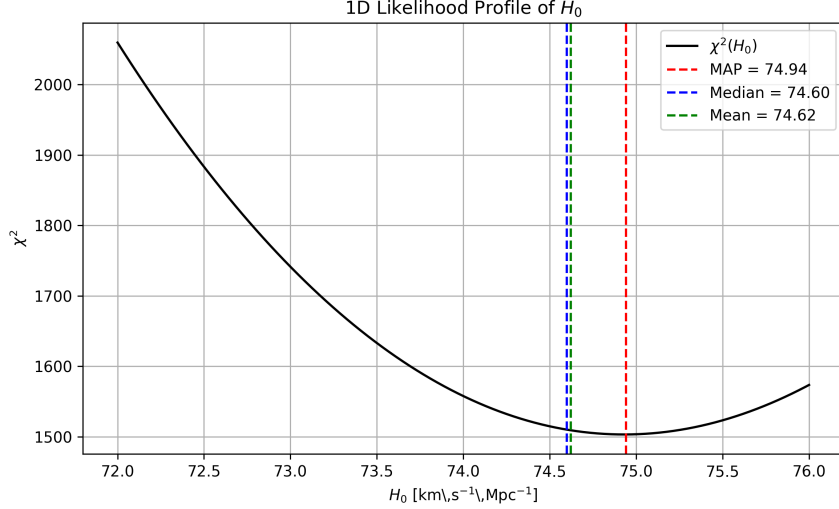


Figure 9: The 1-D Likelihood profile of H_0 .

In contrast with H_0 , d_{crit} exhibits only weak correlations with all other parameters as seen from figure 8, with its largest being a modest correlation with $M_<$ ($\rho = 0.407$). This supports the conclusion that the skewness in the d_{crit} posterior is not primarily due to parameter degeneracies, but rather reflects a broad, flat likelihood region along the transition scale. This implication is strongly verified by its 1-D profile likelihood shown in Figure 10, which instead of a smooth parabola, the curve features a relatively flat minimum and several discontinuous steps, particularly in the range $18.8 \text{--} 20.0$ Mpc. This flatness reflects the nature of d_{crit} as a threshold parameter that determines a regime split in the model: small shifts in its value do not strongly affect the fit, leading to a region of nearly equivalent likelihood. The sharp dip at $d_{\text{crit}} = 19.94$ Mpc corresponds to the MAP value, but the posterior mean and median are shifted toward smaller values (19.66 and 19.49 Mpc, respectively). This confirms that the skewness in the posterior distribution of d_{crit} is primarily due to structural uncertainty rather than degeneracy.

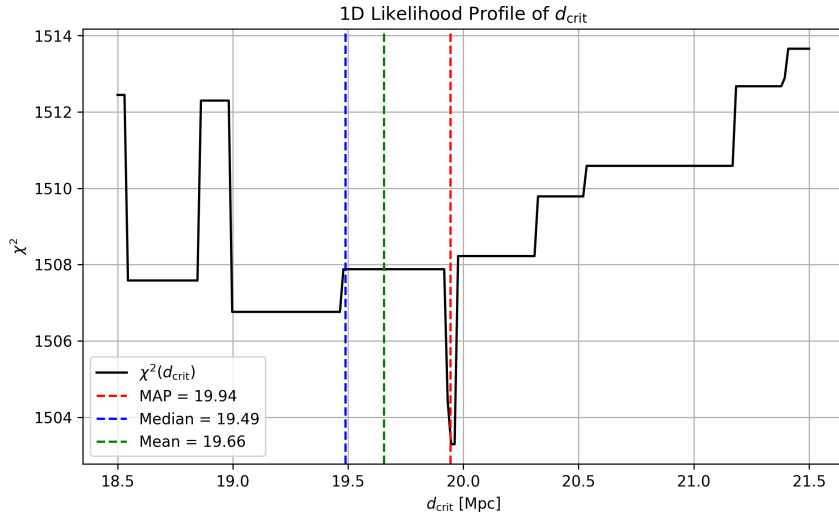


Figure 10: The 1-D Likelihood profile of d_{crit} .

Meanwhile, Ω_m shows negligible correlations with any other parameter, confirming its constraints arise independently. These quantitative results reinforce the importance of interpreting Bayesian posteriors in both marginal and joint dimensions. While the MAP reflects the single most probable parameter set, the median and mean provide complementary views of the full posterior structure, especially in cases of asymmetric or degenerate distributions.

3.4.3 No-Transition in M — Nested Sampling/dynesty

MCMC verified the χ^2 minimization results, however, model comparison is not possible via MCMC, which is why we shift to the Nested Sampling method. This method provides us with the posterior samples and the evidence as well. It is a strong but also computationally expensive method. Given the tools that we had available, we could not run a `dynesty` sampler for more than 500 live points. As a result, the contour plots are expected to not look as smooth as the ones from MCMC and a slight mismatch is expected in the transition model, where two more parameters are included, making the model more complex. However, even less than 500 live points are more than enough to compute the evidence and compare models, as long as consistency is applied, *i.e.* the same number of live points was used for the two models being compared. Let us highlight here that using this method was solely motivated by our desire to compare models, therefore, we won't spend time on explaining the contour plots and the possible differences between the MAP, median and mean values, as we did in the MCMC case.

We're interested in a flat Λ CDM model. Nested sampling algorithms such as `dynesty` operate by drawing samples from the unit cube, where each parameter is initially assumed to be uniformly distributed in the interval $[0, 1]$. A key step in the procedure is the application of a *prior transform*, which maps these unit-cube coordinates to the physical parameter space defined by the user's prior beliefs.

For the no-transition model, we define uniform priors over physically meaningful intervals:

$$\begin{aligned} M &\in [-20.0, -18.0], \\ H_0 &\in [65.0, 78.0] \text{ km s}^{-1} \text{ Mpc}^{-1}, \\ \Omega_m &\in [0.1, 0.8]. \end{aligned}$$

The prior transform is a deterministic function that rescales the unit-cube variables $u_i \in [0, 1]$ into these prior ranges. For example, the transformation for the Hubble constant is given by:

$$H_0 = H_{0,\min} + u_1 \cdot (H_{0,\max} - H_{0,\min}),$$

The sampler is initialized using two core components:

- The *log-likelihood function*, which returns $\log \mathcal{L} = -\chi^2/2$, computed from the residual vector Q as described earlier;
- The *prior transform*, which maps samples from the unit cube $[0, 1]^3$ into the physical parameter space defined by uniform priors on M , H_0 , and Ω_m .

We configure the sampler using 500 live points, the `rwalk` sampling algorithm (a random-walk-based proposal), and the `multi` bounding method to enclose the live point cloud efficiently. Parallel execution is enabled using a multiprocessing pool to speed up the calculation.

The run terminated after 5368 iterations, during which 106,973 likelihood evaluations were performed. The reported sampling efficiency was 5.5%, which is typical for moderately dimensional problems and indicates well-behaved exploration of the parameter space.

Convergence was assessed using the `dynesty` internal stopping criterion based on the remaining evidence contribution, `dlogz`. The final value, $\Delta \log Z = 0.001$, is well below the target threshold of 0.5, confirming statistical convergence of the nested integral. These diagnostics collectively indicate that the sampler converged properly.

Once the nested sampling run for the no-transition Λ CDM model is complete, the algorithm returns a structured output containing all the necessary results. This includes posterior samples, statistical weights for each sample, and an estimate of the Bayesian evidence. We're only interested in the latter, which quantifies the total probability of the data given the model, averaged over the entire prior volume. The natural logarithm of the evidence, denoted $\log \mathcal{Z}$, is reported along with an estimate of its uncertainty. This quantity serves as the key metric for Bayesian model comparison, allowing us to assess how well each model explains the data while penalizing for model complexity. For the flat Λ CDM model we found:

$$\log Z = -771.45 \pm 0.14 \quad (3.42)$$

where the low uncertainty further supports the reliability of the evidence. The contour plots and the mean values with their 1σ uncertainty are shown in figure 11, where we see that the `dynesty` sampler, even with 500 points provides results in good agreement with MCMC. This is because the model under consideration contained only 3 parameters and was a simple one. A discrepancy between the contour plots is expected for more complex models.

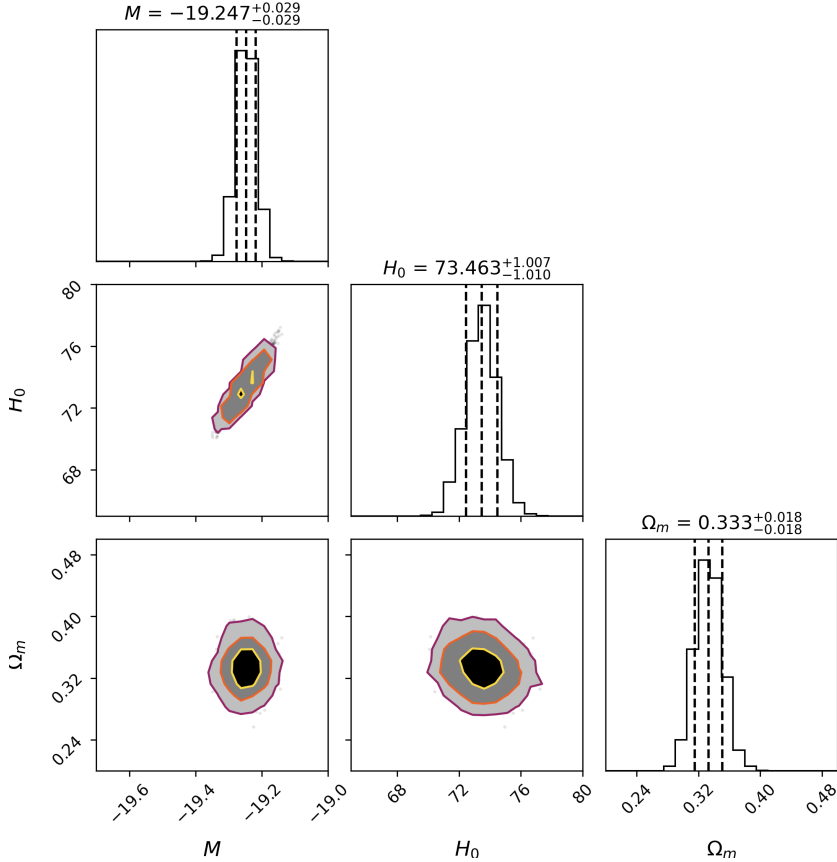


Figure 11: Corner plot for the no-transition Λ CDM model inferred by the dynesty sampler. The medians and their 1σ uncertainties are shown on top of each of the 1-D posterior distributions

3.4.4 Transition in M — Nested Sampling/dynesty

We keep the exact same structure as in the no-transition case. We only need to update the priors as:

$$M_{<} \in [-20, -18], \quad (3.43)$$

$$M_{<} \in [-20, -18], \quad (3.44)$$

$$H_0 \in [65, 78] \text{ km s}^{-1} \text{ Mpc}^{-1}, \quad (3.45)$$

$$\Omega_m \in [0.1, 0.8], \quad (3.46)$$

$$d_{crit} \in [15, 25] \quad (3.47)$$

and the χ^2 now is given by (3.13). The sampler is set up exactly as in the no-transition case, with 500 live points and a random walk. The nested sampling

run for the transition model converged successfully. The final evidence estimate stabilized at:

$$\log \mathcal{Z} = -767.49 \pm 0.18 \quad (3.48)$$

with the stopping criterion $\Delta \log \mathcal{Z} < 0.001$ satisfied. The effective sample efficiency was approximately 4.5%, and the total number of likelihood evaluations exceeded 190,000, indicating thorough exploration of the posterior and reliable integration of the evidence.

In Bayesian model selection, the relative support for two competing models \mathcal{M}_1 and \mathcal{M}_2 is quantified by the *Bayes factor*, defined as the ratio of their marginal likelihoods (evidences):

$$\mathcal{B}_{12} = \frac{\mathcal{Z}_1}{\mathcal{Z}_2}, \quad (3.49)$$

where \mathcal{Z}_i denotes the evidence for model \mathcal{M}_i . The Bayes factor measures how much more the data support one model over the other, automatically incorporating both fit quality and model complexity. In practice, it is common to work with the logarithm of the Bayes factor:

$$\Delta \log \mathcal{Z} = \log \mathcal{Z}_1 - \log \mathcal{Z}_2 \quad (3.50)$$

The strength of evidence is interpreted according to the Jeffreys scale, shown in Table 5.

$\Delta \log \mathcal{Z}$	Interpretation
< 1	Inconclusive evidence
1 to 2.5	Weak evidence for Model 1
2.5 to 5	Moderate evidence for Model 1
> 5	Strong evidence for Model 1

Table 5: Interpretation of Bayes factors according to the Jeffreys scale.

Using the Bayesian evidence computed via nested sampling, we compare the two competing models: the standard no-transition flat Λ CDM model and the extended transition model. Comparing (3.42) and (3.48) results in a Bayes factor:

$$\Delta \log \mathcal{Z} = \log \mathcal{Z}_{\text{transition}} - \log \mathcal{Z}_{\text{no-transition}} = 3.96 \quad (3.51)$$

According to the Jeffreys scale (Table 5), this level of evidence falls within the range $2.5 < \Delta \log \mathcal{Z} < 5$, corresponding to *moderate evidence* in favor of the transition model. This suggests that the inclusion of a magnitude transition yields a statistically meaningful improvement in the model's explanatory power, even after accounting for the increased parameter space, which is in agreement with our findings in section 3.3.3. The corner plot for the transition and the associated mean values with their 1σ uncertainties are shown in Figure 12.

This plot exhibits the same behavior as the corresponding MCMC one, with the ellipses being slightly more skewed as expected given the complexity of the transition model compared to the no-transition one.

In addition comparing the median values reported in the corner plots from MCMC and Nested Sampling in Figures 5, 7, 11, 12, demonstrate full agreement, providing this way solid evidence that the model comparison is consistent.

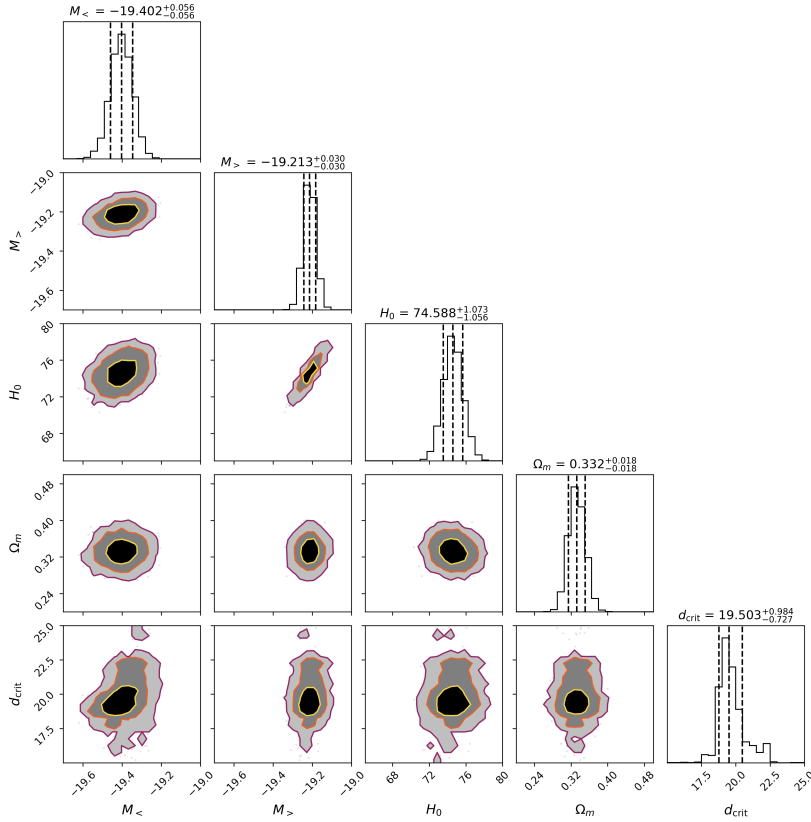


Figure 12: Corner plot for the transition Λ CDM model inferred by the dynesty sampler. The means and their 1σ uncertainties are shown on top of each of the 1-D posterior distributions

3.5 Frequentist vs Bayesian for the flat Λ CDM

Now that we inferred the flat Λ CDM model using three different methods we can safely say that a transition in the SnIa intrinsic magnitude at a distance of approximately 20 Mpc, *i.e.* late-times, is favored by the PANTHEON+ dataset in the context of this model. We saw that the methods agree on their best-fit values and we now want to check the contour plots. Let us isolate the H_0 vs M & Ω_m vs M panels (where M here means $(M, M_<, M_>)$) from the corner plots 5 & 7. The resulted plot is shown in figure 13. The observed higher degree of overlap in the MCMC-based

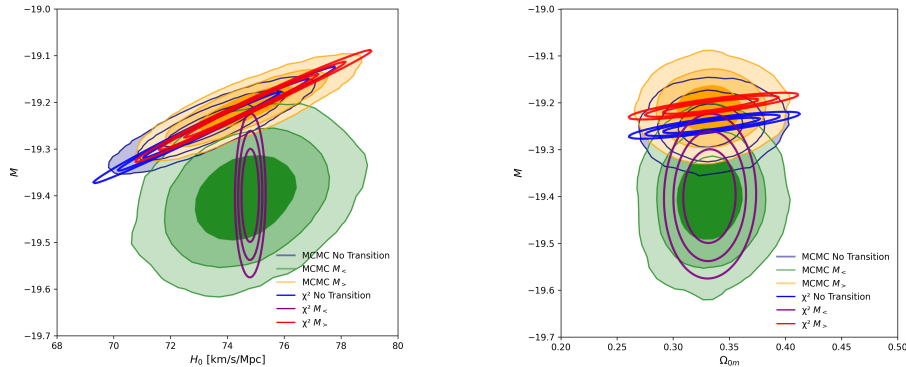


Figure 13: Overlay of H_0 vs M and Ω_m vs M , where $M = (M, M_<, M_>)$ including transition and no-transition values, derived from a standard χ^2 minimization and MCMC sampling via emcee.

(Bayesian) contour plots, compared to those derived from χ^2 minimization (frequentist approach), arises from fundamental differences in how these frameworks handle uncertainty and parameter marginalization [82].

In Bayesian inference, the posterior distributions for parameters such as H_0 , Ω_m , and M are obtained by *marginalizing* over all other parameters in the model, including nuisance parameters like $M_<$, $M_>$, and d_{crit} . This means the 2D posteriors (e.g., M vs. H_0) represent a weighted average over the entire parameter space. When transition-specific parameters are not tightly constrained, their uncertainty is naturally projected onto the marginalized cosmological parameters, leading to broader and more overlapping contours [82].

By contrast, χ^2 contours are computed by scanning over a grid while holding all other parameters fixed at their best-fit values. This approach does not account for parameter uncertainty or degeneracies, resulting in sharper and more separated confidence regions. While this makes χ^2 contours efficient for locating best fits, they can under-represent the full parameter uncertainty, particularly in multi-parameter models.

Degeneracies between M and H_0 are well known. In the presence of poorly constrained transition parameters, as is the case in our analysis, the Bayesian posterior becomes stretched along these degeneracies. This further enhances the overlap in $M-H_0$ and $M-\Omega_m$ planes.

To further illustrate this effect, we examine the 1D marginalized posteriors of the transition-specific parameters (Fig. 14). The 1D marginalized posteriors for the transition parameters $M_<$, $M_>$, and d_{crit} show that while $M_>$ appears better constrained, both $M_<$ and d_{crit} remain broad or even multimodal in the latter case. This implies substantial uncertainty in the modeling of the late-time transition, which is fully accounted for in the Bayesian posterior through marginalization. As a result, the marginalized posteriors in the $M-H_0$ and $M-\Omega_m$ planes appear smoother and more overlapping between the transition and no-transition models.

In contrast, frequentist χ^2 contours are evaluated at fixed best-fit values of all parameters, including the transition ones. This results in narrower confidence regions and sharper separations between models, since no uncertainty is propagated from the weakly constrained parameters. Therefore, the greater overlap observed in the Bayesian contours naturally reflects a more complete treatment of uncertainty and parameter degeneracy.

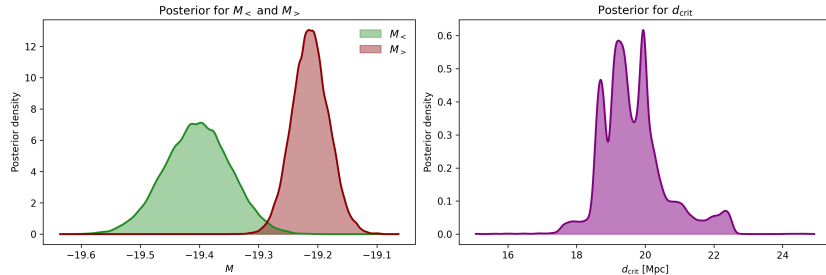


Figure 14: 1D marginalized posteriors for the transition parameters $M_<$, $M_>$, and d_{crit} . The broad and weakly constrained distributions, especially for d_{crit} , explain the enhanced overlap observed in the Bayesian contours.

One could suggest that this overlap could be reduced if higher step count was used. However, going higher than 5000 steps given the tools available was not feasible, so an alternative is to go to a lower step count and see if the overlap increases. We performed the same MCMC sampling, using this time the same amount of 32 walkers, but instead, 2000 steps and 400 burn-ins. We want to test if the overlap changes after using a smaller-step sampler. The parameter values for the no-transition and the transition case are reported in Tables 6 & 7

Parameter	MAP Value	Median	Mean	$\pm 1\sigma$	Unit
M	-19.2477	-19.2474	-19.2476	± 0.0295	
H_0	73.4441	73.4472	73.4486	± 1.0024	km/s/Mpc
Ω_m	0.3324	0.3327	0.3328	± 0.0184	

Table 6: Posterior summary statistics for the parameters in the standard Λ CDM model after using 2000 steps.

Parameter	MAP Value	Median	Mean	$\pm 1\sigma$	Unit
M_{low}	-19.4016	-19.4017	-19.4023	± 0.0563	
M_{high}	-19.2036	-19.2139	-19.2136	± 0.0316	
H_0	74.9416	74.5659	74.5911	± 1.1090	km/s/Mpc
Ω_m	0.3327	0.3326	0.3326	± 0.0183	
d_{crit}	19.9438	19.5166	19.7102	± 0.8830	Mpc

Table 7: Posterior summary statistics for the parameters in the transition model after using 2000 steps.

These results are in excellent agreement with the ones presented in Tables 3 & 4 respectively, indicating that even 2000 steps were enough to perform concrete parameter estimation. Reproduction of the same panels for the 2000-steps-sampler is shown in Figure 15, where we see the same overlap as in Figure 13, with the ellipses being slightly skewed due to the smaller step size used. We therefore conclude that the overlap of the σ levels is not due to the step count, but a reflect of marginalization.

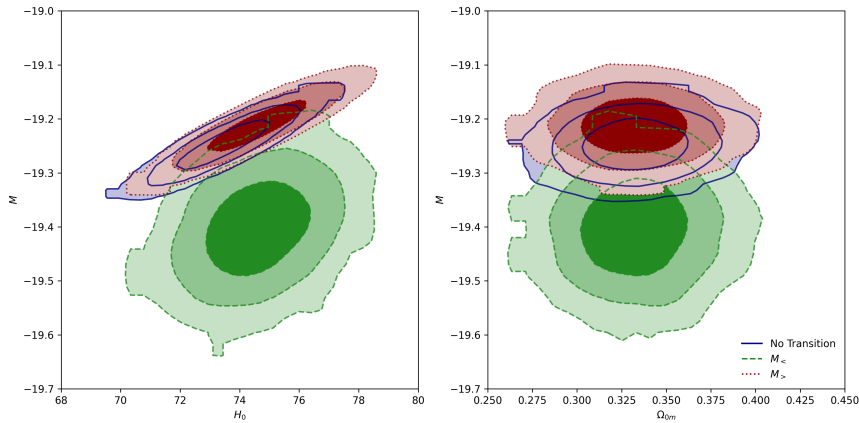


Figure 15: Overlay of Ω_m vs M and H_0 vs M contours for transition and no-transition models in a flat Λ CDM from MCMC sampling after using 2000 steps

Take-home message: *A transition in the SnIa intrinsic luminosity at a critical distance of approximately 20 Mpc is favored by the PANTHEON+ data in the context of a flat Λ CDM model. The value of the Hubble constant, H_0 changes significantly in the transition case, while Ω_m seems to be unaffected.*

4 Expanding the analysis

In Chapter 3, we discussed in depth the flat Λ CDM model and we developed an arsenal that we can use to infer more models. In this chapter we apply the methods that we developed to test the effect of a late-time transition to different cosmological models. Since everything is defined in detail in Chapter 3, we will keep the discussion for the different models short, focusing solely on the results. We highlight here, once again, that the Nested Sampling method is used to only calculate the Bayesian evidence for each model and perform model comparison. The consistent and robust parameter values and contours used are the ones derived with MCMC. However, to ensure that the model comparison is consistent, we do report the median values² derived by the Nested Sampling algorithm and compare them with the ones from MCMC, finding for every model-as we shall prove later- that the values are in agreement.

4.1 Cosmographic Expansion Model up to $\mathcal{O}(z^2)$ order

4.1.1 χ^2 minimization

This model is defined in section 2.5 and the distance modulus in equation (2.48). Before proceeding with discussing the transition, we need to emphasize that we apply a cosmographic expansion, truncated at second-order redshift. We therefore need to define a redshift cut-off scale to ensure statistically and physically meaningful results. A common rule in cosmological analyses, is that when one tries to infer q_0 , he or she should only consider redshifts $z < 0.15$. Therefore, we defined this cut-off scale and via a χ^2 minimization for no-transition in M , we found:

$$M = -19.25 \pm 0.03 \quad (4.1)$$

$$H_0 = 73.1 \pm 1.0 \text{ km/s/Mpc} \quad (4.2)$$

$$q_0 = -0.38 \pm 0.15 \quad (4.3)$$

$$\chi^2_{min} = 748.46 \quad (4.4)$$

Allowing for the transition in M and using the same cut-off, a χ^2 minimization yields:

$$M_< = -19.40222 \pm 0.04666 \quad (4.5)$$

$$M_> = -19.20821 \pm 0.03086 \quad (4.6)$$

$$H_0 = 74.49 \pm 1.11 \text{ km s}^{-1} \text{ Mpc}^{-1} \quad (4.7)$$

$$q_0 = -0.38340 \pm 0.16101 \quad (4.8)$$

$$d_{\text{crit}} = 19.95 \pm 0.10 \text{ Mpc} \quad (4.9)$$

²The reason why median values are used for comparison is because they are more representative, given that they are far less sensitive than the MAP and mean values for slightly skewed and asymmetric posteriors.

The corresponding minimum chi-square is $\chi^2_{\min} = 728.26$. Comparing the minima gives a $\Delta AIC = -16.21$, indicating a strong preference of the transition model and a $\Delta BIC = -6.77$, indicating a moderate preference of the transition model. We see that a late-time transition in M is favored by the data, in the context of a cosmographic expansion. We also derived a q_0 different than -0.55 [67], which corresponds to a standard flat Λ CDM model. This is because we didn't consider redshifts higher than 0.15, trying to be strict while inferring q_0 . To check if this cut-off is correct, we defined a loop of 4 different cut-offs, namely $z = 0.05, 0.10, 0.15, 0.18$. The results for the no-transition and the transition model are shown in tables 8 & 9.

z_{\max}	M	H_0 [km s $^{-1}$ Mpc $^{-1}$]	q_0	χ^2
0.05	-19.25075 ± 0.02941	72.75 ± 1.23	-0.07720 ± 0.69218	600.29
0.10	-19.25008 ± 0.02941	73.10 ± 1.10	-0.40530 ± 0.34609	691.24
0.15	-19.24963 ± 0.02940	73.09 ± 1.04	-0.38445 ± 0.16103	748.46
0.18	-19.24865 ± 0.02940	72.84 ± 1.03	-0.16950 ± 0.11733	823.50

Table 8: Best-fit parameters for increasing redshift cutoffs using the q_0 parametrization.

z_{\max}	$M_<$	$M_>$	H_0 [km s $^{-1}$ Mpc $^{-1}$]	q_0	d_{crit} [Mpc]	χ^2
0.05	-19.40510 ± 0.04674	-19.20891 ± 0.03086	74.18 ± 1.29	-0.10000 ± 0.69314	19.95 ± 0.10	579.62
0.10	-19.40280 ± 0.04668	-19.20863 ± 0.03086	74.49 ± 1.16	-0.40165 ± 0.34593	19.95 ± 0.10	670.99
0.15	-19.40222 ± 0.04666	-19.20821 ± 0.03086	74.49 ± 1.11	-0.38340 ± 0.16101	19.95 ± 0.10	728.26
0.18	-19.40082 ± 0.04664	-19.20734 ± 0.03086	74.22 ± 1.10	-0.17002 ± 0.11733	19.95 ± 0.10	803.41

Table 9: Best-fit parameters for the transition model with varying redshift cut-offs.

We deduce from tables 8 & 9, that $z = 0.15$ is the best cut-off scale, since it gives the most consistent value for q_0 . Going at $z = 0.05$ is wrong, because this regime is dominated by nearby SNe that don't proactively participate in the cosmic expansion, leading to a value with a huge error. At redshift $Z = 0.1$, we see that the q_0 value is close to that of $z = 0.15$, but the uncertainty is larger, due to the smaller number of data used. On the other hand, at $z = 0.18$ we see that the best-fit value is almost equal to its uncertainty, demonstrating that this regime cannot properly constrain q_0 on its own, as higher-order redshifts should be included. The contour plots comparing transition vs no-transition and comparison to the flat Λ CDM case are shown in figure 16.

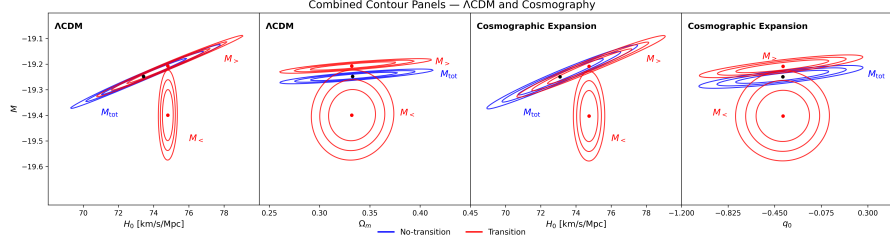


Figure 16: Effect of a late-time transition on a Flat Λ CDM and Cosmographic Model, using a cut-off redshift $z = 0.15$.

4.1.2 MCMC Sampling

No-Transition in M

We start with the no-transition case, using $z = 0.15$ as a cut-off. We adopt uniform priors over the following ranges:

$$\begin{aligned} M &\in [-20.0, -19.0], \\ H_0 &\in [65.0, 78.0] \text{ km s}^{-1} \text{ Mpc}^{-1}, \\ q_0 &\in [-1.0, 0.0]. \end{aligned}$$

The posterior distributions for the three parameters were sampled with `emcee` using 32 walkers with 5000 steps and 1000 burn-ins assigned to each one, and the results are summarized in Table 10.

Parameter	MAP	Median	Mean	$+1\sigma$	-1σ
M	-19.249	-19.248	-19.248	0.0291	0.0289
H_0 [$\text{km s}^{-1} \text{ Mpc}^{-1}$]	73.09	73.14	73.16	1.04	1.01
q_0	-0.381	-0.390	-0.392	0.158	0.159

Table 10: Posterior estimates for the cosmographic model parameters using MCMC.

For all three parameters, the MAP, median, and mean values are closely aligned, suggesting that the posterior distributions are nearly symmetric and unimodal. The differences between the MAP and median for H_0 and q_0 are less than 0.05, and even smaller for M , indicating no significant skewness or multimodality. The associated contours are shown in Figure 17.

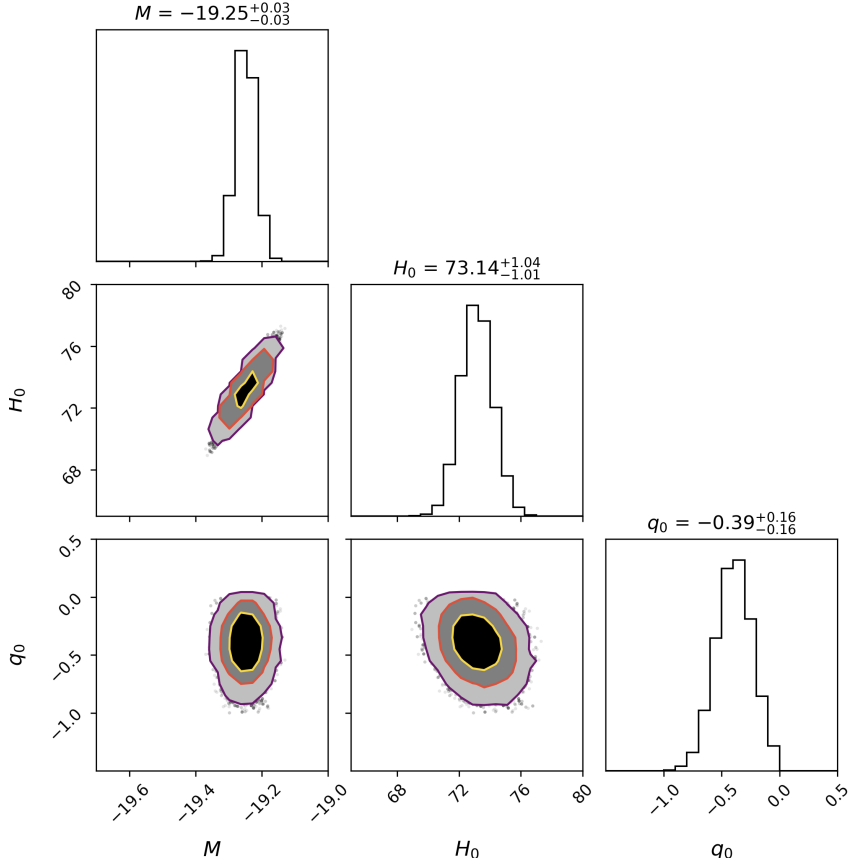


Figure 17: Corner Plot for no-transition cosmography model with the medians and their 1σ uncertainty

To verify the convergence of the MCMC chains, we computed the integrated autocorrelation time τ for each parameter in the cosmography model. The values ranged from $\tau = 36.3$ to 38.0 steps, which is well below the total number of post-burn-in samples per walker. Based on these autocorrelation times, the estimated effective sample sizes (ESS) are approximately 4200–4400 per parameter. These values are significantly larger than the commonly recommended minimum of a few hundred, indicating that the chains have converged well and that the posterior estimates are statistically robust. The resulted chain plot demonstrating the convergence is given in Figure 18.

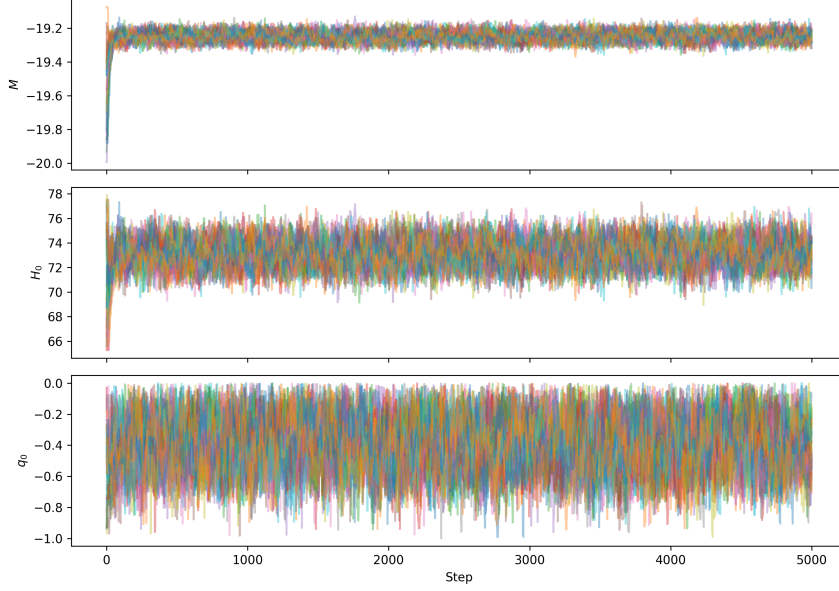


Figure 18: Chain Plot for no-transition cosmography model

Transition in M

Let us now test the effect of the transition in M . Using the same cut-off scale and uniform priors:

$$\begin{aligned} M_< &\in [-20.0, -18.0], \\ M_> &\in [-20.0, -18.0], \\ H_0 &\in [65.0, 78.0] \text{ km s}^{-1} \text{ Mpc}^{-1}, \\ q_0 &\in [-1.0, 0.0]., \\ d_{\text{crit}} &\in [15.0, 25.0] \end{aligned}$$

Using the same sampler set-up of 32 walkers, 5000 steps and 1000 burn-ins, we find:

Parameter	MAP	Median	Mean	$+1\sigma$	-1σ
$M_<$	-19.39856	-19.40447	-19.40538	0.05405	0.05618
$M_>$	-19.20494	-19.21183	-19.21206	0.03105	0.03163
$H_0 [\text{km s}^{-1} \text{ Mpc}^{-1}]$	74.59535	74.37178	74.38157	1.13453	1.11824
q_0	-0.37377	-0.38858	-0.39223	0.15523	0.16307
$d_{\text{crit}} [\text{Mpc}]$	19.95479	19.62551	19.81150	1.17993	0.76687

Table 11: Posterior summary statistics for the cosmographic transition model.

The posterior distributions for most parameters are well-behaved, with MAP,

median, and mean values lying close to each other. For both $M_<$ and $M_>$, the differences are less than 0.01, indicating symmetric and tightly constrained distributions.

For H_0 and q_0 , the MAP values are slightly above their respective medians and means, which reflect mild asymmetries in the posterior tails, though still within one standard deviation, as shown in Figure 19. This pattern is consistent with weak degeneracies among cosmological parameters or sampling noise in broad distributions.

The largest discrepancy is seen again in d_{crit} , where the MAP value (19.95 Mpc) lies noticeably above both the median (19.63 Mpc) and the mean (19.81 Mpc). This suggests a skewed posterior with a broad, asymmetric likelihood structure, as expected for a threshold-like parameter that is not sharply constrained by the data. Overall, the parameter posteriors reflect a well-sampled, informative inference.

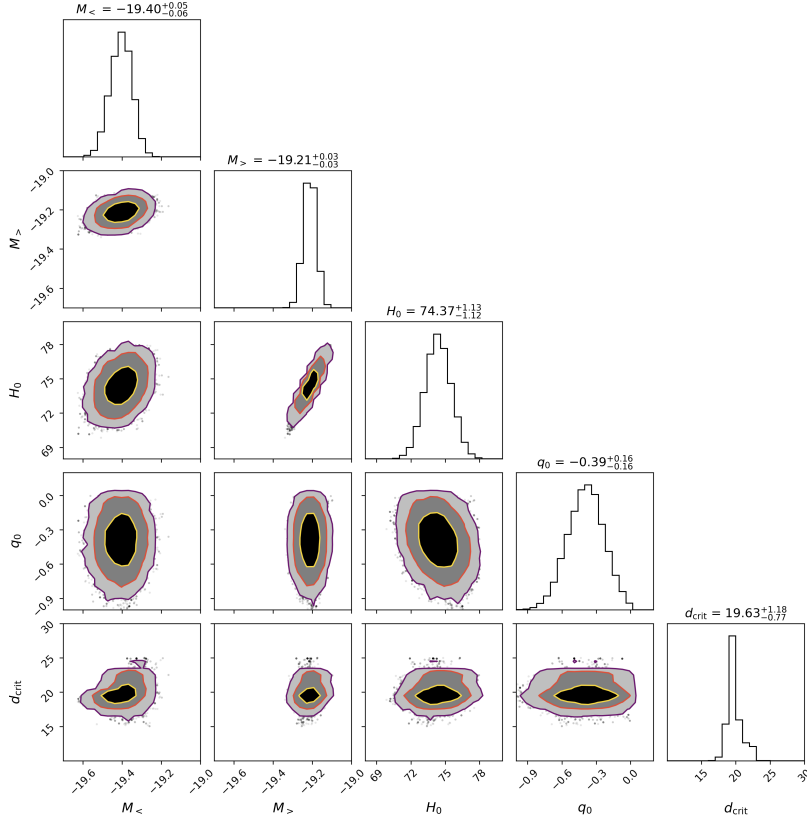


Figure 19: Corner Plot for the transition cosmography model with the medians and their 1σ uncertainty

In addition, the convergence diagnostics indicate that the MCMC sampling was robust and efficient. The autocorrelation time for each parameter ranges between approximately 58 and 77 steps, implying that the chains mix well and do not suffer from excessive correlation. The estimated effective sample sizes (ESS) are all comfortably above 2,000, with the lowest value ($\sim 2,089$) corresponding to the least constrained parameter. These ESS values ensure that the posterior estimates are statistically reliable and the uncertainty estimates are well-resolved. The relatively short autocorrelation times, combined with high ESS, confirm that the sampler thoroughly explored the parameter space and achieved stable convergence as shown in figure 20.

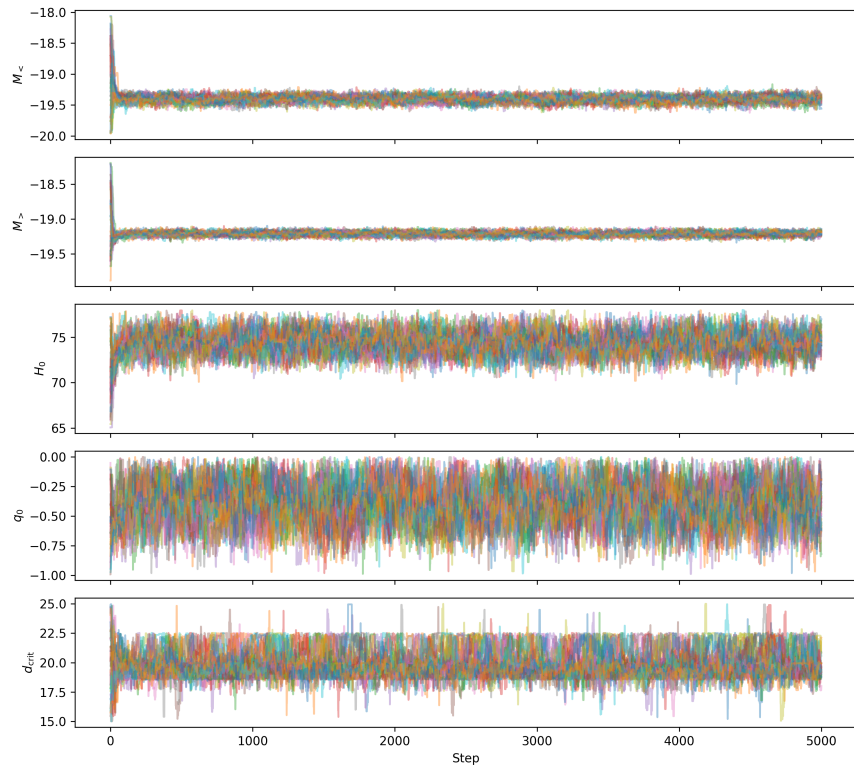


Figure 20: Chain Plot for no-transition cosmography model

4.1.3 Nested Sampling

No-Transition in M

Let us now compare the two models via the Bayes factor. To do that, we need to implement the dynesty sampler, described in section 3. Using again the same priors as in MCMC, 500 live points and a random walk, we find for the

no-transition model:

$$\begin{aligned} M &= -19.2586^{+0.0626}_{-0.1549} \\ H_0 &= 72.8975^{+2.1088}_{-3.4086} \text{ km s}^{-1} \text{ Mpc}^{-1} \\ q_0 &= -0.4280^{+0.2330}_{-0.3076} \end{aligned}$$

The corresponding corner plot is shown in Figure 21. We see no significant differences between the MCMC and the `dynesty` results for the no-transition model, as expected.

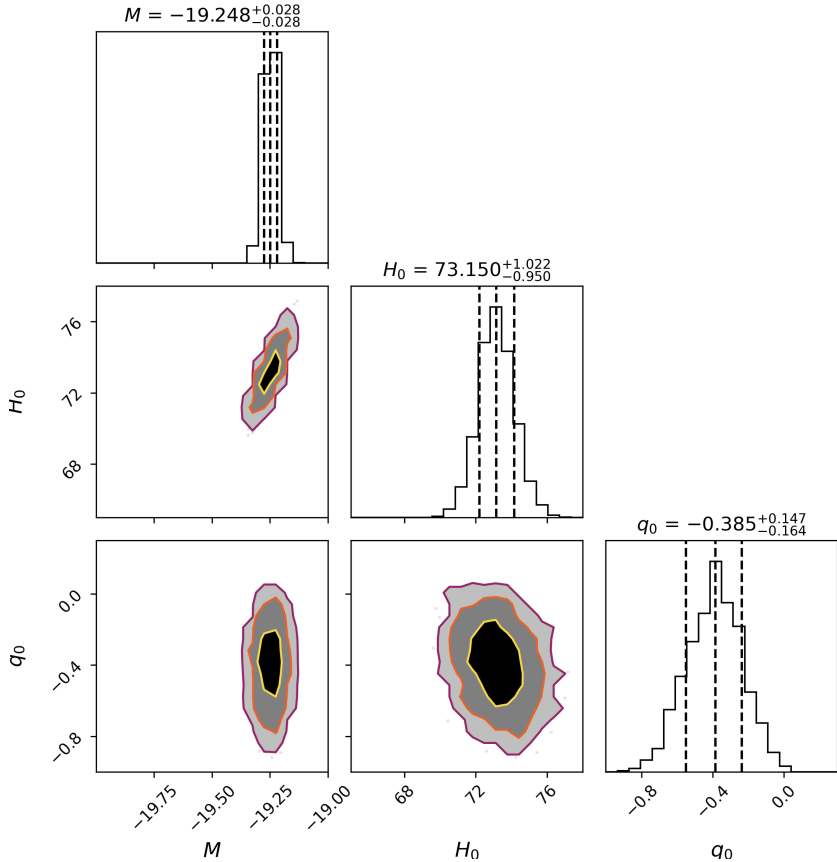


Figure 21: Corner Plot for the no-transition cosmography model with the medians and their 1σ uncertainty, as resulted from the `dynesty` sampler

The `dynesty` run for the cosmographic model converged successfully, as indicated by the termination condition $\Delta \log \mathcal{Z} < 0.001$ being satisfied. The final log-evidence was $\log \mathcal{Z} = -380.906 \pm 0.110$, with an effective sample efficiency

of 6.3% and over 67,000 likelihood evaluations.

Transition in M

Allowing now the transition in M and repeating the exact same process, with the same priors as in MCMC, 500 live points and a random walk, we get the following parameter values and the associated corner plot is shown in figure 22.

$$\begin{aligned} M_< &= -19.3947^{+0.2786}_{-0.1097} \\ M_> &= -19.2208^{+0.0608}_{-0.1054} \\ H_0 &= 73.9638^{+1.7585}_{-3.3796} \text{ km s}^{-1} \text{ Mpc}^{-1} \\ q_0 &= -0.4208^{+0.2201}_{-0.2807} \\ d_{\text{crit}} &= 19.4532^{+2.4061}_{-1.8320} \text{ Mpc} \end{aligned}$$

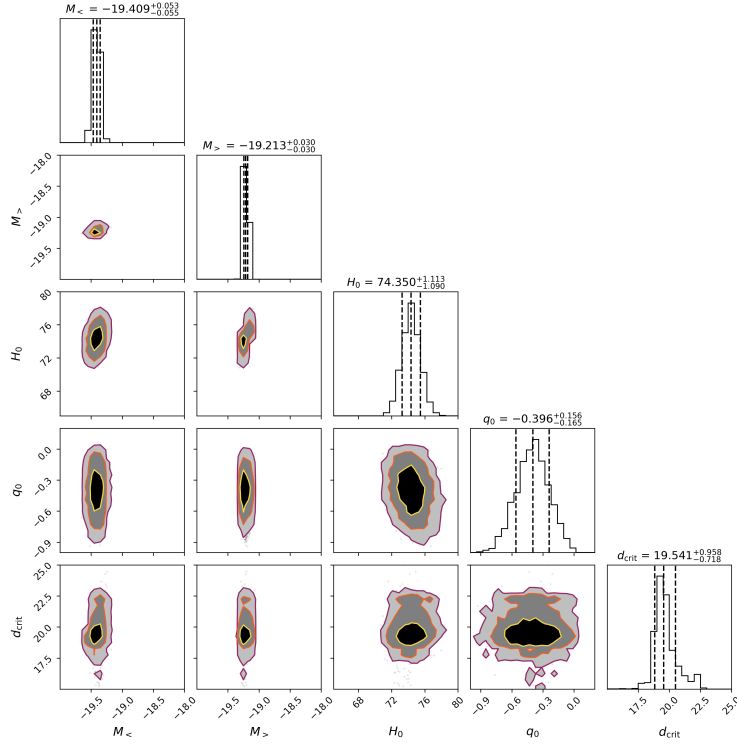


Figure 22: Corner Plot for the transition cosmography model with the medians and their 1σ uncertainty, as resulted from the dynesty sampler

We see some small differences compared to the results from the MCMC, as expected. The introduction of two parameters make the model much more com-

plex, and 500 live points are not enough to provide a consistent constrain. The sampler may have successfully converged, as we will shortly explain, but all the results include larger uncertainties, reflecting this way the few live points used combined with the reduced dataset available. However, our goal using Nested Sampling is to perform model comparison and these small differences are not a red flag. Thus, the model comparison via evidence is consistent.

The nested sampling run for the cosmographic transition model converged successfully. The stopping criterion $\Delta \log \mathcal{Z} < 0.001$ was met, indicating that the estimate of the Bayesian evidence had stabilized. The final log-evidence for the transition model was:

$$\log \mathcal{Z}_{\text{transition}} = -377.489 \pm 0.164 \quad (4.10)$$

This result was obtained after approximately 158,000 likelihood evaluations with a sampling efficiency of 4.7%, confirming a thorough and reliable exploration of the posterior space.

For comparison, the cosmographic model without a transition yielded a log-evidence of:

$$\log \mathcal{Z}_{\text{no-transition}} = -380.91 \pm 0.20.$$

The Bayes factor in favor of the transition model is then:

$$\Delta \log \mathcal{Z} = \log \mathcal{Z}_{\text{transition}} - \log \mathcal{Z}_{\text{no-transition}} = -377.489 - (-380.91) = 3.42. \quad (4.11)$$

According to the Jeffreys scale, this value indicates *moderate evidence* in favor of the transition model. Thus, the Bayesian model comparison suggests that introducing a magnitude transition at a critical scale improves the model's explanatory power in a statistically meaningful way, even after accounting for the additional parameters.

Take-home message: *A transition in the SnIa intrinsic luminosity at a critical distance of approximately 20 Mpc is favored by the PANTHEON+ data in the context of a cosmographic expansion up to second order in redshift. The value of the Hubble constant, H_0 changes significantly in the transition case, while q_0 seems to be unaffected.*

4.2 w_0 CDM Model

This model was defined in Section 2.6, with its distance modulus given in equation (2.52). We now test the effect of a late-time transition in the absolute magnitude M , following the same inference techniques as before.

4.2.1 χ^2 minimization

No-Transition in M

We start with the no-transition case. The minimization yields:

$$M = -19.25 \pm 0.03, \quad (4.12)$$

$$\Omega_m = 0.288 \pm 0.068, \quad (4.13)$$

$$H_0 = 73.3 \pm 1.1 \text{ km s}^{-1} \text{ Mpc}^{-1}, \quad (4.14)$$

$$w_0 = -0.891 \pm 0.15, \quad (4.15)$$

$$\chi_{\min}^2 = 1522.48. \quad (4.16)$$

Transition in M

Allowing now for a transition in M , the best-fit parameters are:

$$M_< = -19.405 \pm 0.05, \quad (4.17)$$

$$M_> = -19.213 \pm 0.03, \quad (4.18)$$

$$H_0 = 74.5 \pm 1.1 \text{ km s}^{-1} \text{ Mpc}^{-1}, \quad (4.19)$$

$$\Omega_m = 0.292 \pm 0.065, \quad (4.20)$$

$$w_0 = -0.899 \pm 0.13, \quad (4.21)$$

$$d_{\text{crit}} = 19.90 \pm 0.4 \text{ Mpc}, \quad (4.22)$$

$$\chi_{\min}^2 = 1507.30. \quad (4.23)$$

Comparing the results, we observe that the transition model introduces a clear separation between $M_<$ and $M_>$, consistent with previous findings. The parameter w_0 remains unchanged, indicating that the late-time transition affects the luminosity calibration more than the underlying expansion dynamics. The Hubble constant H_0 changes, while Ω_m shows only a minor change.

To quantify the model comparison, we compute the AIC and BIC differences:

$$\Delta \text{AIC} = \text{AIC}_{\text{transition}} - \text{AIC}_{\text{no-transition}} = -11.18, \quad (4.24)$$

$$\Delta \text{BIC} = \text{BIC}_{\text{transition}} - \text{BIC}_{\text{no-transition}} = -0.30. \quad (4.25)$$

According to standard information criteria interpretation, the AIC strongly favors the transition model, while the BIC suggests that the two models are statistically indistinguishable. These results provide consistent evidence that a late-time transition in M improves the fit within the w_0 CDM framework,

though not dramatically enough to outweigh the penalty for added parameters in the BIC formalism.

The contour plots showing the 1σ , 2σ and 3σ levels for this model are shown in figures 23 and 24.

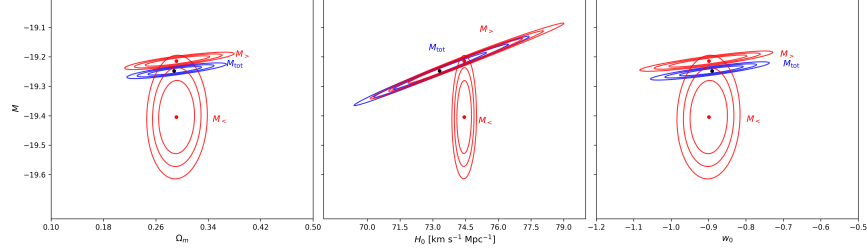


Figure 23: Effect of a late-time transition in a w_0 CDM model. The panels H_0 , Ω_m, w_0 vs M are shown for both a transition and no-transition models.

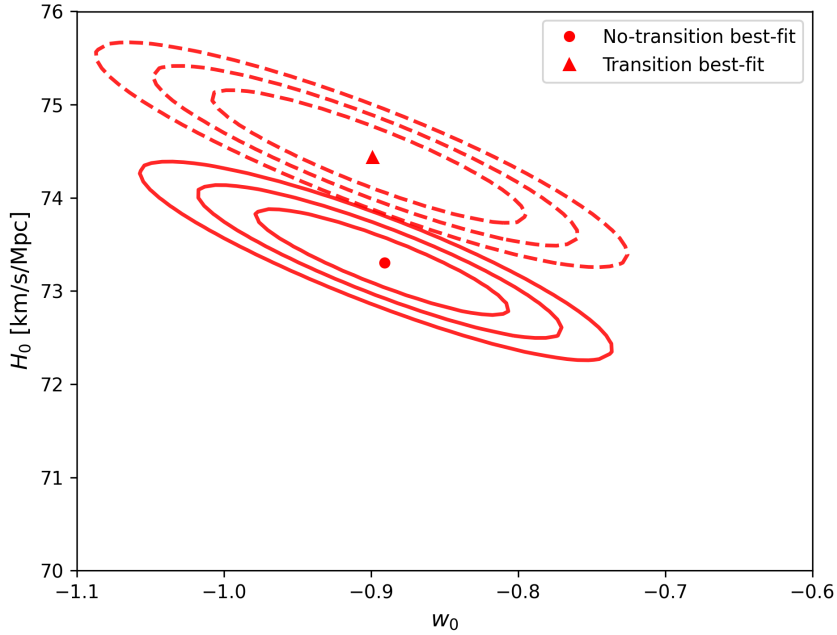


Figure 24: Effect of a late-time transition in a w_0 CDM model depicted on the H_0 vs w_0 panel.

4.2.2 MCMC Sampling

No-Transition in M

We begin with the no-transition case. We adopt uniform priors for the four parameters:

$$\begin{aligned} M &\in [-20.0, -18.0], \\ H_0 &\in [65.0, 78.0] \text{ km s}^{-1} \text{ Mpc}^{-1}, \\ \Omega_m &\in [0.1, 0.8], \\ w_0 &\in [-1.3, 0.0]. \end{aligned}$$

The MCMC sampling was performed using `emcee` with 32 walkers, 5000 steps, and a burn-in phase of 1000 steps. The posterior estimates are summarized in Table 12.

Parameter	MAP	Median	Mean	$\pm 1\sigma$	Unit
M	-19.2464	-19.2470	-19.2471	0.0290	—
H_0	73.3447	73.3185	73.3255	1.0130	$\text{km s}^{-1} \text{ Mpc}^{-1}$
Ω_m	0.2880	0.2871	0.2825	0.0682	—
w_0	-0.8897	-0.8895	-0.8982	0.1416	—

Table 12: Posterior summary statistics for the no-transition w_0 CDM model using MCMC.

The MAP, median, and mean values show excellent agreement across all parameters, suggesting that the posterior distributions are unimodal and nearly symmetric. The slight difference in w_0 between the MAP (-0.8897) and mean (-0.8982) may indicate a mild skewness in the posterior, though it remains within one standard deviation. Similar behavior is observed for Ω_m , while M and H_0 appear tightly constrained and centered.

To verify convergence, we computed the integrated autocorrelation time τ for each parameter:

$$\begin{aligned} \tau_M &= 41.4, & \tau_{H_0} &= 49.1, \\ \tau_{\Omega_m} &= 80.0, & \tau_{w_0} &= 77.8. \end{aligned}$$

All values are much smaller than the number of post-burn-in samples per walker, ensuring reliable chain mixing. The corresponding effective sample sizes (ESS) were:

$$\begin{aligned} N_{\text{eff},M} &\approx 3862, & N_{\text{eff},H_0} &\approx 3255, \\ N_{\text{eff},\Omega_m} &\approx 2000, & N_{\text{eff},w_0} &\approx 2056. \end{aligned}$$

These values far exceed the recommended minimums, confirming robust statistical reliability. The convergence is visually supported by the chain plot in Figure 25 and the structure of the posterior is illustrated in the corner plot of Figure 26.

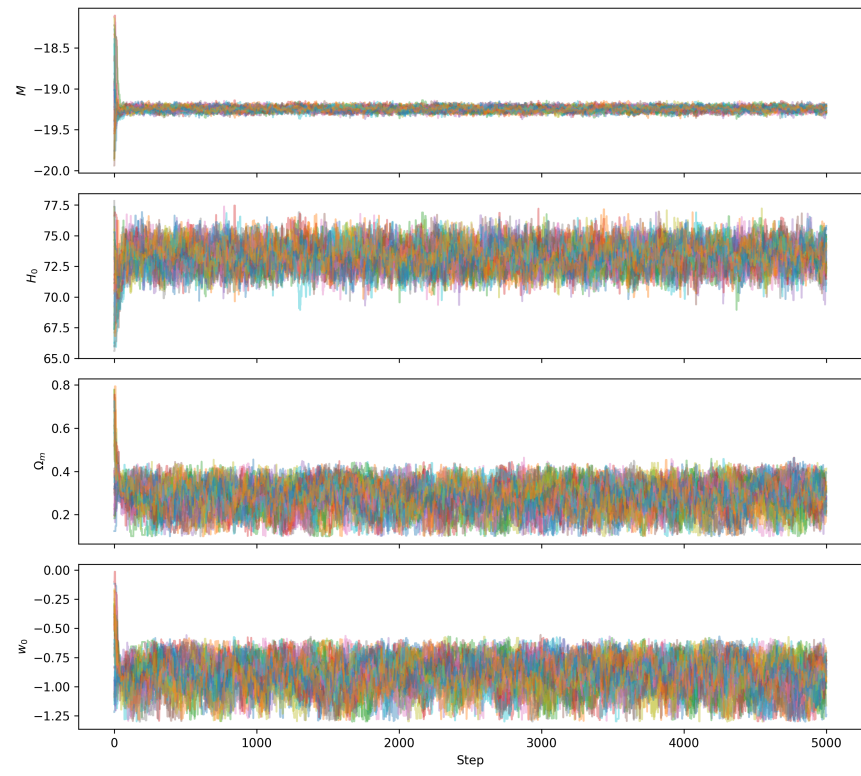


Figure 25: Chain plot for the no-transition w_0 CDM model.

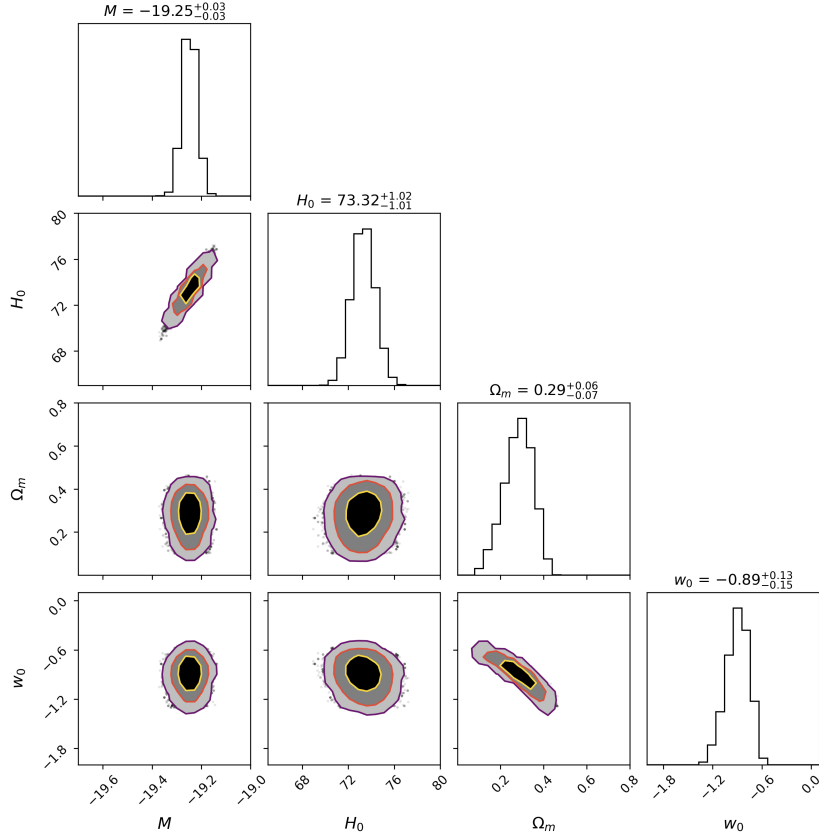


Figure 26: Corner plot for the no-transition w_0 CDM model showing medians and 1σ intervals.

Transition in M

We now allow for a late-time transition in the absolute magnitude M , introducing two values: $M_<$ and $M_>$. The same uniform priors are applied to the cosmological parameters as in the no-transition case, along with an additional prior:

$$d_{\text{crit}} \in [15.0, 25.0] \text{ Mpc.}$$

The MCMC sampling was again performed using `emcee`, with 32 walkers, 5000 steps, and 1000 burn-ins. The posterior estimates are presented in Table 13.

Parameter	MAP	Median	Mean	$\pm 1\sigma$	Unit
$M_<$	-19.3902	-19.3976	-19.3996	0.0559	–
$M_>$	-19.2069	-19.2116	-19.2112	0.0308	–
H_0	74.8037	74.5490	74.5676	1.0776	$\text{km s}^{-1} \text{Mpc}^{-1}$
Ω_m	0.3021	0.2978	0.2908	0.0688	–
w_0	-0.9302	-0.9133	-0.9202	0.1519	–
d_{crit}	19.9622	19.5856	19.7435	0.8934	Mpc

Table 13: Posterior summary statistics for the transition w_0 CDM model using MCMC.

As in the no-transition case, most parameter distributions are well-behaved. The MAP, median, and mean values for $M_<$, $M_>$, and H_0 are in close agreement, indicating symmetric and tightly constrained posteriors. A small discrepancy between the mean and MAP of w_0 hints at mild skewness, and a similar trend is seen for Ω_m and d_{crit} , due to extended tails in the likelihood surface.

To confirm convergence, we computed the integrated autocorrelation time τ for each parameter:

$$\begin{aligned}\tau_{M_<} &= 74.0, & \tau_{M_>} &= 73.7, & \tau_{H_0} &= 93.6, \\ \tau_{\Omega_m} &= 125.1, & \tau_{w_0} &= 126.8, & \tau_{d_{\text{crit}}} &= 105.4.\end{aligned}$$

All values remain significantly below the number of post-burn-in samples, confirming efficient mixing. The corresponding effective sample sizes were:

$$\begin{aligned}N_{\text{eff},M_<} &\approx 2162, & N_{\text{eff},M_>} &\approx 2172, & N_{\text{eff},H_0} &\approx 1710, \\ N_{\text{eff},\Omega_m} &\approx 1278, & N_{\text{eff},w_0} &\approx 1262, & N_{\text{eff},d_{\text{crit}}} &\approx 1517.\end{aligned}$$

These values comfortably exceed convergence thresholds and validate the statistical robustness of the inference. The chain plot confirming this behavior is shown in Figure 27, and the full posterior structure is visualized in the corner plot of Figure 28.

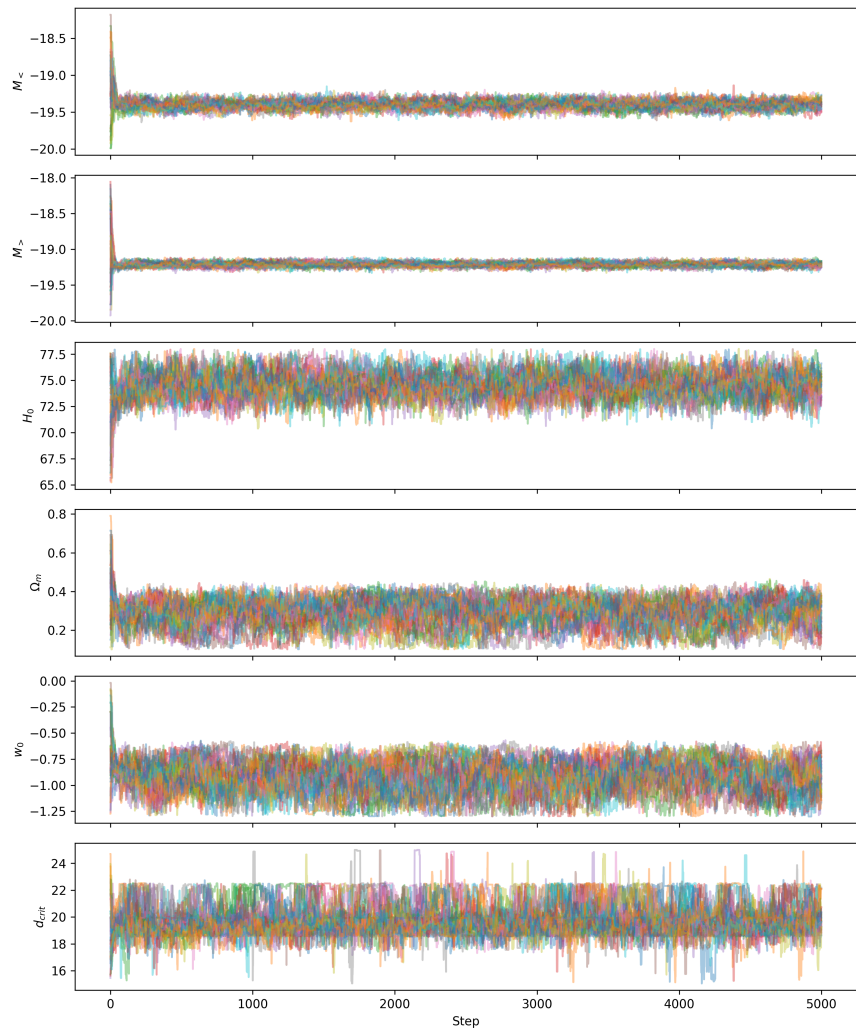


Figure 27: Chain plot for the transition w_0 CDM model.

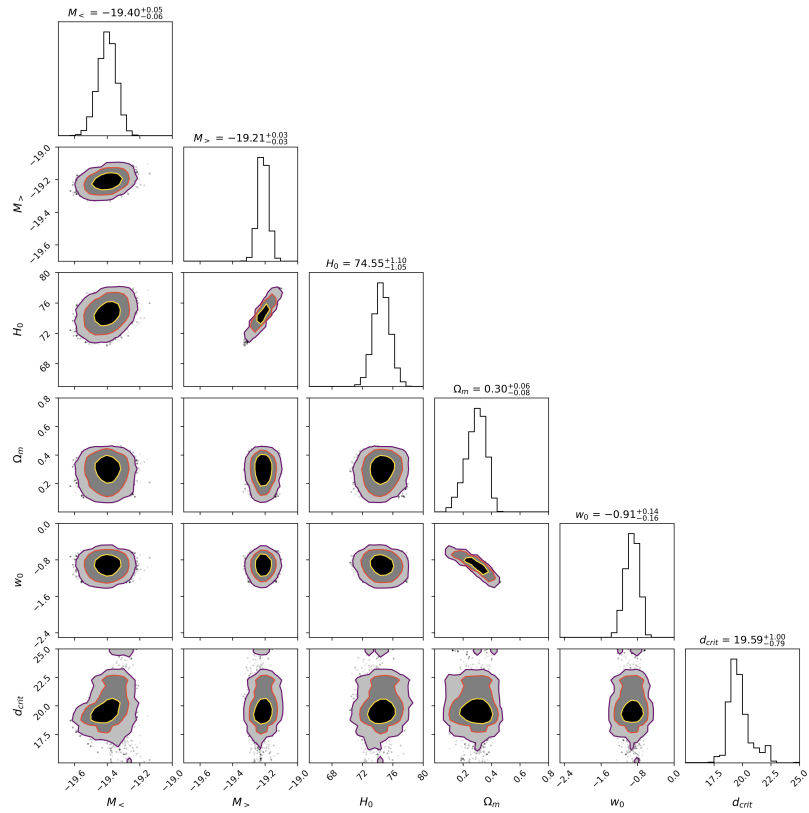


Figure 28: Corner plot for the transition w_0 CDM model showing medians and 1σ intervals.

4.2.3 Nested Sampling

No-Transition in M

We now use the `dynesty` sampler to compute the Bayesian evidence for both the no-transition and transition cases of the w_0 CDM model. For the no-transition case, we used 500 live points. The sampler converged successfully with the following diagnostics:

```
5902it [1:25:26, 1.15it/s, +500 — bound: 47 — nc: 1 — ncall:  
125440 — eff(%) = 5.12 — logz: -772.358 ± 0.148]
```

The medians with their 1σ uncertainty and the contour plots are shown in Figure 29. Comparison with the corresponding results from MCMC show good agreement, ensuring this way that we are safe to proceed with model comparison.

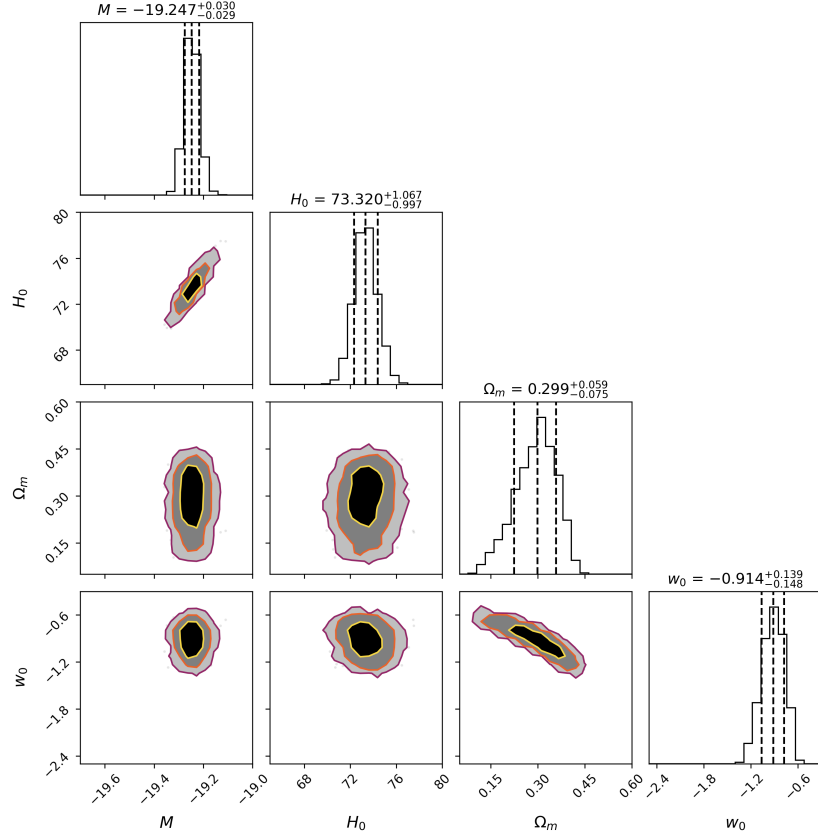


Figure 29: Corner plot for the no-transition w_0 CDM model and median parameter values with their 1σ uncertainty, using the `dynesty` sampler.

Transition in M

In the transition case, two additional parameters are included. Due to the higher dimensionality of the transition model - 6 parameters- we reduced the number of live points to 250 to ensure computational feasibility. Despite this, the run converged successfully with:

```
4463it [1:16:14, 1.03s/it, +250 — bound: 45 — nc: 1 — ncall:  
118902 — eff(%) = 3.97 — logz: -768.280 ± 0.237]
```

The corresponding median values with their 1σ uncertainty and the contour plots are shown in Figure 30. We see again an agreement with the corresponding values from MCMC, ensuring a consistent model comparison.

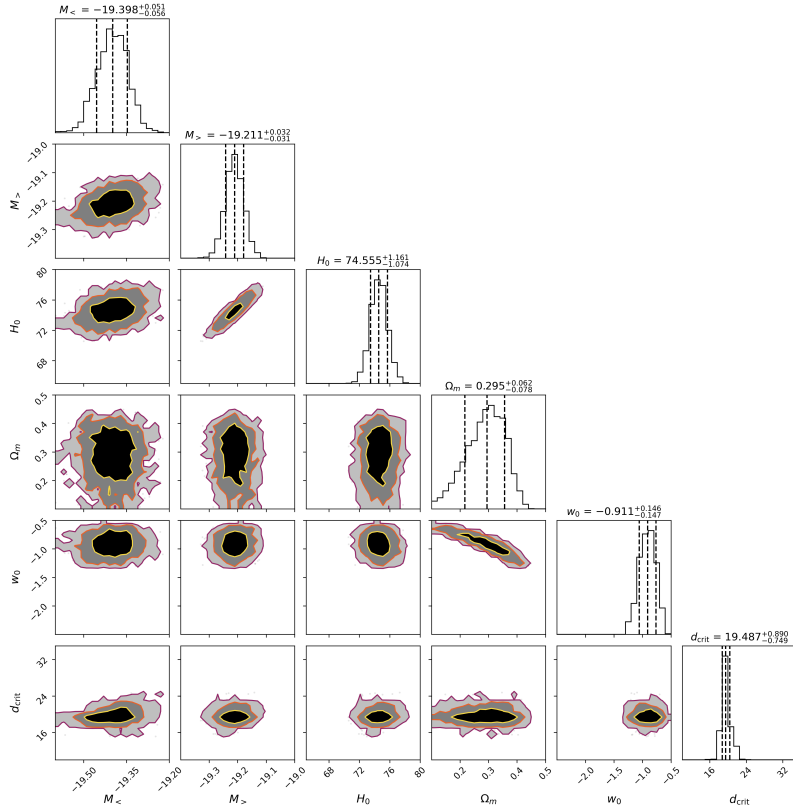


Figure 30: Corner plot for the transition w_0 CDM model and median parameter values with their 1σ uncertainty, using the dynesty sampler.

The process here used different number of live points for the two models, so one could argue that the comparison is not consistent. However, this is not the

case. We see that the uncertainty in both evidences is relatively small enough, so the use of 500 points in the no-transition model only provides a good uncertainty, meaning that even if we changed the number of live points to 250, the evidence would be the same with only its uncertainty being slightly but not significantly higher. Using 500 live points for the transition model with 6 parameters made the code crash, while the same number of live points for 4 parameters worked fine. Therefore, 5 parameters is the critical value, around which the number of live points used should change. As our goal is solely to compute the model evidence, we do not present the MAP values, posterior plots, or corner diagrams from the `dynesty` output, since these were already thoroughly analyzed in the MCMC section above.

The resulting Bayesian evidences are:

$$\log \mathcal{Z}_{\text{no-transition}} = -772.358 \pm 0.148, \quad (4.26)$$

$$\log \mathcal{Z}_{\text{transition}} = -768.280 \pm 0.237. \quad (4.27)$$

The Bayes factor is thus:

$$\Delta \log \mathcal{Z} = \log \mathcal{Z}_{\text{transition}} - \log \mathcal{Z}_{\text{no-transition}} = -768.280 - (-772.358) = 4.078. \quad (4.28)$$

According to the Jeffreys scale, this corresponds to *moderate evidence* in favor of the transition model. Therefore, even after accounting for its additional complexity, the data modestly prefer the model with a late-time transition in M .

Take-home message: *A transition in the SnIa intrinsic luminosity at a critical distance of approximately 20 Mpc is favored by the PANTHEON+ data in the context of the flat w_0 CDM model. The value of the Hubble constant, H_0 changes significantly in the transition case, while the values of Ω_m and w_0 remain roughly the same.*

4.3 CPL Model

For the Chevallier–Polarski–Linder (CPL) model, a χ^2 minimization approach was not feasible due to the complexity of the model. In particular, the parameter space proved too irregular to construct a reliable cubic grid around the best-fit point, rendering Fisher matrix estimation of uncertainties unreliable. As a result, we analyze the CPL model exclusively via MCMC and nested sampling techniques, focusing on the effect of a potential transition in the absolute magnitude M .

4.3.1 MCMC Sampling

No-Transition in M

We begin with the no-transition case. The priors applied to the CPL model parameters are:

$$\begin{aligned} M &\in [-20.0, -18.0], \\ H_0 &\in [60.0, 85.0] \text{ km s}^{-1} \text{ Mpc}^{-1}, \\ \Omega_m &\in [0.1, 0.5], \\ w_0 &\in [-2.0, 0.0], \\ w_a &\in [-2.0, 2.0]. \end{aligned}$$

The MCMC sampling was performed with `emcee` using 32 walkers, 5000 steps, and a burn-in of 1000 steps. The posterior results are reported in Table 14.

Parameter	MAP	Median	Mean	$\pm 1\sigma$	Unit
M	-19.2522	-19.2485	-19.2481	0.0291	—
H_0	73.1364	73.2912	73.3056	1.0385	$\text{km s}^{-1} \text{ Mpc}^{-1}$
Ω_m	0.2678	0.3220	0.3063	0.0898	—
w_0	-0.8658	-0.9131	-0.9257	0.1421	—
w_a	0.1066	-0.2474	-0.3177	0.9611	—

Table 14: Posterior summary statistics for the no-transition CPL model using MCMC.

Convergence diagnostics confirmed stable and well-mixed chains. The integrated autocorrelation times were:

$$\begin{aligned} \tau_M &= 55.7, & \tau_{H_0} &= 66.7, & \tau_{\Omega_m} &= 141.0, \\ \tau_{w_0} &= 102.7, & \tau_{w_a} &= 107.2. \end{aligned}$$

Corresponding effective sample sizes were:

$$\begin{aligned} N_{\text{eff},M} &\approx 2870, & N_{\text{eff},H_0} &\approx 2399, \\ N_{\text{eff},\Omega_m} &\approx 1134, & N_{\text{eff},w_0} &\approx 1558, & N_{\text{eff},w_a} &\approx 1492. \end{aligned}$$

These values indicate that the sampling is statistically reliable. The associated trace plots confirming convergence are shown in Figure 31.

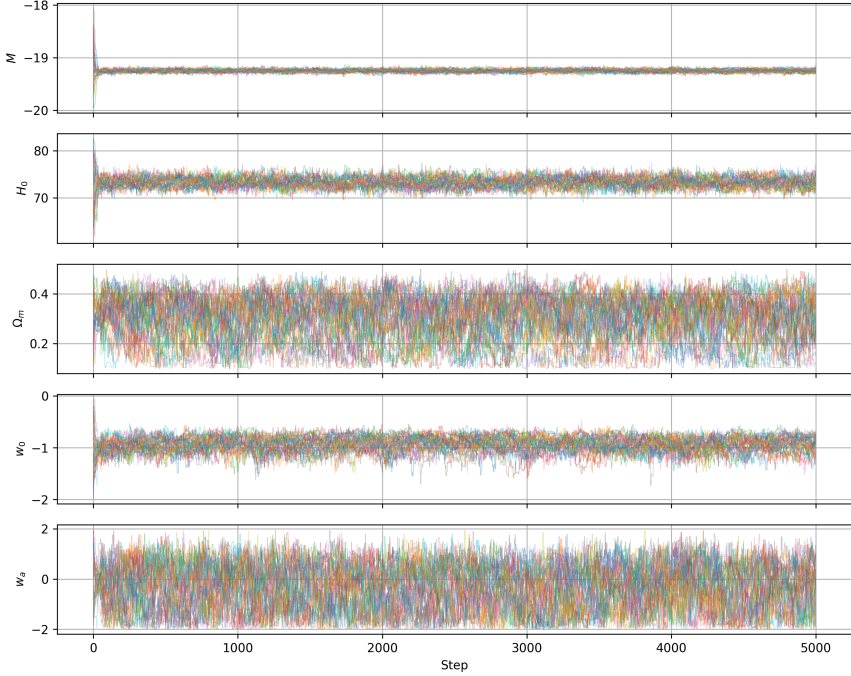


Figure 31: Chain plot for the no-transition CPL model.

The inferred posterior distributions reveal several features. While most parameters are well constrained, the parameter w_a shows a notably broad distribution with a 1σ uncertainty approaching unity. This large uncertainty reflects the well-known degeneracy between w_0 and w_a , particularly in the absence of complementary datasets such as Baryon Acoustic Oscillations (BAO) or Cosmic Microwave Background (CMB) priors. While our supernova dataset provides strong constraints on M , H_0 , and w_0 , the CPL model's time-evolving dark energy component (w_a) remains weakly constrained under these data alone. A comprehensive treatment would require joint constraints with multiple cosmological probes, which is beyond the scope of this work. In addition, we see a discrepancy in the MAP, median and mean values of Ω_m , which reflects a skewness of the tail toward lower values as shown in the corner plot summarizing the full posterior structure, Figure 32.

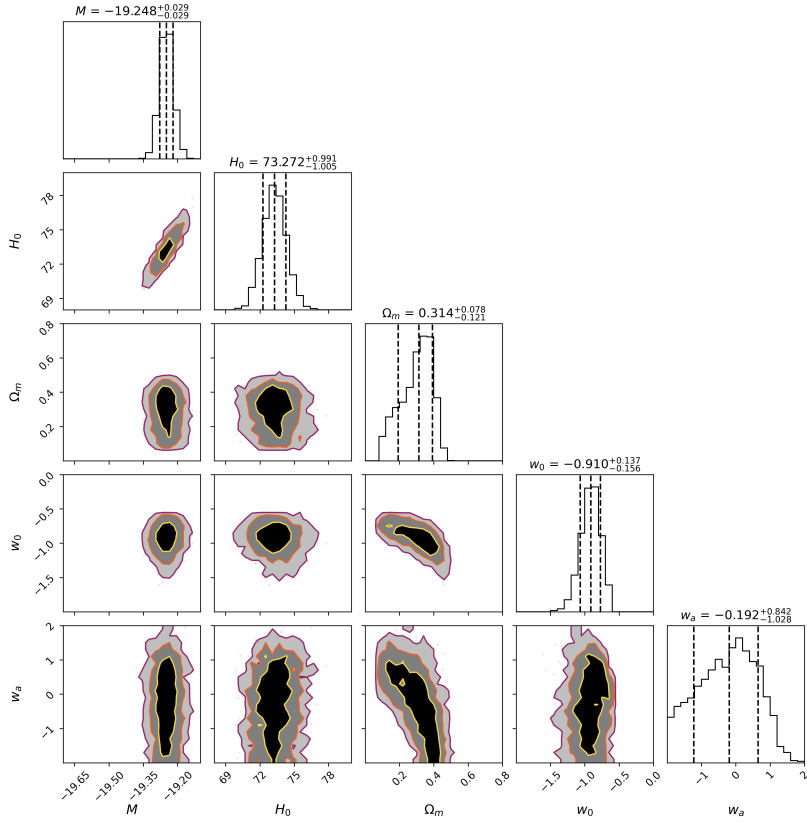


Figure 32: Corner plot for the no-transition CPL model showing posterior distributions and 1σ credible intervals.

Transition in M

We now investigate the CPL model allowing for a transition in the absolute magnitude M . The priors are defined as:

$$\begin{aligned}
 M_{<}, M_{>} &\in [-20.0, -18.0], \\
 H_0 &\in [60.0, 85.0] \text{ km s}^{-1} \text{ Mpc}^{-1}, \\
 \Omega_m &\in [0.1, 0.5], \\
 w_0 &\in [-2.0, 0.0], \\
 w_a &\in [-2.0, 2.0], \\
 d_{\text{crit}} &\in [15.0, 25.0] \text{ Mpc}.
 \end{aligned}$$

We used the same MCMC setup: 32 walkers, 5000 steps, and 1000 burn-ins. The inferred posterior statistics are reported in Table 15.

Parameter	MAP	Median	Mean	$\pm 1\sigma$	Unit
$M_<$	-19.3973	-19.4008	-19.4017	0.0561	–
$M_>$	-19.2173	-19.2104	-19.2108	0.0313	–
H_0	74.2495	74.5647	74.5679	1.1137	$\text{km s}^{-1} \text{Mpc}^{-1}$
Ω_m	0.2150	0.3295	0.3135	0.0870	–
w_0	-0.8060	-0.9261	-0.9363	0.1396	–
w_a	0.3192	-0.3291	-0.3687	0.9726	–
d_{crit}	19.9508	19.5032	19.6637	0.7938	Mpc

Table 15: Posterior summary statistics for the CPL transition model using MCMC.

The convergence of the chains was verified via the integrated autocorrelation time:

$$\begin{aligned}\tau_{M_<} &= 93.3, & \tau_{M_>} &= 83.5, & \tau_{H_0} &= 107.6, \\ \tau_{\Omega_m} &= 226.5, & \tau_{w_0} &= 185.9, & \tau_{w_a} &= 183.2, & \tau_{d_{\text{crit}}} &= 120.0.\end{aligned}$$

The corresponding effective sample sizes were:

$$\begin{aligned}N_{\text{eff},M_<} &\approx 1715, & N_{\text{eff},M_>} &\approx 1916, & N_{\text{eff},H_0} &\approx 1486, \\ N_{\text{eff},\Omega_m} &\approx 706, & N_{\text{eff},w_0} &\approx 860, & N_{\text{eff},w_a} &\approx 873, & N_{\text{eff},d_{\text{crit}}} &\approx 1333.\end{aligned}$$

These statistics confirm that the chains have converged and the parameter space has been sufficiently sampled. Figure 33 shows the corresponding chain plot.

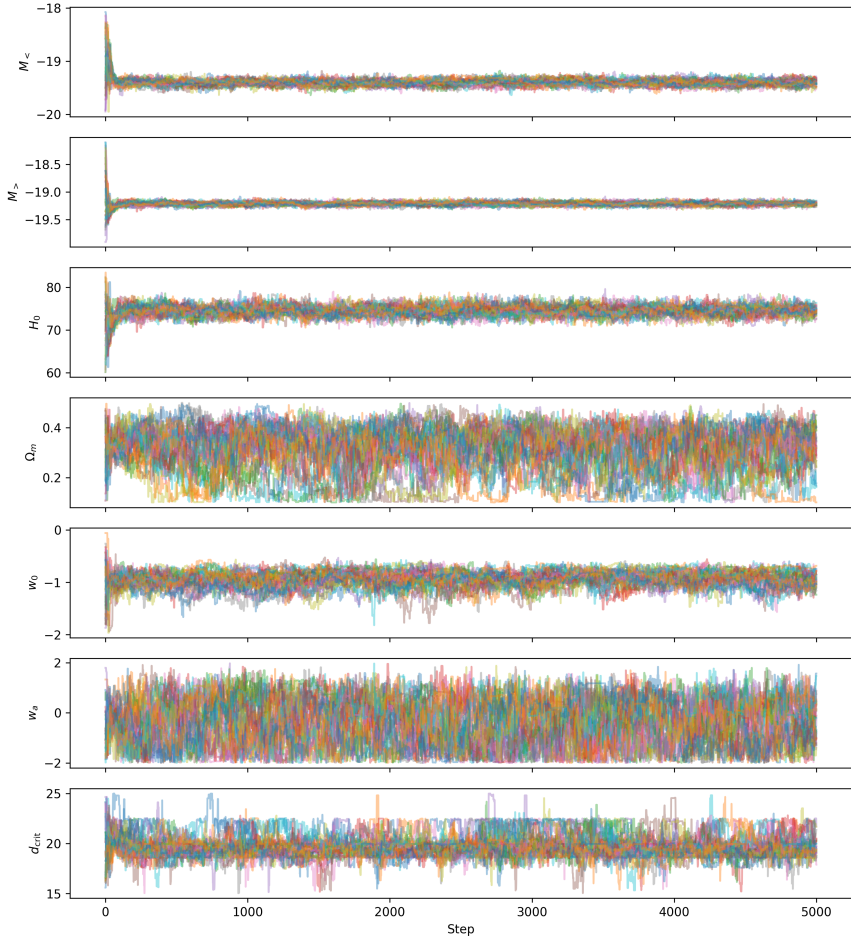


Figure 33: Chain plot for the CPL transition model.

As with the no-transition case, the parameters $M_{<}$, $M_{>}$, Ω_m and H_0 are well constrained and the same discrepancy between the Ω_m values as in the no-transition case is present. The posterior distributions for w_0 and w_a remain broad, reflecting the intrinsic degeneracy between these parameters and the limitations of using only supernova data. In particular, the spread in w_a remains significant ($\sigma \sim 1$), indicating that time evolution in the dark energy equation of state is weakly constrained. Again, this highlights the need for joint analyses with complementary datasets such as BAO or CMB to fully constrain CPL models. The structure of the posterior is illustrated in the corner plot in Figure 34.

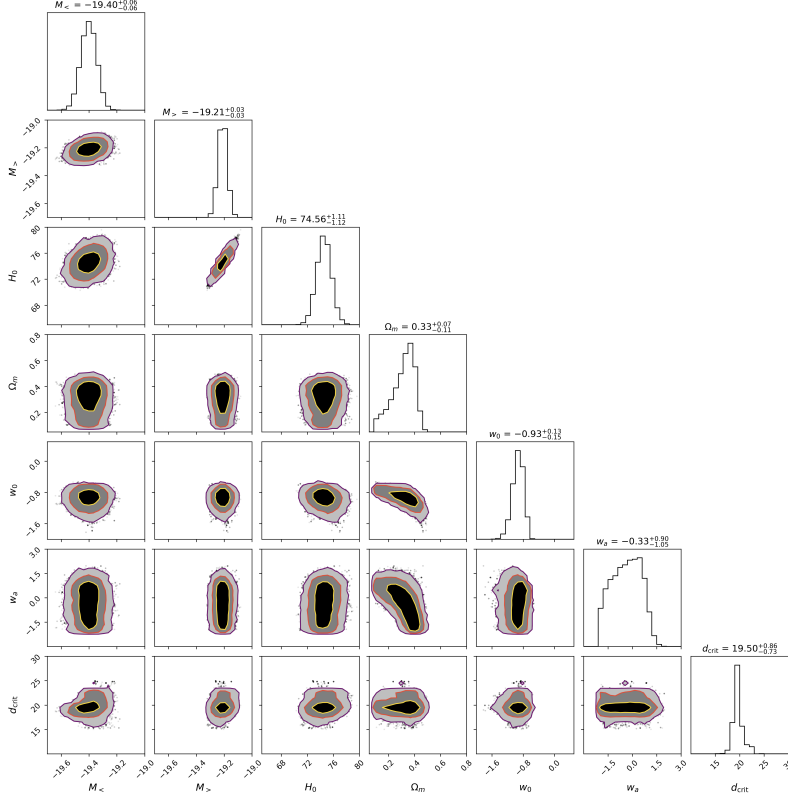


Figure 34: Corner plot for the CPL transition model showing posterior distributions and 1σ credible intervals.

4.3.2 Nested Sampling

No-Transition in M

We now apply the `dynesty` sampler to the CPL model to compute the Bayesian evidence and perform model comparison between the no-transition and transition cases. As in previous models, we are only interested in the evidence itself; the posterior distributions have already been explored in detail via MCMC.

Due to the high dimensionality of the parameter space, we used 250 live points for both the no-transition and transition models. Despite the reduced live count, both runs achieved excellent convergence.

The run for the no-transition model terminated successfully with the following summary:

```
3369it [1:20:10, 1.43s/it, +250 — bound: 30 — nc: 1 — ncall: 80720
— eff(%) = 4.50 — logz: -773.352 ± 0.209]
```

The contour plots and the parameter medians with their 1σ uncertainty are shown in figure 35. We see again a general agreement between these values and the corresponding ones from MCMC.

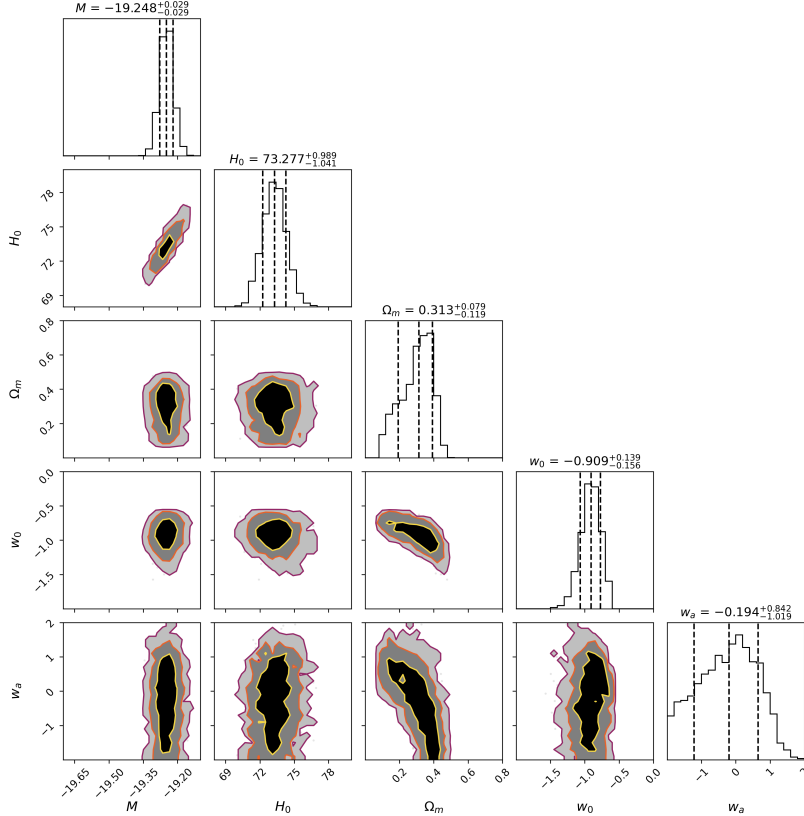


Figure 35: Corner plot for the no-transition CPL model and median parameter values with their 1σ uncertainty, using the dynesty sampler.

Transition in M

Similarly, the transition model was sampled thoroughly with:

```
4824it [2:07:51, 1.59s/it, +250 — bound: 48 — nc: 1 — ncall:  
132707 — eff(%) = 3.83 — logz: -769.659 ± 0.250]
```

The contour plots and the parameter medians with their 1σ uncertainty are shown in figure 36. We see again a general agreement between these values and the corresponding ones from MCMC.

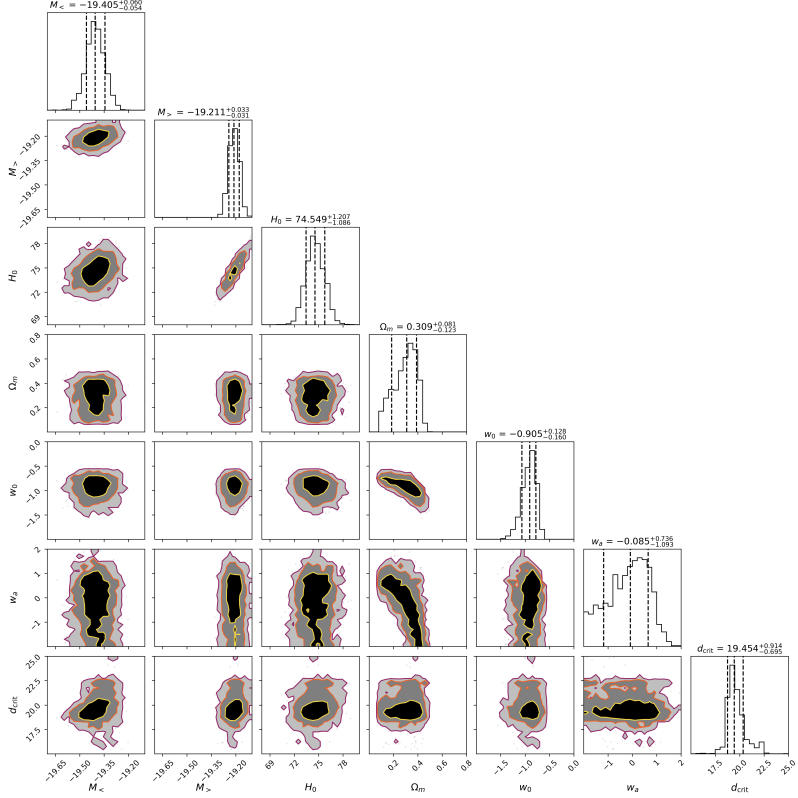


Figure 36: Corner plot for the transition CPL model and median parameter values with their 1σ uncertainty, using the dynesty sampler.

The evidence estimates are:

$$\log \mathcal{Z}_{\text{no-transition}} = -773.352 \pm 0.209, \quad (4.29)$$

$$\log \mathcal{Z}_{\text{transition}} = -769.659 \pm 0.250. \quad (4.30)$$

We compute the Bayes factor as:

$$\Delta \log \mathcal{Z} = \log \mathcal{Z}_{\text{transition}} - \log \mathcal{Z}_{\text{no-transition}} = -769.659 - (-773.352) = 3.693. \quad (4.31)$$

According to the Jeffreys scale, this corresponds to *moderate evidence* in favor of the transition model. Thus, even in the extended CPL framework, the inclusion of a magnitude transition improves the model's explanatory power in a statistically meaningful way.

Take-home message: *A transition in the SnIa intrinsic luminosity at a critical distance of approximately 20 Mpc is favored by the PANTHEON+ data in the context of the flat CPL model. The value of the Hubble constant, H_0 changes significantly in the transition case, while the values of Ω_m , w_0 and w_a change only slightly. However, the PANTHEON+ dataset alone cannot provide powerful constraints to the CPL model, and BAO with CMB data need to be also included for a consistent inference.*

5 Summary and Discussion

Inference Framework for Cosmological Parameter Estimation with Type Ia Supernovae. In this thesis, we constructed a complete theoretical and statistical framework to investigate cosmological models using Type Ia Supernovae (SnIa) as standard candles. Our primary goal was to assess the impact of a possible late-time transition in the absolute magnitude M on the best-fit values of various cosmological parameters. To that end, we implemented and cross-validated three distinct inference methods: χ^2 minimization, Markov Chain Monte Carlo (MCMC) sampling via `emcee`, and nested sampling via `dynesty`.

As a benchmark, we successfully reproduced the results of Perivolaropoulos & Skara (P&S)[2] for the flat Λ CDM model using χ^2 minimization. This not only validated our data processing and statistical methodology but also laid the foundation for applying the same techniques to a broader class of cosmological models. We extended the analysis to include MCMC sampling for posterior exploration, which allowed us to examine the full likelihood landscape, quantify uncertainties more robustly, and assess parameter degeneracies.

To perform principled model comparison within the Bayesian framework, we employed the `dynesty` nested sampling algorithm. This approach provided reliable estimates of the Bayesian evidence, enabling us to compute Bayes factors and apply the Jeffreys scale to evaluate the support for the transition model over the no-transition hypothesis.

Results and possible implications. Across all models tested, the inclusion of a late-time transition in the absolute magnitude of Type Ia supernovae (M) led to a consistent preference for a two-value structure ($M_<$ and $M_>$). Notably, the only cosmological parameter systematically affected by this transition was the Hubble constant H_0 , while parameters like Ω_m , q_0 , w_0 and w_a remained in general unaffected. This suggests that the redshift dependence of M directly modulates the inferred cosmic expansion rate today.

While one could attribute such a signal to a residual volumetric redshift scatter bias, we tested this possibility by removing all data below $z < 0.01$, where this effect is most pronounced. The result persisted—albeit more mildly—still favoring a transition. This makes it unlikely that the signal arises solely from this known systematic.

An intriguing alternative explanation is that the transition reflects a physical change in the underlying cosmological model—specifically, a late-time variation in the gravitational constant G [31, 83, 84, 85, 86, 87]. In several modified gravity scenarios, such as scalar-tensor theories or screening models, a redshift-dependent G would alter the Chandrasekhar mass and thus the intrinsic luminosity of supernovae. This would manifest observationally as an evolving M , and if unaccounted for, would bias the inference of H_0 . Therefore, our results may hint at the presence of hidden low-redshift physics, potentially signaling a breakdown of the standard assumption of a constant G in the local Universe.

Possible extensions of this work. Future extensions of this work could incorporate joint constraints from additional cosmological probes such as Baryon Acoustic Oscillations (BAO), Cosmic Microwave Background (CMB) anisotropies, and gravitational lensing. These data sets would help further constrain the CPL parameters and test the robustness and consistency of the inferred transition in M . In particular, combining distance indicators with independent measurements of the Hubble constant could clarify the extent to which the M transition is responsible for the H_0 tension.

Furthermore, the observational signature of a redshift-dependent absolute magnitude may hint at new physics beyond Λ CDM. For example, a transition in the effective gravitational constant $G_{\text{eff}}(z)$, as predicted by several modified gravity theories (e.g., scalar-tensor models or screened gravity scenarios), would induce a change in the Chandrasekhar mass and hence the intrinsic luminosity of Type Ia supernovae. Future work could explicitly embed such models into the transition framework and explore whether the magnitude evolution is consistent with theoretical predictions from $G(z)$ -driven cosmologies.

Finally, further exploration of redshift-dependent astrophysical systematics, such as evolution in the supernova population, host-galaxy effects, or selection biases, is essential. Disentangling such effects from genuine physical transitions will be crucial in assessing whether the observed signal represents a systematic artifact or a deeper insight into the fundamental physics driving cosmic acceleration.

Acknowledgments

I would like to express my deepest gratitude to my supervisors, Subodh and Leandros, for taking me under their wings without a second thought and guiding me throughout this journey. I would also like to express my gratitude to my study advisor, Hara Papathanasiou, for being there and supporting me during some tough times.

References

- [1] Dillon Brout, Dan Scolnic, Brodie Popovic, Adam G Riess, Anthony Carr, Joe Zuntz, Rick Kessler, Tamara M Davis, Samuel Hinton, David Jones, et al. The pantheon+ analysis: cosmological constraints. *The Astrophysical Journal*, 938(2):110, 2022.
- [2] Leandros Perivolaropoulos and Foteini Skara. On the homogeneity of snia absolute magnitude in the pantheon+ sample. *Monthly Notices of the Royal Astronomical Society*, 520(4):5110–5125, 2023.
- [3] Albert Einstein. Die feldgleichungen der gravitation. *Sitzungsberichte der Königlich Preußischen Akademie der Wissenschaften*, pages 844–847, 1915.
- [4] Michael Paul Hobson, George P Efstathiou, and Anthony N Lasenby. *General relativity: an introduction for physicists*. Cambridge university press, 2006.
- [5] N Aghanim, Y Akrami, M Ashdown, J Aumont, C Baccigalupi, M Ballardini, AJ Banday, RB Barreiro, N Bartolo, S Basak, et al. Planck 2018 results. vi. cosmological parameters. 2020.
- [6] David W Hogg, Daniel J Eisenstein, Michael R Blanton, Neta A Bahcall, J Brinkmann, James E Gunn, and Donald P Schneider. Cosmic homogeneity demonstrated with luminous red galaxies. *The Astrophysical Journal*, 624(1):54, 2005.
- [7] Morag I Scrimgeour, Tamara Davis, Chris Blake, J Berian James, Gregory B Poole, Lister Staveley-Smith, Sarah Brough, Matthew Colless, Carlos Contreras, Warrick Couch, et al. The wigglez dark energy survey: the transition to large-scale cosmic homogeneity. *Monthly Notices of the Royal Astronomical Society*, 425(1):116–134, 2012.
- [8] Timothee Delubac, James Rich, Stephen Bailey, Andreu Font-Ribera, David Kirkby, J-M Le Goff, Matthew M Pieri, Anze Slosar, Éric Aubourg, Julian E Bautista, et al. Baryon acoustic oscillations in the $\text{Ly}\alpha$ forest of boss quasars. *Astronomy & Astrophysics*, 552:A96, 2013.
- [9] Anže Slosar, Andreu Font-Ribera, Matthew M Pieri, James Rich, Jean-Marc Le Goff, Éric Aubourg, Jon Brinkmann, Bill Carithers, Romain Charlaisier, Marina Cortès, et al. The lyman- α forest in three dimensions: measurements of large scale flux correlations from boss 1st-year data. *Journal of Cosmology and Astroparticle Physics*, 2011(09):001, 2011.
- [10] Shirley Ho, Christopher Hirata, Nikhil Padmanabhan, Uros Seljak, and Neta Bahcall. Correlation of cmb with large-scale structure. i. integrated sachs-wolfe tomography and cosmological implications. *Physical Review D—Particles, Fields, Gravitation, and Cosmology*, 78(4):043519, 2008.

- [11] Martin Kilbinger. Cosmology with cosmic shear observations: a review. *Reports on Progress in Physics*, 78(8):086901, 2015.
- [12] Alexander Friedman. Über die krümmung des raumes. *Zeitschrift für Physik*, 10(1):377–386, 1922.
- [13] Steven Weinberg. *Gravitation and cosmology: principles and applications of the general theory of relativity*. John Wiley & Sons, 2013.
- [14] Kip S Thorne, Charles W Misner, and John Archibald Wheeler. *Gravitation*. Freeman San Francisco, 2000.
- [15] Viatcheslav Mukhanov. *Physical foundations of cosmology*. Cambridge university press, 2005.
- [16] Sean M Carroll. *Spacetime and geometry*. Cambridge University Press, 2019.
- [17] David Hilbert. Die grundlagen der physik. *Mathematische Annalen*, 92(1):1–32, 1924.
- [18] Luca Amendola and Shinji Tsujikawa. *Dark energy: theory and observations*. Cambridge University Press, 2010.
- [19] Albert Einstein. Kosmologische betrachtungen zur allgemeinen relativitätstheorie. *Sitzungsberichte der Königlich Preußischen Akademie der Wissenschaften*, pages 142–152, 1917.
- [20] Edwin Hubble. A relation between distance and radial velocity among extra-galactic nebulae. *Proceedings of the national academy of sciences*, 15(3):168–173, 1929.
- [21] George Gamow. The evolutionary universe. *Scientific American*, 195(3):136–156, 1956.
- [22] Adam G Riess, Alexei V Filippenko, Peter Challis, Alejandro Clocchiatti, Alan Diercks, Peter M Garnavich, Ron L Gilliland, Craig J Hogan, Saurabh Jha, Robert P Kirshner, et al. Observational evidence from supernovae for an accelerating universe and a cosmological constant. *The astronomical journal*, 116(3):1009, 1998.
- [23] Saul Perlmutter, Goldhaber Aldering, Gerson Goldhaber, Richard A Knop, Peter Nugent, Patricia G Castro, Susana Deustua, Sébastien Fabbro, Ariel Goobar, Donald E Groom, et al. Measurements of ω and λ from 42 high-redshift supernovae. *The Astrophysical Journal*, 517(2):565, 1999.
- [24] Shadab Alam, Marie Aubert, Santiago Avila, Christophe Balland, Julian E Bautista, Matthew A Bershadsky, Dmitry Bizyaev, Michael R Blanton, Adam S Bolton, Jo Bovy, et al. Completed sdss-iv extended baryon oscillation spectroscopic survey: Cosmological implications from two decades of spectroscopic surveys at the apache point observatory. *Physical Review D*, 103(8):083533, 2021.

- [25] Alexandra Amon, Daniel Gruen, Michael A Troxel, Niall MacCrann, Scott Dodelson, Ami Choi, Cyrille Doux, Lucas F Secco, Simon Samuroff, Elisabeth Krause, et al. Dark energy survey year 3 results: Cosmology from cosmic shear and robustness to data calibration. *Physical Review D*, 105(2):023514, 2022.
- [26] Marika Asgari, Chieh-An Lin, Benjamin Joachimi, Benjamin Giblin, Catherine Heymans, Hendrik Hildebrandt, Arun Kannawadi, Benjamin Stölzner, Tilman Tröster, Jan Luca van den Busch, et al. Kids-1000 cosmology: Cosmic shear constraints and comparison between two point statistics. *Astronomy & Astrophysics*, 645:A104, 2021.
- [27] Catherine Heymans, Tilman Tröster, Marika Asgari, Chris Blake, Hendrik Hildebrandt, Benjamin Joachimi, Konrad Kuijken, Chieh-An Lin, Ariel G Sánchez, Jan Luca Van Den Busch, et al. Kids-1000 cosmology: Multi-probe weak gravitational lensing and spectroscopic galaxy clustering constraints. *Astronomy & Astrophysics*, 646:A140, 2021.
- [28] Nathan J Secrest, Sebastian von Hausegger, Mohamed Rameez, Roya Mohayaee, Subir Sarkar, and Jacques Colin. A test of the cosmological principle with quasars. *The Astrophysical journal letters*, 908(2):L51, 2021.
- [29] Dominik J Schwarz, Craig J Copi, Dragan Huterer, and Glenn D Starkman. Cmb anomalies after planck. *Classical and Quantum Gravity*, 33(18):184001, 2016.
- [30] Lavrentios Kazantzidis and Leandros Perivolaropoulos. Evolution of the f σ_8 tension with the planck $15/\lambda$ cdm determination and implications for modified gravity theories. *Physical Review D*, 97(10):103503, 2018.
- [31] Leandros Perivolaropoulos and Foteini Skara. Challenges for λ cdm: An update. *New Astronomy Reviews*, 95:101659, 2022.
- [32] Bradley W Carroll and Dale A Ostlie. *An introduction to modern astrophysics*. Cambridge University Press, 2017.
- [33] Hannu Karttunen, Pekka Kröger, Heikki Oja, Markku Poutanen, and Karl Johan Donner. *Fundamental astronomy*. Springer, 2007.
- [34] Lennart Lindegren, SA Klioner, J Hernández, A Bombrun, M Ramos-Lerate, Hea Steidelmüller, U Bastian, M Biermann, A de Torres, E Gerlach, et al. Gaia early data release 3-the astrometric solution. *Astronomy & Astrophysics*, 649:A2, 2021.
- [35] Henrietta S Leavitt and Edward C Pickering. Periods of 25 variable stars in the small magellanic cloud. *Harvard College Observatory Circular, vol. 173, pp. 1-3*, 173:1–3, 1912.

- [36] Lucas M Macri, PB Stetson, GD Bothun, WL Freedman, PM Garnavich, S Jha, BF Madore, and Michael W Richmond. The discovery of cepheids and a new distance to ngc 2841 using thehubble spacetelescope. *The Astrophysical Journal*, 559(1):243, 2001.
- [37] Laura Ferrarese, NA Silbermann, Jeremy R Mould, Peter B Stetson, Abhijit Saha, Wendy L Freedman, and Robert C Kennicutt. Photometric recovery of crowded stellar fields observed with hst/wfpc2 and the effects of confusion noise on the extragalactic distance scale. *Publications of the Astronomical Society of the Pacific*, 112(768):177, 2000.
- [38] Nial R Tanvir, MA Hendry, A Watkins, SM Kanbur, LN Berdnikov, and CC Ngeow. Determination of cepheid parameters by light-curve template fitting. *Monthly Notices of the Royal Astronomical Society*, 363(3):749–762, 2005.
- [39] Boris Trahin, Louise Breuval, Pierre Kervella, Antoine Mérand, Nicolas Nardetto, Alexandre Gallenne, Vincent Hocdé, and Wolfgang Gieren. Inspecting the cepheid parallax of pulsation using gaia edr3 parallaxes-projection factor and period-luminosity and period-radius relations. *Astronomy & Astrophysics*, 656:A102, 2021.
- [40] Wendy L Freedman and Barry F Madore. The hubble constant. *Annual Review of Astronomy and Astrophysics*, 48(1):673–710, 2010.
- [41] M Romaniello, Francesca Primas, M Mottini, S Pedicelli, Bertrand Lemasle, G Bono, Patrick François, MAT Groenewegen, and CD Laney. The influence of chemical composition on the properties of cepheid stars-ii. the iron content. *Astronomy & Astrophysics*, 488(2):731–747, 2008.
- [42] Jesper Storm, Wolfgang Gieren, Pascal Fouque, Thomas G Barnes, G Pietrzyński, Nicolas Nardetto, M Weber, T Granzer, and KG Strassmeier. Calibrating the cepheid period-luminosity relation from the infrared surface brightness technique-i. the p-factor, the milky way relations, and a universal k-band relation. *Astronomy & Astrophysics*, 534:A94, 2011.
- [43] Adam G Riess, Lucas M Macri, Samantha L Hoffmann, Dan Scolnic, Stefano Casertano, Alexei V Filippenko, Brad E Tucker, Mark J Reid, David O Jones, Jeffrey M Silverman, et al. A 2.4% determination of the local value of the hubble constant. *The Astrophysical Journal*, 826(1):56, 2016.
- [44] Wendy L Freedman, Barry F Madore, Brad K Gibson, Laura Ferrarese, Daniel D Kelson, Shoko Sakai, Jeremy R Mould, Robert C Kennicutt Jr, Holland C Ford, John A Graham, et al. Final results from the hubble space telescopekey project to measure the hubbleconstant. *The Astrophysical Journal*, 553(1):47, 2001.
- [45] Wenlong Yuan, Adam G Riess, Stefano Casertano, and Lucas M Macri. A first look at cepheids in a type ia supernova host with jwst. *The Astrophysical Journal Letters*, 940(1):L17, 2022.

- [46] Subrahmanyan Chandrasekhar. The maximum mass of ideal white dwarfs. *Astrophysical Journal*, vol. 74, p. 81, 74:81, 1931.
- [47] R Kessler, J Marriner, M Childress, R Covarrubias, CB D'Andrea, DA Finley, J Fischer, Ryan Joseph Foley, D Goldstein, RR Gupta, et al. The difference imaging pipeline for the transient search in the dark energy survey. *The Astronomical Journal*, 150(6):172, 2015.
- [48] J Parrent, B Friesen, and M Parthasarathy. A review of type ia supernova spectra. *Astrophysics and Space Science*, 351:1–52, 2014.
- [49] Peter Lundqvist, Seppo Mattila, Jesper Sollerman, Cecilia Kozma, E Baron, Nick LJ Cox, Claes Fransson, Bruno Leibundgut, and Jason Spyromilio. Hydrogen and helium in the spectra of type ia supernovae. *Monthly Notices of the Royal Astronomical Society*, 435(1):329–345, 2013.
- [50] Gastón Folatelli, Nidia Morrell, Mark M Phillips, Eric Hsiao, Abdo Campillay, Carlos Contreras, Sergio Castellón, Mario Hamuy, Wojtek Krzeminski, Miguel Roth, et al. Spectroscopy of type ia supernovae by the carnegie supernova project. *The Astrophysical Journal*, 773(1):53, 2013.
- [51] Richard Kessler, Bruce Bassett, Pavel Belov, Vasudha Bhatnagar, Heather Campbell, Alex Conley, Joshua A Frieman, Alexandre Glazov, Santiago González-Gaitán, Renée Hlozek, et al. Results from the supernova photometric classification challenge. *Publications of the Astronomical Society of the Pacific*, 122(898):1415, 2010.
- [52] A Möller, V Ruhlmann-Kleider, C Leloup, J Neveu, N Palanque-Delabrouille, J Rich, R Carlberg, Christopher Lidman, and C Pritchett. Photometric classification of type ia supernovae in the supernova legacy survey with supervised learning. *Journal of Cosmology and Astroparticle Physics*, 2016(12):008, 2016.
- [53] RC Chen, D Scolnic, M Vincenzi, ES Rykoff, J Myles, R Kessler, B Popovic, M Sako, M Smith, P Armstrong, et al. Evaluating cosmological biases using photometric redshifts for type ia supernova cosmology with the dark energy survey supernova program. *Monthly Notices of the Royal Astronomical Society*, 536(2):1948–1966, 2025.
- [54] Malcolm Hicken, Peter Challis, Robert P Kirshner, Armin Rest, Claire E Cramer, W Michael Wood-Vasey, Gaspar Bakos, Perry Berlind, Warren R Brown, Nelson Caldwell, et al. CfA4: light curves for 94 type ia supernovae. *The Astrophysical Journal Supplement Series*, 200(2):12, 2012.
- [55] P Astier, P El Hage, J Guy, D Hardin, M Betoule, S Fabbro, N Fourmanoit, R Pain, and N Regnault. Photometry of supernovae in an image series: methods and application to the supernova legacy survey (snls). *Astronomy & Astrophysics*, 557:A55, 2013.

- [56] Nicolas Regnault, A Conley, J Guy, M Sullivan, J-C Cuillandre, P Astier, C Balland, S Basa, RG Carlberg, D Fouchez, et al. Photometric calibration of the supernova legacy survey fields. *Astronomy & Astrophysics*, 506(2):999–1042, 2009.
- [57] M Betoule, J Marriner, N Regnault, J-C Cuillandre, P Astier, J Guy, C Balland, P El Hage, D Hardin, R Kessler, et al. Improved photometric calibration of the snls and the sdss supernova surveys. *Astronomy & Astrophysics*, 552:A124, 2013.
- [58] Xiaosheng Huang, Zachary Raha, G Aldering, Pierre Antilogus, S Bailey, C Baltay, K Barbary, Derek Baugh, Kyle Boone, Sebastien Bongard, et al. The extinction properties of and distance to the highly reddened type ia supernova 2012cu. *The Astrophysical Journal*, 836(2):157, 2017.
- [59] C. Alard and Robert H. Lupton. A method for optimal image subtraction. *The Astrophysical Journal*, 503(1):325–331, August 1998.
- [60] Monique Signore and Denis Puy. Supernovae and cosmology. *New Astronomy Reviews*, 45(4–5):409–423, March 2001.
- [61] Bill S. Wright and Baojiu Li. Type ia supernovae, standardizable candles, and gravity. *Physical Review D*, 97(8), April 2018.
- [62] M. M. Phillips. The absolute magnitudes of type ia supernovae. *Astrophysical Journal Letters*, 413:L105–L108, 1993.
- [63] B. Leibundgut, R. Schommer, M. Phillips, A. Riess, B. Schmidt, J. Spyromilio, J. Walsh, N. Suntzeff, M. Hamuy, J. Maza, R. P. Kirshner, P. Challis, P. Garnavich, R. C. Smith, A. Dressler, and R. Ciardullo. Time dilation in the light curve of the distant type ia supernova sn 1995k. *The Astrophysical Journal*, 466(1):L21–L24, July 1996.
- [64] Alex Kim, Ariel Goobar, and Saul Perlmutter. A generalized k correction for type ia supernovae: Comparing r-band photometry beyond $z=0.2$ with b, v, and r-band nearby photometry. *Publications of the Astronomical Society of the Pacific*, 108:190, February 1996.
- [65] J. Guy, P. Astier, S. Baumont, D. Hardin, R. Pain, N. Regnault, S. Basa, R. G. Carlberg, A. Conley, S. Fabbro, D. Fouchez, I. M. Hook, D. A. Howell, K. Perrett, C. J. Pritchett, J. Rich, M. Sullivan, P. Antilogus, E. Aubourg, G. Bazin, J. Bronder, M. Filiol, N. Palanque-Delabrouille, P. Ripoche, and V. Ruhlmann-Kleider. Salt2: using distant supernovae to improve the use of type ia supernovae as distance indicators. *Astronomy & Astrophysics*, 466(1):11–21, February 2007.
- [66] Saurabh Jha, Adam G. Riess, and Robert P. Kirshner. Improved distances to type ia supernovae with multicolor light-curve shapes: Mlcs2k2. *The Astrophysical Journal*, 659(1):122–148, April 2007.

- [67] Adam G. Riess, Wenlong Yuan, Lucas M. Macri, Dan Scolnic, Dillon Brout, Stefano Casertano, David O. Jones, Yukei Murakami, Gagandeep S. Anand, Louise Breuval, Thomas G. Brink, Alexei V. Filippenko, Samantha Hoffmann, Saurabh W. Jha, W. D'arcy Kenworthy, John Mackenty, Benjamin E. Stahl, and WeiKang Zheng. A comprehensive measurement of the local value of the hubble constant with 1 km s1 mpc1 uncertainty from the hubble space telescope and the sh0es team. *The Astrophysical Journal Letters*, 934(1):L7, July 2022.
- [68] Matt Visser. Jerk, snap and the cosmological equation of state. *Classical and Quantum Gravity*, 21(11):2603–2615, April 2004.
- [69] MICHEL CHEVALLIER and DAVID POLARSKI. Accelerating universes with scaling dark matter. *International Journal of Modern Physics D*, 10(02):213–223, April 2001.
- [70] Eric V. Linder. Exploring the expansion history of the universe. *Physical Review Letters*, 90(9), March 2003.
- [71] Dragan Huterer and Michael S. Turner. Probing dark energy: Methods and strategies. *Physical Review D*, 64(12), November 2001.
- [72] L. Verde. *Statistical Methods in Cosmology*, page 147–177. Springer Berlin Heidelberg, 2010.
- [73] Christian P. Robert. The metropolis-hastings algorithm, 2016.
- [74] John Skilling. Nested sampling for general bayesian computation. 2006.
- [75] Edward Higson, Will Handley, Michael Hobson, and Anthony Lasenby. Dynamic nested sampling: an improved algorithm for parameter estimation and evidence calculation. *Statistics and Computing*, 29:891–913, 2019.
- [76] Joshua S Speagle. dynesty: a dynamic nested sampling package for estimating bayesian posteriors and evidences. *Monthly Notices of the Royal Astronomical Society*, 493(3):3132–3158, February 2020.
- [77] Ryan E. Keeley, Arman Shafieloo, and Benjamin L'Huillier. An analysis of variance of the pantheon+ dataset: Systematics in the covariance matrix? *Universe*, 10(12):439, November 2024.
- [78] Kenneth P Burnham, David R Anderson, Kenneth P Burnham, and David R Anderson. *Practical use of the information-theoretic approach*. Springer, 1998.
- [79] Robert E Kass and Adrian E Raftery. Bayes factors. *Journal of the american statistical association*, 90(430):773–795, 1995.
- [80] William H Press. *Numerical recipes 3rd edition: The art of scientific computing*. Cambridge university press, 2007.

- [81] W. D'Arcy Kenworthy, Adam G. Riess, Daniel Scolnic, Wenlong Yuan, José Luis Bernal, Dillon Brout, Stefano Casertano, David O. Jones, Lucas Macri, and Erik R. Peterson. Measurements of the hubble constant with a two-rung distance ladder: Two out of three ain't bad. *The Astrophysical Journal*, 935(2):83, August 2022.
- [82] Eoin Ó Colgáin, Saeed Pourojaghi, M. M. Sheikh-Jabbari, and Darragh Sherwin. A comparison of bayesian and frequentist confidence intervals in the presence of a late universe degeneracy, 2025.
- [83] Jeremy Mould and Syed A. Uddin. Constraining a possible variation of g with type ia supernovae. *Publications of the Astronomical Society of Australia*, 31, 2014.
- [84] Valerio Marra and Leandros Perivolaropoulos. Rapid transition of g eff at $z \approx 0.01$ as a possible solution of the hubble and growth tensions. *Physical Review D*, 104(2):L021303, 2021.
- [85] Mario Ballardini, Fabio Finelli, and Domenico Sapone. Cosmological constraints on the gravitational constant. *Journal of Cosmology and Astroparticle Physics*, 2022(06):004, 2022.
- [86] Leandros Perivolaropoulos and Foteini Skara. Gravitational transitions via the explicitly broken symmetron screening mechanism. *Physical Review D*, 106(4):043528, 2022.
- [87] Wen Zhao, Bill S Wright, and Baojiu Li. Constraining the time variation of newton's constant g with gravitational-wave standard sirens and supernovae. *Journal of Cosmology and Astroparticle Physics*, 2018(10):052, 2018.